Characterization of a Dual-Mode Scramjet via Stereoscopic Particle Image Velocimetry

---

A Dissertation

Presented to

the faculty of the School of Engineering and Applied Science

University of Virginia

In Partial Fulfillment

Of the requirements for the Degree

Doctor of Philosophy

Mechanical and Aerospace Engineering

by

Brian E. Rice

August 2014

Approval Sheet

This dissertation is submitted in partial fulfillment of the requirements for the degree of

Doctor of Philosophy in Mechanical and Aerospace Engineering

_____

Brian Rice, AUTHOR

This dissertation has been read and approved by the examining committee:

_____

Christopher P. Goyne, Advisor

_____

James C. McDaniel, Advisor

_____

Harsha Chelliah, Dissertation Committee Chair

_____

Eric Loth, Committee Member

_____

George L. Cahen, Committee Member

Accepted for the School of Engineering and Applied Science:

_____

Dean, School of Engineering and Applied Science

August 2014

Abstract

Scramjet propulsion devices have the potential for revolutionizing high-speed atmospheric flight in the future. This includes aerospace planes for space access and high-speed long distance strike vehicles for national defense. Despite over 60 years of research, the high-speed, turbulent, combusting flow field of the engine is not fully understood. In particular, the dual-mode scramjet (DMSJ) is complicated by the ability to operate in different modes of combustion. These modes of combustion are referred to as the ramjet mode of operation, characterized by subsonic combustor inflow, and the scramjet mode of operation, characterized by supersonic combustor inflow. The gap in knowledge stems from the inability to experimentally measure pertinent flow properties and the resulting absence of accurate computational tools. Renewed interest in hypersonic flight and the advancement of laser-based optical measurement techniques provide an opportunity to quantify flow properties that were once not accessible. This includes instream Velocimetry in the supersonic, turbulent, combusting flow field of a DMSJ. Such measurements can provide a fundamental understanding of the convective transport processes in these engines. Of particular interest is how these processes change for the DMSJ when operating in the supersonic, subsonic, and mixed modes of combustion.

This work employs the experimental technique of Stereoscopic Particle Image Velocimetry (SPIV) to measure the 3-dimensional, instantaneous velocity within a DMSJ model. This work is part of the greater collaborative efforts of the National Center for Hypersonic Combined Cycle Propulsion (NCHCCP). Significant design of new DMSJ model hardware was necessary to allow the extensive experimental testing with the end

goal of building a one-of-a-kind data set for the development and validation of advanced modeling techniques.

The work presented herein contributes to this goal by measuring the flow field within the combustor section in both the ramjet mode and scramjet mode of operation at four axial locations. These measurements represent the first reported SPIV measurements in the two different modes of operation of a DMSJ and reveal the key similarities and differences between the modes. The influence on the velocity field as the combustion process develops axially is also identified for each mode. Additionally, the measurements serve to quantify the velocity bias associated with the single-stream seeding method. The primary properties presented in the current study are mean velocity magnitude, cross-plane velocity vectors, vorticity, and turbulent kinetic energy. The defining flow features of the scramjet mode of operation are a low-momentum separation region near the fuel injection wall surrounded by a high-speed freestream. Alternatively, the ramjet mode of operation consists of a high-speed fuel jet core surrounded by a low-speed freestream. This data helps to identify the location, size, and intensity of the classic ramp fuel injector induced vortices which act to mix the fuel and air. The results indicate that the vortices expand with the axial location in the flowpath while the intensity decreases. In addition, the peak levels of turbulent kinetic energy have been identified ranging between 10,000-15,000 m^2/s^2 and are located corresponding to a shear layer present in the axial velocity component. The comprehensive data set provides converged turbulence statistics and the means to quantitatively compare experiments to numerical models. Comparisons with a hybrid LES/RANS computational model (conducted at N.C. State) reveal some areas of improvement to the computational model but overall excellent agreement was observed.

Acknowledgements

Chris Goyne and Jim McDaniel

Thanks for their continued support throughout the PhD program and the confidence in my capabilities to complete such a challenging academic endeavor

Bob Rockwell and Roland Krauss

Thanks for always being available to offer suggestions or advice and for operating the wind tunnel

Roger Reynolds and Ed Spencley

Thanks for always doing anything necessary to get the job done and Ed for fabrication of precise parts on a tight schedule

Kristin Busa, Jesse Quinlan, Jesse Fulton, Justin Kirik, Josh Codoni, Brendyn Saranacki, Mike Smayda, Ben Tatman, Max Deperio, and Chad Smith

I value the friendship and comradery of my fellow graduate students. Especially thanks to any of the aforementioned people for assistance in running the wind tunnel and changing endless hydrogen cylinders

Harsha Chelliah, Eric Loth, George Cahen

Thanks for guidance throughout the process and serving on my PhD Advisory Committee

Richard Rice, Linda Rice, and Eric Rice

Thanks for supporting me throughout all levels of my education and for the encouragement to pursue a higher degree and the motivation to complete the process

The National Center for Hypersonic Combined Cycle Propulsion

The research was sponsored by the National Center for Hypersonic Combined Cycle Propulsion grant FA 9550-09-1-0611 with technical monitors Chiping Li (AFOSR) and Aaron Auslender and Rick Gaffney (NASA)

Table of Contents

List of Figures

List of Tables

List of Symbols

x, y, z	=	Axial coordinate, transverse vertical coordinate, transverse horizontal coordinate
H	=	Fuel injector normal ramp height
γ	=	Specific heat ration
φ	=	Fuel equivalence ratio
p	=	Static pressure
p_{ref}	=	Measured static pressure immediately downstream of facility nozzle
p_0	=	Flow stagnation pressure
T_0	=	Flow stagnation temperature
T	=	Static temperature
M	=	Mach number
A	=	Nozzle exit area
A^*	=	Nozzle throat area
Δt	=	Time separation between laser pulses
C(dx,dy)	=	Intensity cross-correlation function
Q	=	Peak detection ratio (height of highest peak/height of next highest peak)
Δx_p	=	Seed particle displacement
$f^{\#}$	=	Lens aperture (f-number)
$\boldsymbol{\ell}$	=	Distance along lens principle axis from object plane to image plane
$\boldsymbol{\ell}_I$	=	Interrogation sub-region size
$\boldsymbol{\ell}_{pix}$	=	Physical size of CCD pixels
R	=	Lens reproduction ration defined as the camera CCD area/field of view)
α	=	Image (CCD) plane tilt angle
θ	=	Camera angle measured from normal to the object plane
St	=	Stokes number
τ_p	=	Particle response time
U_f	=	Fluid characteristic velocity

d	=	Fluid domain length scale
ρ_p	=	Particle density
d_p	=	Particle diameter
μ_g	=	Fluid viscosity
Kn	=	Knudsen number
U, V, W	=	Instantaneous velocity components (x-direction, y-direction, z-direction)
$\overline{U}, \overline{V}, \overline{W}$	=	Mean velocity components
u', v', w'	=	Fluctuating velocity components
|V|	=	Instantaneous 3-component velocity magnitude
$\|\overline{V}\|$	=	Mean 3-component velocity magnitude
u, v, w	=	RMS velocity components (u, v, w = $\sqrt{\overline{u'^2}}, \sqrt{\overline{v'^2}}, \sqrt{\overline{w'^2}}$)
|v|	=	RMS Velocity Magnitude
TKE	=	Turbulent kinetic energy
$\overline{u'u'}, \overline{u'v'}, \overline{v'v'}, \overline{v'w'}, \overline{u'w'}, \overline{w'w'}$	=	Reynold's stresses
$\overline{\omega_x}$	=	Mean vorticity
E_{zz}, E_{zy}, E_{yy}, E_{yy}	=	Strain rate
ε	=	Percent different
R_{ii}	=	Velocity correlation function
L_{ii}	=	Integral length scale
δ	=	Difference between SPIV and CFD
β	=	SPIV or CFD scalar velocity quantity comparison

Abbreviations

DMSJ	=	Dual-Mode Scramjet
TBCC	=	Turbine Based Combined Cycle
UVaSCF	=	University of Virginia Supersonic Combustion Facility
NCHCCP	=	National Center for Hypersonic Combined Cycle Propulsion
PIV	=	Particle Image Velocimetry
SPIV	=	Stereoscopic Particle Image Velocimetry

PLIF	=	Planar Laser Induced Fluorescence
PDV	=	Planar Doppler Velocimetry
DGV	=	Doppler Global Velocimetry
LDV	=	Laser Doppler Velocimetry
MSCT	=	Modular Supersonic Combustion Tunnel
EDM	=	Electric Discharge Machining
CFD	=	Computational Fluid Dynamics
RMS	=	Root Mean Square
RSS	=	Root Sum Square
PT	=	Pressure Tap
KPT	=	Kulite Pressure Tap
TC	=	Thermocouple
CARS	=	Coherent Anti-Stokes Raman Scattering
TDLAS	=	Tunable Diode Laser Absorption Spectroscopy
RANS	=	Reynolds Averaged Navier Stokes Equations
LES	=	Large Eddy Simulation
SEM	=	Scanning Electron Microscope

Chapter 1

Introduction

Since original concept in the 1950's, scramjet engines have experienced continued interest for use on hypersonic vehicles. The most common applications for these engines are access to space and long-distance atmospheric flight for strike capability. These engines promise low-cost and dependability due to a simple duct flowpath with few moving mechanical parts. The components of a typical ramjet are a convergent-divergent diffuser, combustor, and convergent-divergent nozzle [1]. The first step of compression occurs due to the deceleration of the incoming airflow through shocks off the forebody and inlet. Further compression occurs in the convergent inlet diffuser where a normal shock system decelerates the flow to subsonic speeds. The subsonic air then expands through the divergent section of the diffuser and further decelerates. In the combustor, the fuel mixes and reacts with the air causing combustion. Combustion results in an increase in temperature and pressure which accelerates the flow through the exhaust convergent-divergent nozzle to supersonic speeds. At higher incoming air speeds it is advantageous to allow supersonic flow through the combustor in order to avoid excessively high combustor pressure and temperature. Thus, a scramjet is utilized which primarily relies on the aircraft forebody and engine inlet for compression. The diffuser is typically convergent and there is no shock system to decelerate the flow to subsonic speeds. Supersonic air enters the combustor where the fuel mixes and burns. Lastly, the flow expands through a divergent nozzle providing thrust to the vehicle.

Combing the function of both ramjets and scramjets in a single flowpath, the dual-mode scramjet (DMSJ) has become the standard propulsion engine to study. A DMSJ enables the propulsion system to operate at peak efficiency across a broad range of Mach numbers from 3-12 with a fixed geometry flow path [2]. The principal advantage of a DMSJ is that there is no need to carry large oxidizer tanks like those of traditional rockets and this offers an increased payload fraction. At speeds in the Mach number range 3-5 the DMSJ operates in ramjet mode which is characterized by subsonic flow at the entrance to the combustor. At speeds above approximately Mach 5, the DMSJ operates in scramjet mode and flow remains supersonic at the entrance to the combustor. Transitioning to scramjet mode above Mach 5 is advantageous to avoid excessive pressure rise and performance losses due to a normal shock wave system [1].

A practical implementation of a DMSJ in a flight vehicle airframe is depicted in Fig. 1. Since the DMSJ does not produce static thrust it is necessary to utilize a combined cycle such as the turbine-based combined cycle (TBCC). The features of the TBCC concept and low- and high-speed flow paths are illustrated in Figure 1.1.

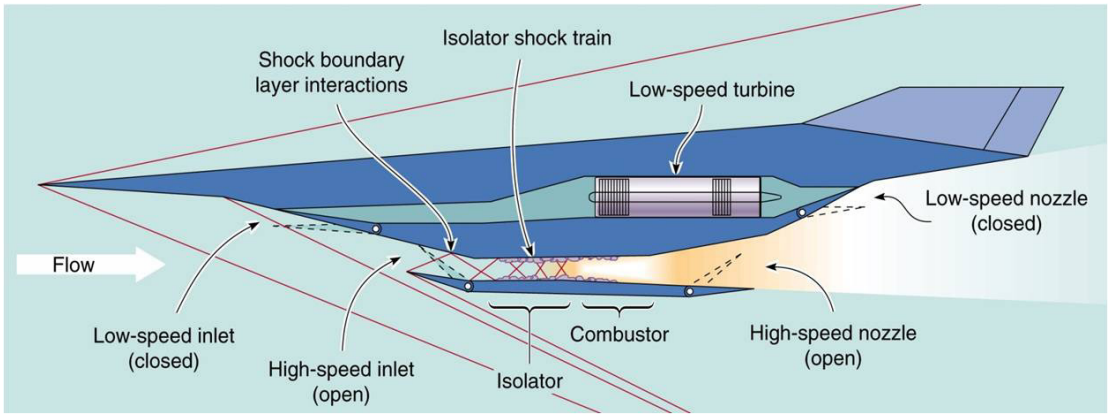

Figure 1.1: Turbine-based combined cycle concept [3].

In the TBCC, the turbine jet engine in the low-speed flowpath powers the flight vehicle up to Mach 3-4 at which point the vehicle transitions to the high-speed flow path DMSJ [3]. This is achieved by closing the low-speed inlet with a mechanical door and opening the high-speed inlet. Other alternatives include a rocket-based combined cycle.

Due to the high cost and risk of flight tests, extensive ground testing of DMSJ's is critical. This presents the opportunity to apply advanced laser-based optical measurement techniques that are more suited to the laboratory. The University of Virginia Supersonic Combustion Facility (UVaSCF) has enabled direct-connect testing of a representative high-speed DMSJ flowpath [3]. A photo of the DMSJ model is shown in Figure 1.2.

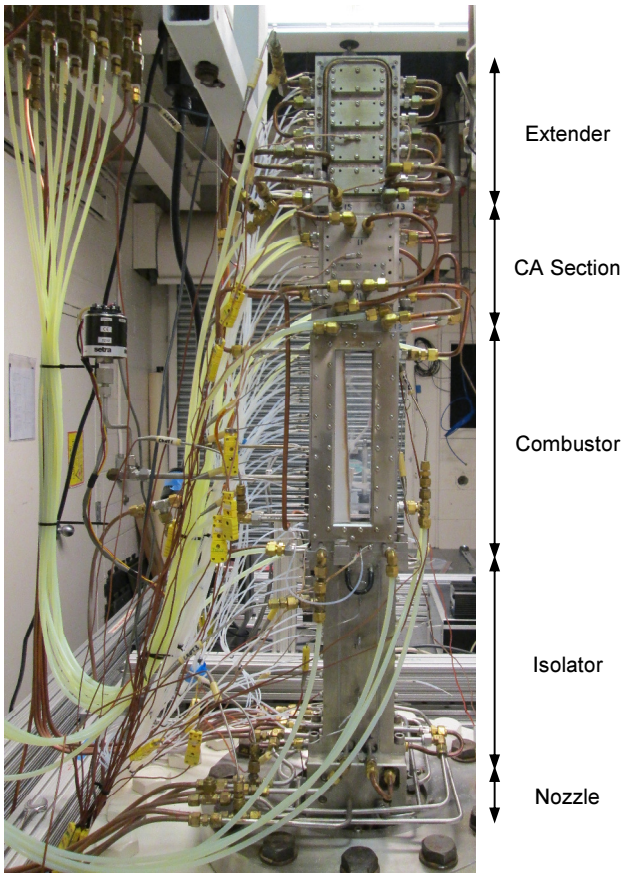

Figure 1.2: Photograph of the Configuration C Dual-Mode Scramjet model.

As presented in Figs. 1.1 and 1.2, a DMSJ is comprised of a constant area isolator section which serves to prevent combustor-inlet interaction and provide an area for gradual pressure rise. If the pressure rise due to combustion is high enough, a normal or oblique shock train develops in the isolator, the combustor Mach number reduces, and the flowpath undergoes mode transition. The location and control of the shock train is of main concern because if it reaches the inlet, unstart conditions develop. Unstart conditions reduce the air mass flow rate, reduce total pressure and lead to dynamic changes in the vehicle trim [1]. In the combustor section of the flowpath in Fig. 2, hydrogen fuel is injected via a ramp fuel injector that serves to mix the fuel and air. The primary imposed mixing mechanism arises from stream-wise counter-rotation vortices induced by the adverse pressure gradient across the ramp surface. The presence of these vortices results in a flow field that is highly three-dimensional. After the combustor section is an intermediate constant area section that was intended mainly for optical access but also aids the combustion process by creating backpressure and an area for a thermal throat to develop. Finally the combusted flow expands through a divergent extender section to adjust the outlet flow to ambient conditions.

One of the key challenges involved with scramjet operation is that the residence time of the fuel is on the same order as the chemical reaction rates, making flameholding extremely difficult. Therefore, the ability to achieve adequate fuel/air mixing despite very short fuel residence times in the combustor is vital. One of the classic solutions to this problem is to utilize a ramp fuel injector which assists in the mixing of the air and fuel through streamwise vortices. The streamwise vortices are generated due to spillage of air over the edges of the ramp into a low pressure region. Therefore, it is important to

accurately measure the velocity, vorticity, and turbulence in order to provide an understanding of the fuel/air mixing process. Of particular interest to the current study is how the convective transport processes in the DMSJ combustor change as the flowpath undergoes mode transition. This is because the fuel injection, mixing, and combustion take place, in a one-dimensional sense, in supersonic and subsonic flow in the scramjet and ramjet modes of operation, respectively. This results in fundamental differences in the velocity field that need to be identified and understood if engine operation and performance it to be optimized across the entire DMSJ flight envelope. Despite significantly different combustor entrance Mach numbers of approximately 1.6 (scram) and 0.8 (ram), the Reynolds number, will be approximately 150,000 and 142,000 respectively. The Reynolds number is a ratio of inertial forces to viscous forces and dictates predominant flow features. The Reynolds number in which a duct flow transitions from laminar to turbulent is approximately 4000. This indicates that both modes of combustion will be highly turbulent. The scamjet mode of operation is characterized by higher velocity but lower density due to lower pressure whereas the ramjet mode is characterized by lower velocity and higher density due to elevated pressure from the isolator shock train. These opposing tendencies lead to comparable Reynolds numbers (at the combustor entrance) which non-dimensionalize the flow and indicate dynamic similitude between modes of operation. Therefore, both modes of operation should share many flow properties. Relatively similar Reynolds numbers will lead to largely comparable turbulent mixing length scales due to strong Reynolds number dependence.

1.1 Motivation and Scope

The National Center for Hypersonic Combined Cycle Propulsion (NCHCCP) began in 2009 with the goal of creating a multidisciplinary approach to solving the critical problems faced by the hypersonic community. The motivation for a hypersonic vehicle is two-fold. First and most immediate, the U.S. military is eager to develop scramjet technology for the application of a Prompt Global Strike missile for national defense [4]. Secondly, NASA is interested in the application of DMSJ engines for access to space via a reusable shuttle [5]. Flight testing of DMSJ engines is extremely costly and high risk. For example, the X-51 Waverider developed by DARPA, Boeing, Pratt & Whitney, Rocketdyne, and NASA has cost approximately $70M in the detailed design phase and roughly $7.7M for multiple flight tests [6]. To date, the X-51 program has cost more than $300M [7]. The NASA X-43A hydrogen gas-powered scramjet program similarly cost a total of $240M [8]. The X-51 demonstration aircraft performed a total of four powered flight tests. The first test, in 2010, was marginally successful and achieved 200 seconds of powered flight reaching Mach 5 but ended earlier than the planned 300 seconds [9]. In 2011, the scramjet engine was boosted to Mach 5 by rocket but experienced engine inlet unstart. In the second test the engine was not able to properly transition from ethylene to JP-7 fuel. In 2012, the third test flight was a failure due to an aerodynamic fin control issue and no powered flight data was achieved. Finally, in 2013 the X-51 demonstrator performed a successful flight test which separated from the booster and flew under scramjet power for 210 seconds burning all of the fuel on board. Although, much has been learned from both the failures and successes of the flight tests, the high risk involved is apparent. Therefore, an alternative for experimental testing of scramjet

engines at significantly lower cost and risk is necessary. Experimental ground testing is an advantageous alternative because a comprehensive suite of diagnostics and measurements can be performed which would not be possible during flight. In addition, the measurements performed during ground testing provide a unique data set available for comparison and validation of advanced computational modeling techniques.

1.2 Dissertation Goal and Objectives

The primary goal of the present PhD research is to:

> *Advance the understanding of dual-mode scramjet operation and supersonic combustion flow regimes by measuring three-components of instantaneous velocity in a DMSJ combustor.*

This will be accomplished in the present study by:

1. Designing new test sections that
    a. Enhance the optical access in the combustor section of the DMSJ in order to allow advanced laser-based optical diagnostics
    b. Employ a modular combustor section that serves to accommodate various fuel injectors
2. Utilizing advanced laser-based optical diagnostics, such as Stereoscopic Particle Image Velocimetry (SPIV), to further understand the flow physics in the combustor of a DMSJ which will:

   a. Provide mean velocity and turbulent statistics to compare the ramjet mode and scramjet mode of operation.
   b. Allow quantitative measurement of the effect of velocity bias errors induced by the seeding method

3. Providing a comprehensive benchmark dataset for the development and validation of advanced DMSJ computational models and a means to quantitatively compare experiment with CFD.

1.3 Historical Background

In recent years, optical digital imaging diagnostic techniques applied to high-speed/combusting flows have experienced rapid growth. Techniques employed to measure velocity in such flows include Planar Doppler Velocimetry (PDV)/Doppler Global Velocimetry (DGV), Planar Laser-Induced Fluorescence (PLIF), and Particle Image Velocimetry (PIV). Each of these techniques have their inherent strengths and weaknesses, which make them more or less well-suited for application in a DMSJ. The common thread among these techniques is that they impart little to no disturbances on the flow. This is essential in high-speed, high-temperature flows because traditional measurement devices are intrusive and cannot survive the harsh environment.

In 1964, Cummins et al. recognized the ability to measure point fluid velocity from the Doppler shift [10]. Cummins investigated the spectrum of Rayleigh scattered light from a suspension of small particles and observed a shift in the frequency of the light which can be attributed to the velocity of the fluid. In 1983, Adrian drew upon this concept to further develop the Laser Doppler Velocimetry (LDV) technique [11]. The

basic principle of LDV is measuring the Doppler shift of scattered light from small tracer particles. A typical LDV optical setup consists of two visible beams of laser light which intersect at a small volume of interest. As particles move into the measurement volume, the light reflected off of the particles is captured by a photodetector. The reflected light from the two lasers interfere resulting in a set of straight fringes. The fringes fluctuate in intensity with a frequency equivalent to the Doppler shift. From the Doppler shift, the component of velocity in the plane of the two beams can be calculated. The technique has been extensively explored and is well established in the community. The primary disadvantage of LDV is that the measurement can only resolve velocity components at single points and is not planar. Three-component LDV systems are commercially available and measure fluctuating, as well as mean, velocity but is limited to point measurements.

In 1991, Komine and Brosnan extended these principles to the technique of Planar Doppler Velocimetry [12]. PDV has the capability of measuring three components of instantaneous velocity over a 2-D plane. PDV utilizes a molecular filter to measure the frequency shift of scattered light from tracer particles. In order to measure one component of velocity, an injection-seeded Nd:YAG laser is used to illuminate the plane of interest. The scattered light is split into two beams, one of which passes through an iodine filter, and is imaged onto two CCD cameras. The primary drawback of such a system is that in order to measure three components of velocity, three or more cameras are necessary to view from multiple perspectives. This presents a challenge with optical access, particularly for a DMSJ. Such systems would require windows on all four walls of the model which is expensive, impractical, and subject to window failure due to

thermal loads. PDV experienced rapid grown in the 1990's due to the parallel advancement of high repetition rate lasers and high-speed CCD cameras. In 2004, Thurow et al. successfully measured one component of velocity in a supersonic jet at MHz rates [13].

The Planar Laser-Induced Fluorescence (PLIF) technique follows similar principles as PDV but the execution differs. Both qualitative images of reaction zones and velocity measurements can be extracted depending on the optical setup. PLIF typically relies on combustion products such as OH or CH as tracer particles. As a result, there exist no problems with particle tracking. The work of McIntyre et al. utilized the technique to determine the location at which ignition was taking place in the shear layer between fuel and air in a scramjet model combustor [14]. Parker et al. similarly employed PLIF for qualitative imaging of combusting regions in a scramjet model [15]. Lessons learned from these earlier works motivated Donbar et al. to apply a qualitative PLIF technique to a cavity fueled scramjet model [16]. The measurements allowed the researchers to observe large-scale structures in the flow and development of the mixing/combusting process through the combustor. A more powerful, but complex, application of PLIF allows for quantitative measurement of velocity. Since the combustion-produced OH radicals act as the tracer, velocity measurements can only be acquired in areas where combustion is taking place and sufficient products are present. The combustion products are illuminated with a UV laser sheet and digital cameras record the spectral information. Two counter-propagating sheets are passed through the flow at different angles to each other in order to measure the Doppler frequency shift from the tracer products. PLIF is favorable in supersonic combustion applications because the introduction of foreign

particles is avoided. The PLIF Velocimetry technique was demonstrated with success at the UVsSCF with ramp fuel injection [17]. OH radical species acted as the tracers in the experiment which measured two components of velocity along a streamwise plane parallel to the fuel injection wall. However, the diagnostic did not have the capability of measuring instantaneous velocity fields and required three or more cameras and viewing angles to measure all three components of velocity.

PIV was chosen as the best optical Velocimetry technique for the current work due to: a) the necessity of measuring all three-components of velocity with a limited number of cameras (two), and b) the necessity of measuring instantaneous velocity in order to obtain turbulent statistics. The fundamental concept of the PIV technique involves illuminating injected seed particles with a pulsed laser sheet and imaging the movement of the particles with a CCD camera over a given small time delay in order to measure displacement. A statistical cross-correlation method calculates velocity vectors based on the measured displacement and time separation between laser pulses. Detailed explanation of the PIV technique will follow in Chapter 3. Table 1.1 summarizes the application of PIV/SPIV to high-speed or combusting flow fields that share similarities with DMSJ experiments.

Table 1.1: PIV applications and developments common to DMSJ flows.

Year	Author	2D/3D	Particle Type/Size	Application: Impact
1993	Molezzi, M.J[18]	2	Oil/800 nm	High-Speed Separated Flows: Improved spatial resolution and accuracy using sub-micron particles
2001	Weisgerber, H[19]	2	SiO_2/12 nm	M2 Hydrogen-Air Supersonic Combustion: Demonstration of 2D PIV for scramjet flows and compared to LDV to assess tracer tracking
2002	Lang, H[20]	3	Oil/700 nm	Transonic Turbine Stage
2002	Ikeda, Y[21]	2	SiO_2/2200 nm	M2.5 Step-back Flow with Normal Injection: Worked to optimize parameters such as laser pulse separation, sheet thickness, and interrogation area
2003	Scarano, F[22]	2	TiO_2/270 nm	2-D Compressible Wake: Seeding particle response measured experimentally
2003	Alkislar, M.B[23]	3	Oil/300nm, Smoke/1μm	Screeching Rectangular Jet: High resolution of shock structures and temporal evolution of eddy circulation
2004	Scheel, F[24]	2	Aerosil/12 nm	Reacting Scramjet Combustion: Comparison of mixing capability and performance of different fuel injectors
2004	Gupta, A[25]	3	Sub-micron	Luminous Spray Flames: Developed method to minimize background luminosity from flames using bandpass filter and mechanical shutter.
2005	Tanahashi, M.[26]	3	Al_2O_3/180 nm	Turbulent Premixed Flames: Decreased interference between PIV/PLIF and discovered misinterpretation of flame interaction based on
2006	Arai, T[27]	2	700 nm	Scramjet Combustor: Studied breakdown process of streamwise vortices
2006	Goyne, C.P[28]	2	Al_2O_3/300 nm	DMSJ Combustor: Investigated the effects of combustion on fuel/air mixing
2007	Filatyev, S.A[29]	3	Al_2O_3/500 nm	Turbulent Premixed Flames: Simultaneous SPIV/PLIF showed interaction of flame front and vortex structures
2007	Beresh, S.J[30]	3	Oil/300 nm	Laterally Inclined Supersonic Jet in Transonic Crossflow: Assessment of position and strength of counter-rotating vortices
2008	Smith, C[31]	3	Al_2O_3/300 nm	Scramjet Combustor: First experimentally obtained, instantaneous, 3C velocity fields for a scramjet during combustion
2010	Wagner, J.L[32]	2	TiO_2/250 nm	Inlet-Isolator Unstart in M5 Flow: Time resolved measurement of unstart process showed shock-induced separation in the isolator
2012	Tuttle, S.G[33]	2	TiO_2/100 nm	Isothermal and Exothermic High-Speed Cavity: Study of the cavity shear layer impingement at various operating conditions. Observation of

It is evident from Table 1.1 that PIV has been applied frequently with success to similar flow fields. However, no Velocimetry technique, including PIV, has been applied to a DMSJ undergoing mode transition. Due to thermal properties and flow tracking characteristics, the most common seeding materials for the high-temperature and high-speed PIV applications are Al_2O_3, TiO_2, and SiO_2 with diameters of less than 1 micron. Tanahashi et al. showed that all three components of velocity are necessary in the study of premixed flames due to the highly three-dimensional nature of the flame front [26]. Examination of large out-of-plane fluctuations allowed for a much greater understanding of the flow. Several authors have published 2D PIV results of ramp fueled DMSJ's, cavity fueled DMSJ's, and a DMSJ isolator [24, 28, 32, 33]. A significant gap in the literature is the measurement of all three components of velocity, particularly with respect to DMSJ's. SPIV measurements are especially difficult in a DMSJ due to the high-temperature, the presence of combustion, large velocity gradients, and window fouling. The flow field inside a DMSJ is highly three-dimensional and thus all components must be measured to fully understand mixing and combustion processes. In addition, few authors have reported reliable higher-order turbulent statistics due to low image acquisition numbers or were able to accomplish measuring all three components of velocity through windows. Measurements of external flows present a distinct advantage to those viewed through windows due to the absence of window fouling and laser reflections. While external measurements are useful, a much more detailed understanding of the internal flow is necessary for the development of DMSJ technology.

The implementation of the SPIV technique to measure the 3D flowfield of a scramjet combustor was developed by Smith et al [31, 34]. While some successful

experimental data was collected, this work's primary impact was the experimental design and development of SPIV for this particular type of flowfield. A major contribution was the optimization of experimental parameters and development of an iterative design procedure. The work focused on the comparison of two situations: fuel-air mixing only (no combustion), and combusting cases. These comparisons allowed for studies of the effect of heat release on mixing. The work of Smith et al. did not examine the effect of mode transition on the velocity field. The changes in the velocity field, associated with fuel injection, mixing, and combustion, that take place during the DMSJ mode transition were therefore not identified. These measurements were conducted on a different flow path and no quantitative comparison with the current numerical models was conducted. In addition, a major critique of PIV measurements conducted at the UVaSCF has been the issue of velocity bias which is also addressed by the current study.

1.4 Dissertation Overview

The dissertation continues with Chapter 2, which describes the UVaSCF experimental facility and presents an overview of the significant hardware design that was necessary to accomplish the goals of the research. Next, Chapter 3 gives an overview of the basic PIV principles along with the additional requirements of SPIV. In addition, the optical hardware and particle seeding method are described. The SPIV experimental configurations for the four measurement plane locations are explained in Chapter 4. The results begin with Chapter 5, which focuses on the measurement of velocity bias errors due to the seeding method and presents the measurement uncertainty analysis. The main results are presented in Chapter 6 at the measurement locations x/H=6 and x/H=12 in the

combustor section and x/H=82 at the engine exit plane during both modes of combustion. Throughout the dissertation, axial locations (x) along the DMSJ flowpath are referenced from the base of the ramp fuel injector and normalized by H=0.25" (ramp height). Chapter 7 compares the SPIV velocity measurements to ongoing CFD efforts and Tunable Diode Laser Absorption Spectroscopy (TDLAS) measurements conducted within the NCHCCP. Finally, Chapter 8 gives a brief summary and future recommendations.

Chapter 2

Experimental Facility and DMSJ Hardware Design

In this chapter, the University of Virginia Supersonic Combustion Facility (UVaSCF) is described in detail. The different sections of the tunnel are described along with locations of key features of the flowpath. The facility operating conditions are presented and the fuel conditions for the experiment are established. The motivation for the design of new model hardware is discussed. Details of the design are reported including cooling, instrumentation locations, and material choices. In addition, the design of diagnostic specific hardware is presented.

2.1 University of Virginia Supersonic Combustion Facility

The DMSJ flowpath is tested experimentally in the University of Virginia Supersonic Combustion Facility with a Mach 2 nozzle. The experimental facility is an electrically heated, continuous flow, direct-connect wind tunnel that is fully described elsewhere [35, 36]. A schematic of the facility is given in Fig. 2.1.

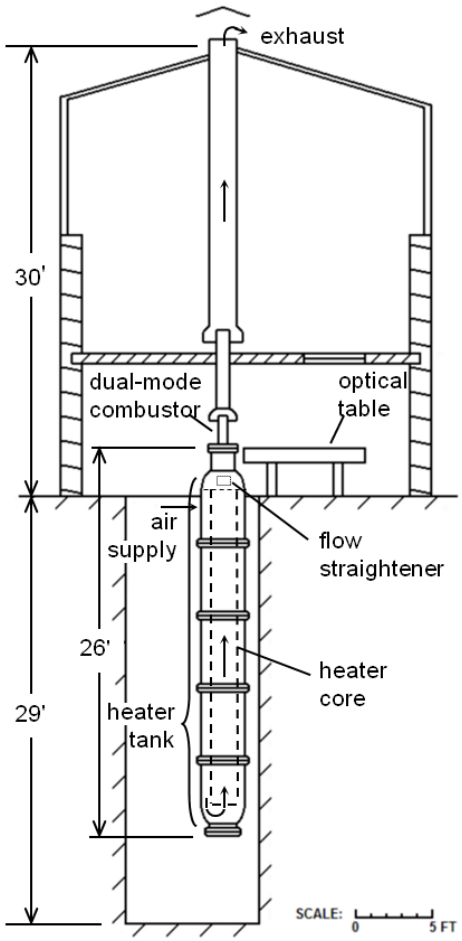

Figure 2.1: University of Virginia Supersonic Combustion Facility schematic [36].

The UVaSCF flow conditions simulated Mach 5 flight enthalpy conditions of a theoretical hypersonic flight vehicle by operating at a total temperature of 1200 K. The incoming freestream air to the flight vehicle is compressed and decelerated through shocks off the forebody and inlet, at which point the flow entering the isolator would be approximately Mach 2 depending on the aerodynamic geometry of the vehicle. The combination of the facility Mach number and length of the isolator allow a range of combustor entrance Mach numbers in order to simulate the ramjet and scramjet mode of operation. The facility is vertically mounted and the test section is conveniently located at optical table level for measurements. The heated, clean air is achieved by introducing the

supply air at the top of the heater tank at which point the air travels down the outer annular section and then back up through a series of 14 electrical resistance heaters. The heated air, at a specified total temperature and pressure, is then delivered through a two-dimensional facility nozzle which accelerates the flow to Mach 2 at the entrance to the isolator. Fuel is introduced in the combustor section and the hot burning gas exhausts to the room atmosphere, where it is directed outdoors through a large diameter metal pipe. Since the facility is electrically heated, the flow is free of any contaminates such as water or carbon dioxide, which are present in combustion-preheated facilities. The continuous flow capability allowed unlimited testing duration, but typical run times were on the order of hours with steady state heating and fuel conditions. Long-duration testing enables the acquisition of an adequate sample size of measurements to ensure statistical convergence of mean velocity and root-mean-square (RMS) velocity. The facility flow conditions are presented in Table 2.1. The equivalence ratio, φ, is defined as the ratio of the actual fuel/air ratio to the stoichiometric fuel/air ratio. The hydrogen auto-ignited at both fuel conditions listed and therefore a fuel-air mixing only case could not be studied and no ignition source was necessary. The scramjet mode of operation was simulated with $\varphi=0.18$ and the ramjet mode of operation was simulated with $\varphi=0.49$. Since the mass flow rate of the facility nozzle cannot vary significantly, the mass flow rate of the fuel is adjusted to achieve the proper ratio between air and fuel. Both the variability in facility flow conditions and the measurement device accuracy are included in the stated uncertainty values.

Table 2.1: Facility test conditions (Configuration C)

Parameter	Air	Uncertainty	Fuel		Uncertainty
Equivalence ratio, φ			0.18	0.49	±5%
Total pressure (kPa)	300	±1%	472	1278	±3%
Total temperature (K)	1200	±0.8%	300	300	±3%
Mach number*	2.03	±1%	1.7	1.7	±0.5%
Static pressure*	37	±1.4%	94	259	±3%
Static temperature*	709	±1%	190	190	±3%

The properties at the nozzle exit, and denoted with a star, were determined using nozzle areas and isentropic flow assumptions according to Eqn. 2.1-2.2 with the specific heat ratio, $\gamma = 1.4$, for hydrogen, and $\gamma = 1.34$ for air.

$$\frac{T_0}{T} = 1 + \frac{\gamma - 1}{2} M^2 \tag{2.1}$$

$$\frac{p_0}{p} = \left(1 + \frac{\gamma - 1}{2} M^2\right)^{\gamma/\gamma - 1} \tag{2.2}$$

In Eq. 2.1 and 2.2 the variables are defined as total temperature, T_0, static temperature, T, Mach number, M, total pressure, p_0, and static pressure, p.

2.1.1 DMSJ Model Flowpath

The flowpath of interest for the study was designated Configuration C and has been studied extensively within the National Center for Hypersonic Combined Cycle Propulsion through both experiments and computational modeling [35, 36, 37, 38]. A schematic of the flowpath is illustrated in Fig. 2.2 with the side view above and the top view below.

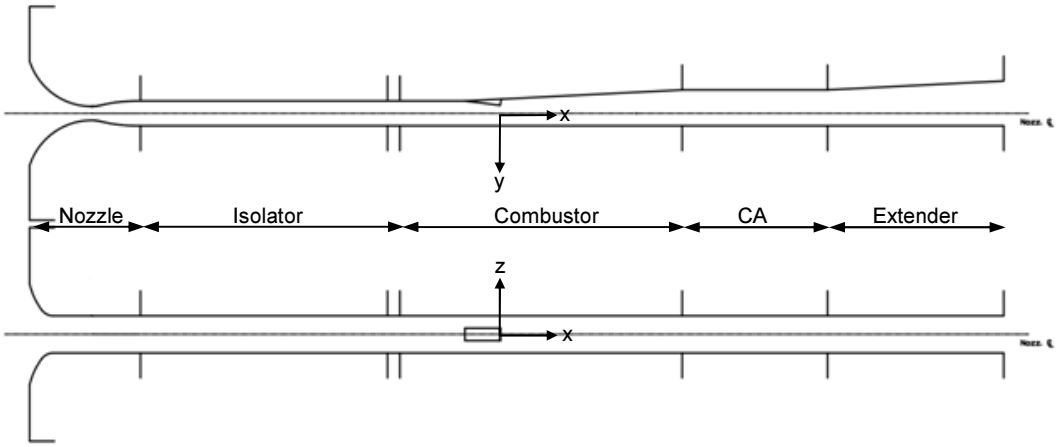

Figure 2.2: Configuration C flowpath schematic side view and top view.

The flowpath consisted of a nozzle, isolator section, combustor section, constant area section, and extender section. The flowpath was two-dimensional and the area from the isolator entrance to the extender exit is rectangular in shape. The isolator entrance area was 1" x 1.5" and the flowpath remains straight until the point of divergence on the combustor-side wall at the leading edge of the ramp. The combustor section features a 10° unswept compression ramp that was 0.5" wide and 0.25" high. Hydrogen fuel was injected through a Mach 1.7 conical nozzle located at the base of the ramp and is parallel to the face of the ramp. The injection-side wall diverges at an angle of 2.9° starting at the leading edge of the ramp and this is maintained until the constant area section, followed by a continuation of divergence in the extender. The DMSJ flowpath terminated with an atmospheric backpressure at the exit.

2.2 DMSJ Hardware Design

To meet the goals of the National Center for Hypersonic Combined Cycle Propulsion, several new test section components were necessary. The optical access in

the previous generation DMSJ flowpath was very limited and did not allow full field of view. Therefore a new modular combustor, constant area section, and extender section were designed with specific features intended for optical measurements. The design requirements were as follows:

- Independent sections that could be removed or replaced
- Able to interface with existing sections such as nozzle and isolator
- A fully modular combustor section capable of housing different fuel injectors, fuel injection walls, and side walls
- Full duct height optical access and maximum optical access in the axial direction in the combustor section
- Minimum window frame obstruction for optical access
- Modular windows for quick and easy cleaning or replacement
- High temperature gaskets to seal window frames
- Capable of an air-tight seal with o-rings and grooves
- Internal water cooling channels to minimize thermal deformation
- Capable to apply optical-based laser diagnostics through windows and slotted walls

The focus of the flowpath design was the modular combustor which was capable of housing multiple fuel injection walls, full field-of-view windows, and slotted walls for point measurements using Coherent Anti-Stokes Raman Scattering (CARS). The existing nozzle and isolator were the only sections that did not require a complete redesign, but for completeness they are described. The following sections describe the hardware design and present the key features of the hardware.

2.2.1 Mach 2 Nozzle Block

The facility nozzle is a 2-dimensional Mach 2 nozzle. Fig. 2.3 shows an isometric view of the nozzle and cross-sectional views through the z and y-axis.

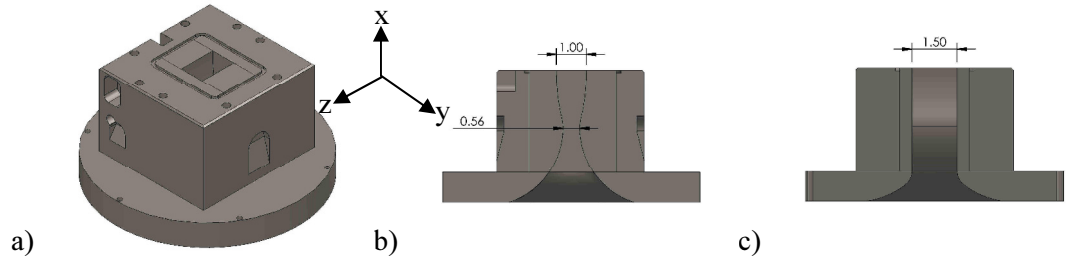

Figure 2.3: Nozzle block solid model assembly: a) isometric view, b) cross-sectional view though the y-axis, c) cross-sectional view though the z-axis.

The nozzle contour is evident in Fig. 2.3(b)/(c), with a throat area of 0.86 in^2 and an exit area of 1.5 in^2. The area ratio, $A/A^*=1.79$, between the exit area and throat area gives a Mach number equal to 2.03 based on equation 2.3 which assumes compressible, isentropic flow.

$$\left(\frac{A}{A^*}\right)^2 = \frac{1}{M^2}\left[\frac{2}{\gamma+1}\left(1+\frac{\gamma-1}{2}M^2\right)\right]^{(\gamma+1)/(\gamma-1)} \tag{2.3}$$

The nozzle is constructed of nickel and all parts are brazed together to form a solid part. Several internal ethylene glycol cooling channels are drilled throughout the metal walls but are not shown in the figure for clarity. The o-ring groove on the top of the nozzle is sized for a standard 236S070 silicon o-ring and seals with the isolator section with 3/8-16 unified coarse threaded (UNC) tapped holes.

2.2.2 Isolator Section

The isolator section is 9.97" long and constructed from 4 walls with straight interior sides to form a constant area duct with dimensions of 1" x 1.5". An exploded view and assembly of the isolator section solid model is presented in Fig. 2.4.

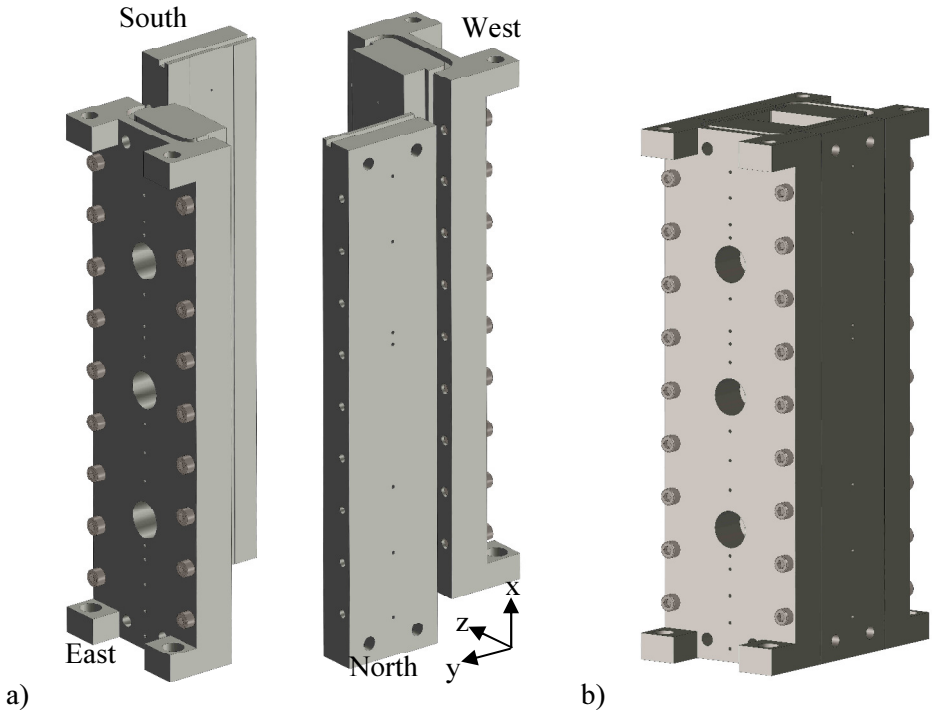

Figure 2.4: Isolator section solid model: a) isometric exploded view, b) isometric assembly.

The walls are defined in cardinal directions relative to the orientation of the DMSJ hardware in the laboratory. The east and west walls clamp the north and south walls with 10-32 UNC bolts which serve to compress the vertical o-ring (S070). The vertical o-rings meet at the top and bottom of the part and join with the nozzle o-ring and top isolator o-ring in order to achieve a complete air tight seal. All four walls of the isolator are coated with a 0.015'' thick Zirconia thermal barrier coating. Each wall featured two vertical internal cooling passages which are joined at the top with external tubing to form a closed loop. The primary instrumentation was located on the combustor side (west) wall and

consisted of low frequency surface pressure taps (PT), high frequency Kulite surface pressure taps (KPT), and subsurface thermocouples (TC). The instrumentation location is listed in Table 2.2.

Table 2.2: Isolator section instrumentation locations.

Distance from Fuel Injector (x/H)	Wall	Type
-57.088	East / West	PT
-55.129	West	PT
-53.088	West	PT
-51.088	West	PT
-50.129	North / East / South / West	TC
-48.088	East / West	KPT
-45.133	West	PT
-42.888	West	PT
-40.688	West	PT
-38.088	East / West	KPT
-35.488	West	PT
-34.135	North / East / South / West	TC
-33.133	West	PT
-30.688	West	PT
-28.088	East / West	KPT
-26.137	North / East / South / West	TC
-25.088	West	PT
-23.088	West	PT
-21.110	West	PT

Three high-frequency Kulite pressure taps were evenly spaced throughout the isolator section for the purpose of measuring the pressure fluctuations due to the shock train in ramjet mode. The isolator section attached to the combustor section through the intermediate isolator-combustor adaptor plate discussed below.

2.2.3 Isolator-Combustor Adaptor Plate

Due to the large footprint of the combustor cage, to be discussed in the next section, an adaptor plate was necessary to interface the isolator and the combustor cage. Two of the connecting tabs did not match between the isolator and combustor cage, and therefore

a plate with six tabs total enabled the parts to mate. The adaptor plate was 0.5 inches thick and had the same flowpath dimensions as the isolator of 1 x 1.5 inches. An isometric view and a transparent view showing the cooling channels are illustrated in Fig. 2.5.

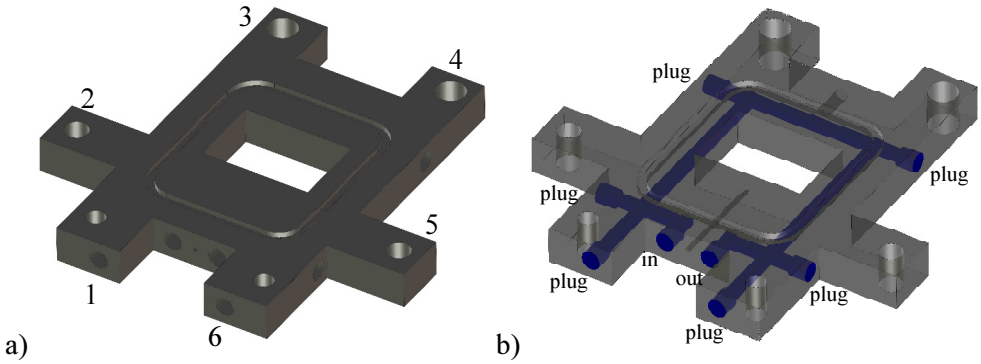

Figure 2.5: Isolator-combustor adaptor plate solid model: a) isometric view, b) transparent view with cooling channels highlighted in blue.

Tabs 1, 3, 4, and 6 were utilized to bolt the isolator to the adaptor plate. Two 5/16-20 UNC bolts were passed up through the corresponding isolator tabs and attached to threaded holes in tab 1 and 6. Two 3/8-16 UNC bolts were passed down through the corresponding tabs in the combustor, then pass through tabs 3 and 4 which finally attached to threaded holes in the corresponding isolator tabs. Tabs 2 and 5 were threaded and allowed the combustor cage to attach to the adapter by utilizing the corresponding tabs in the combustor cage. The cooling passage inlet and exit were on the west side wall and the remaining holes were plugged and brazed to form a closed loop which traversed all four sides of the part. There was one low frequency pressure tap located on the west wall centerline of the adaptor plate at an axial location of x/H = -17.216. In addition, there was an external thermocouple at the same axial location on the east wall. The adaptor plate was machined from a solid piece of stainless steel and no Zirconia coating

was applied to the flowpath side. The adaptor plate sealed with the bottom of the combustor cage with a standard silicon (144S070) o-ring.

2.2.4 Combustor Cage

The most essential part of the Modular Supersonic Combustion Tunnel (MSCT) was the combustor cage structure which was the platform for enabling optical access through three walls of the combustor section. The primary advantage of a cage structure was that various walls can be inserted in order to form the flowpath. For example, the combustor cage was capable of housing various fuel injection walls, fuel injector inserts, side windows/frame assemblies, slotted side walls, a solid observation wall, and an observation window wall. The combustor cage enabled complete flowpath modularity and the specific configuration could be optimized to the diagnostic technique. The combustor cage did not require the removal of any other sections in order to exchange any of the combustor flowpath walls. This was convenient for cleaning windows or quickly transitioning to another optical diagnostic. Figure 2.6 shows an isometric view of the cage as well as the internal cooling channels highlighted in blue.

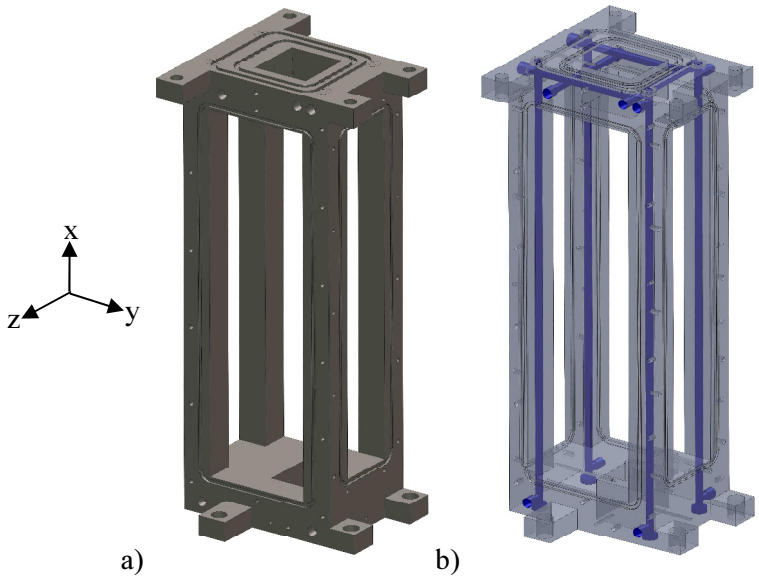

Figure 2.6: Combustor cage solid model: a) isometric view, b) transparent view with cooling channels highlighted in blue.

The combustor cage was machined from a solid piece of stainless steel which required Electrical Discharge Machining (EDM) of the flowpath walls in order to achieve non-rounded interior corners. The tabs on the bottom of the combustor cage were designed such that the part can be bolted directly to the existing bolt pattern on the nozzle block or the isolator section. The tabs on the top of the combustor cage were moved outward to create more space for optical access. Each vertical column of the combustor cage contained a cooling channel with an inlet at the bottom and exit at the top flange. At the top flange, a u-shaped loop was formed with the horizontal cooling channels. An additional horizontal cooling channel was machined below the u-shaped loop along the combustor side wall to provide protection from the burning flame which anchors to that side. Four large o-ring grooves were machined along the vertical columns to create a seal with any side walls. Low frequency pressure taps were located on all four sides of the

combustor cage at x/H = -15.216. In addition, there were low frequency pressure taps on the fuel injection-side wall at x/H = -13.416, 26.544, and 28.344.

Fig. 2.7 illustrates how the flowpath was formed through an exploded view of the combustor cage with the fuel injection wall, ramp fuel injector insert, side windows, and observation window wall.

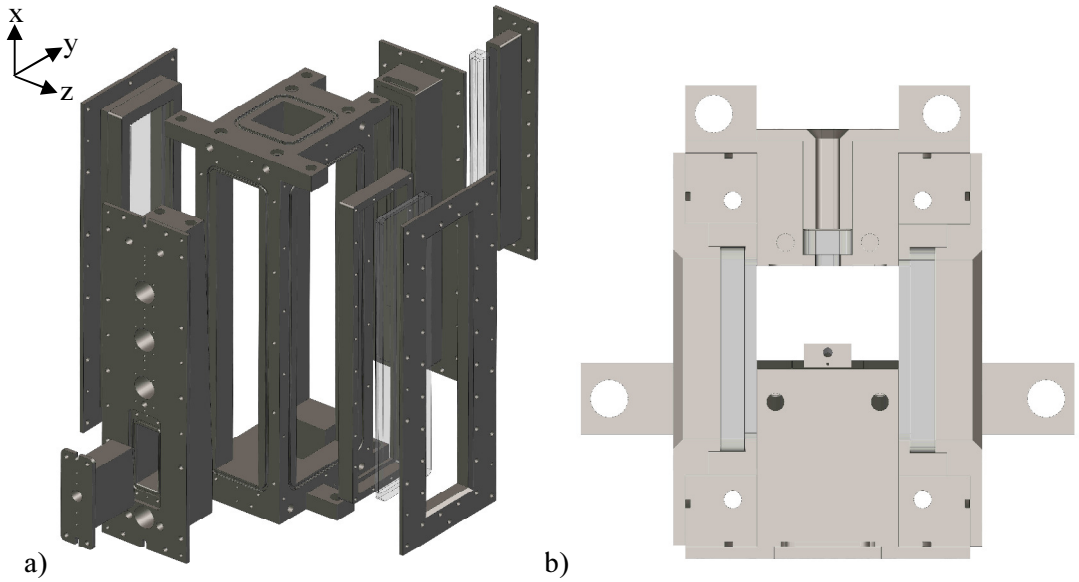

Figure 2.7: Combustor section solid model assembly: a) exploded view including the combustor side wall, fuel injector insert, side window frame assemblies and observation window frame assembly, b) Top view cross-section assembly.

Each flowpath wall featured a flange which bolted to the exterior cage surface with 6-32 UNC bolts which compress the o-ring, creating a seal. Due to limited space on the vertical columns of the combustor cage, custom o-rings were necessary, with sizes 7.27x.07 S070, 7.95x.07 S070, and 6.9x.07 S070, on the north/south wall, fuel injector wall, and observation side wall respectively. The clearance between all walls and the cage opening was 0.005 inches for a tight fit with any physical disturbance to the flow minimized. To prevent contact of glass on metal, a 0.040 inch thick alumina paper was inserted between the interior glass surface and the corresponding area of the observation

wall and fuel injection wall. The width of the window in the y-direction has been oversized to accommodate different fuel injection walls for future testing. The fuel injection wall and insert, window frame assemblies, and observation window wall will be discussed in more detail below. The cross-section in Fig. 2.7(b) illustrates how the combustor section is assembled and the extent of the optical access in reference to the flowpath.

2.2.5 Fuel Injection Wall and Ramp Fuel Injector Insert

The fuel injection wall was designed to accommodate various fuel injector inserts to meet the goal of modularity. The flowpath side of the fuel injection wall is straight for 1.625 inches, beyond which point, 2.9° divergence exists throughout the combustor section. An isometric view of the fuel injection wall with the fuel injector insert installed is shown in Fig. 2.8. Note that the ramp leading edge was aligned with the point of divergence.

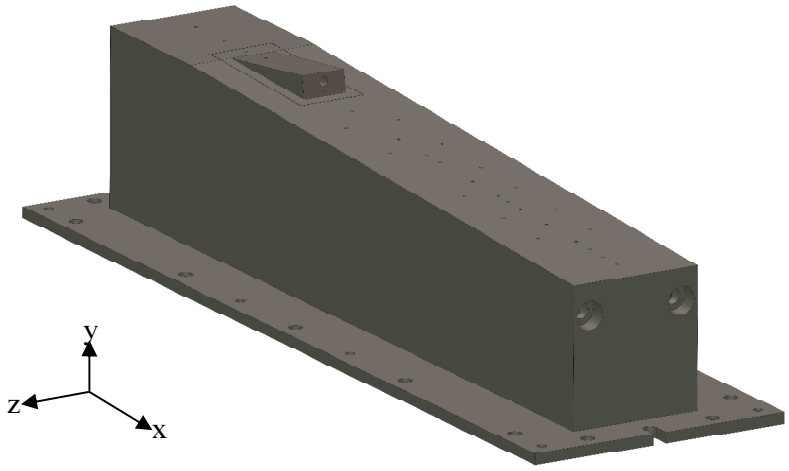

Figure 2.8: Fuel injection wall with ramp fuel injector insert assembly (isometric view).

Two straight internal cooling channels ran the length of the fuel injection wall and were located nearest to the flowpath surface. In addition, the entire flowpath surface of the fuel injection wall and fuel injector insert received a 0.015 inch thick Zirconia coating to protect the part from high thermal loading. The combustor section was the area of focus for the optical diagnostics; therefore, extensive pressure and temperature instrumentation is dedicated to the fuel injection wall. A cross-sectional view of the assembly along the centerline of the y-axis is presented in Fig. 2.9.

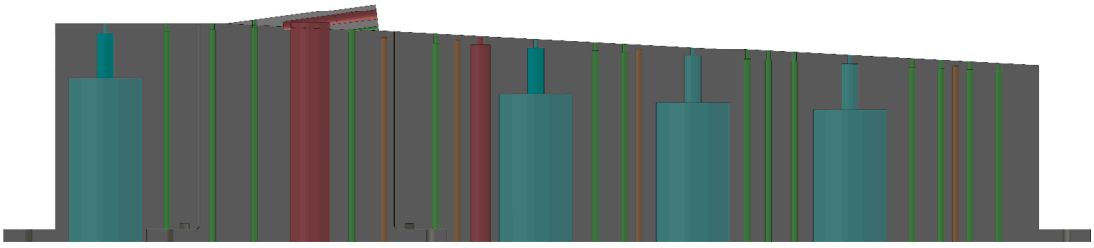

Figure 2.9: Fuel injection wall cross-sectional view (with high frequency pressure taps colored blue, low frequency pressure taps colored green, sub-surface thermocouples colored orange, and the fuel and igniter flowpath colored red).

Low frequency pressure taps are colored green, subsurface thermocouples are colored orange, high-frequency Kulite pressure taps are colored blue, and the hydrogen flowpath and igniter are colored red. In addition to the centerline low frequency pressure taps there were off-centerline pressure taps located upstream and downstream of the Kulite pressure taps. The Kulite pressure tap upstream of fuel injection was located at the most upstream position with optical access in order to experimentally quantify the combustor inflow conditions. The three Kulite pressure taps downstream of fuel injection were located at x/H = 6, 12, and 18, and defined the primary laser-based optical measurement planes. The instrumentation locations of the fuel injection wall and fuel injector insert are presented in Table 2.3.

Table 2.3: Combustor section instrumentation locations.

Distance from Fuel Injector (x/H)	Wall	Type
-10.316	Combustor	KPT
-7.964	Combustor	PT
-6.216	Fuel Injector Insert	PT
-4.616	Fuel Injector Insert (ramp face)	PT
0.004	Fuel Injector Insert (ramp base)	PT
0.336	Combustor	TC
2.436	Combustor	PT
3.124	Combustor	TC
4.008	Combustor (N/S)	PT
6	Combustor	KPT
7.540	Combustor (N/S)	PT
8.408	Combustor	PT
9.508	Combustor	PT
10.060	Combustor	TC
10.712	Combustor (N/S)	PT
12	Combustor	KPT
13.540	Combustor (N/S)	PT
14.208	Combustor	PT
15.008	Combustor	PT
16.008	Combustor	PT
16.712	Combustor (N/S)	PT
18	Combustor	KPT
19.540	Combustor (N/S)	PT
20.508	Combustor	PT
21.608	Combustor	PT
22.160	Combustor	TC
22.708	Combustor	PT
23.808	Combustor	PT

2.2.6 Window Frame Assemblies

The combustor side window frame assembly and observation window frame assembly solid model are shown in Fig. 2.10. The combustor side window frame was a three part construction consisting of the back frame, window, and front frame.

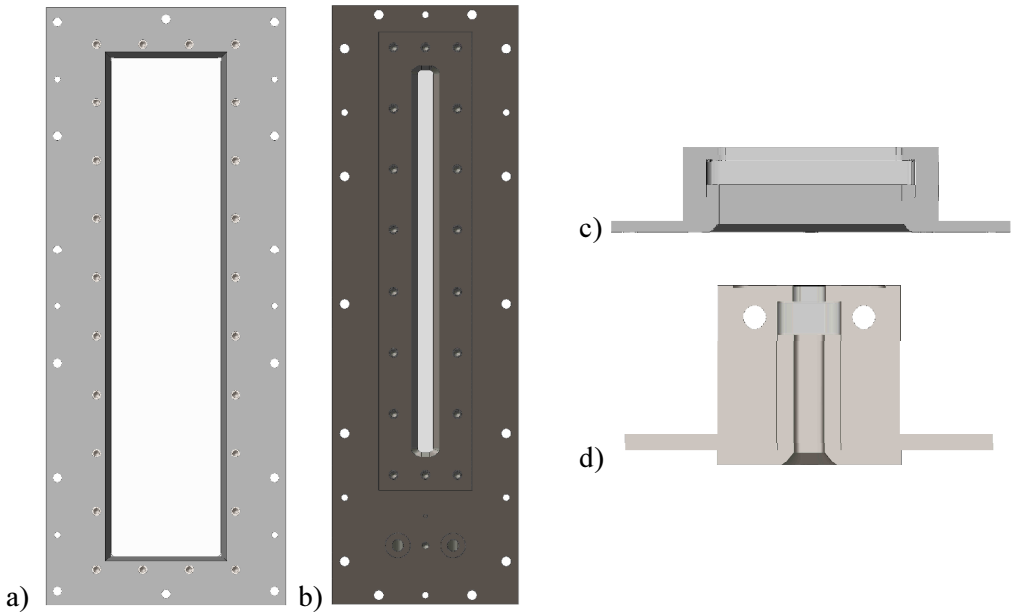

Figure 2.10: Combustor section side window frame assembly and observation window assembly: a) Side window frame assembly, b) Observation side window frame assembly, c) Side window frame cross-section, d) Observation window frame cross-section.

The back frame and front frame squeezed the glass window which “floated” and no metal-to-glass contact was made. Alumina gasket paper was inserted into the gaps between the window surface and the frame surface and after compression the gap was .01" on either side of the window. There was .0125" clearance between the window side/top and the corresponding part of the window frame. The clearance was necessary to allow some thermal growth of the metal window frames to avoid metal to glass contact. Initial testing of the side window frame assembly led to failure of windows caused by deformation of the stainless steel frames due to thermal loads. To solve this problem, a new back frame was machined out of titanium to minimize thermal deformation. The titanium window frame was assessed using Finite Element Analysis which predicted thermal stresses in the window well below failure [41].

Due to higher thermal loads on the observation side of the combustor, the observation window assembly needed to be actively water cooled. In this case, the back

frame was constructed from stainless steel and two vertical cooling channels that surround the window greatly reduced the temperature of the part. The depth of the observation window frame was significantly larger than the side windows which allowed for the vertical cooling channels. The observation window is only ¼ in. on the flowpath side which is suitable for delivering a laser sheet for optical measurements. The observation window was likewise sealed with Alumina gasket paper.

2.2.7 Constant Area Section

The constant area (CA) section was machined from stainless steel and measures 5.87" long. The main structure of the constant area cage is shown in the exploded view in Fig. 2.11(a) and as an assembly in Fig. 2.11(b). The flowpath cross-sectional area was 1.5" x 1.44". The constant area section shown was initially designed to accommodate optical access with wall-to-wall windows on all four walls.

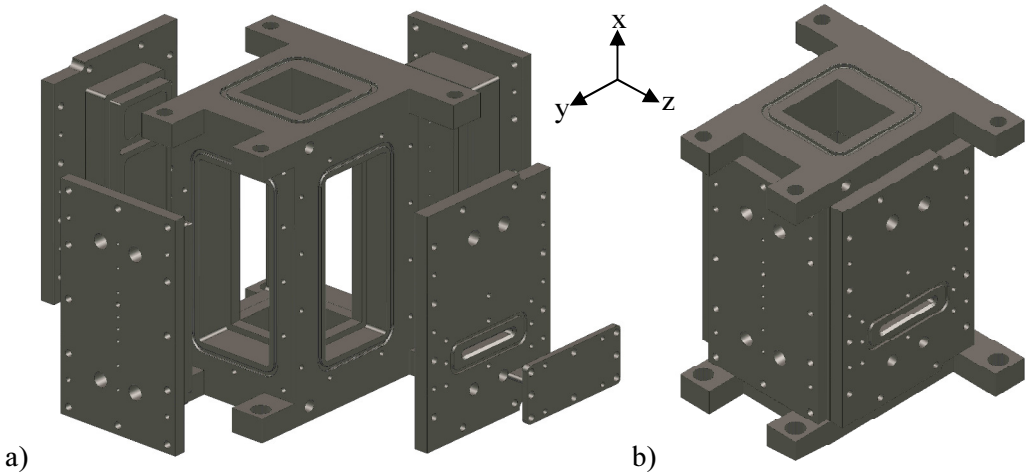

Figure 2.11: Constant area section solid model a) exploded isometric view with solid side walls, b) assembly isometric view.

The only way to accomplish this goal was to create a flowpath with constant area, discontinuing the 2.9° divergence which was observed on the combustor side wall.

To design a window and frame assembly with divergence would have been impractical and the expense outweighed the benefit. Upon initial testing, high-strength ceramic blanks could not survive the harsh temperatures present in the constant area section. A thermal throat present in the ramjet mode of combustion is located in the CA section, causing peak temperatures in the flowpath. Therefore, all subsequent testing of Configuration C took place with 4 solid, actively cooled walls inserted in the constant area section.

The constant area section cage was similar in design to the combustor cage but was shorter, at 5.87 inches long. The vertical columns of the cage were cooled in a similar fashion as the combustor cage. One of the key differences was the shape of the vertical columns which were necessary to accommodate full optical access. The vertical columns were not rectangular and feature a step towards the corners to allow the installation of a window. Therefore, unlike in the combustor section, inner frames were not utilized in the CA section. Instead, the vertical columns of the CA cage act as physical barriers to mount the windows. This is evident in Fig. 2.12 which presents the cage assembly cross-section.

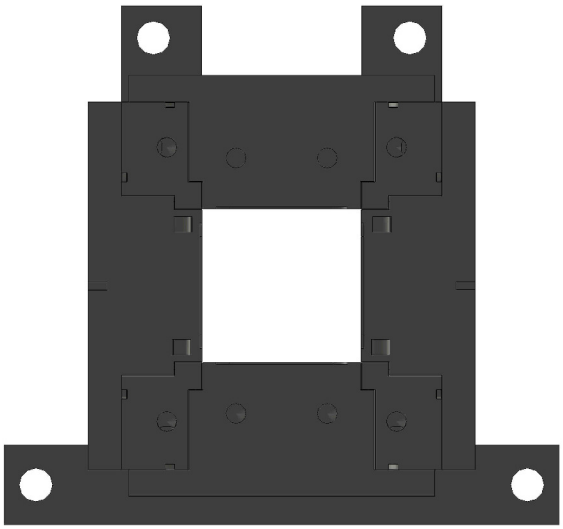

Figure 2.12: Constant area section solid model assembly top view cross-section.

Similar to the combustor section, all four CA section solid walls featured a flange that bolted to the cage and compressed the o-rings to create a seal. Vertical cooling channels on all four CA solid walls and the CA cage can be seen in Fig. 2.12. The CA section solid walls have one slot machined to accommodate CARS measurements. In addition, the fuel injection-side CA section solid wall was instrumented according to Table 2.4.

Table 2.4: CA section instrumentation locations.

Distance from Fuel Injector (x/H)	Wall	Type
35.032	West	PT
37.032	West	PT
41.032	West	PT
42.032	West	TC
42.032	East	ETC
43.032	West	PT
45.032	West	PT
47.032	West	OT

2.2.8 Extender Section

The extender section was constructed from stainless steel and is 7.09" long with an entrance flowpath area of 1.5" x 1.44". The 2.9° divergence resumed within the extender

on the combustor-side wall resulting in an exit area of 1.5 x 1.80 inches. The extender was constructed from 4 solid walls that bolted together to form the flowpath. Fig. 2.13(a) shows an exploded view of the four walls and Fig. 2.13(b) shows the extender assembly.

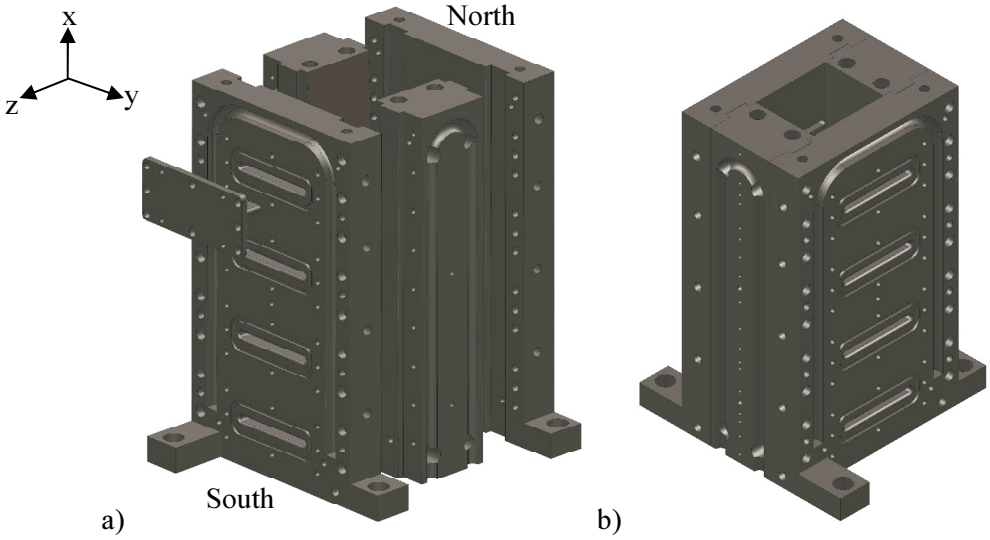

Figure 2.13: Extender section solid model: a) Exploded view with slot plug, b) Assembly isometric view.

The extender north and south side walls were mirror images of each other about the y-axis. The north and south walls featured a groove to accept the tongue of the east and west wall. This groove served the purpose of creating a recess for a high-temperature furnace cement which acted to seal the assembled extender. The north and south walls mated together with the east and west walls with 10-32 UNC bolts which compressed the furnace cement and therefore no o-rings were used to seal the assembly. The tongue and groove also assisted in alignment of the parts. More precise alignment is achieved with four alignment pins on the north and south sides with a tight tolerance of ± 0.001 inches.

The north and south walls featured an external u-shaped cooling loop in which a ¼ inch diameter copper cooling tube was brazed in the 1/8 inch radius groove on the outer surface of the wall. The north and south walls also featured a serpentine cooling loop

which traveled in the y-direction and externally connected in order to cool the metal between the slot locations. The serpentine loop was necessary to accommodate the slotted side walls for laser diagnostics. The east and west wall both featured two vertical internal cooling passages. All internal cooling channel inlets and outlets connected with National Pipe Thread (NPT) fittings so that no brazing process was necessary. Only the east and west walls received a 0.015 inch thick Zirconia coating due to the challenge of coating the slotted surfaces. The slot height was 0.125 in. and enable laser point measurement techniques such as CARS. The slots were located at x/H = 58.134, 62.634, 69.136, 75.652, and the instrumentation locations are presented in Table. 2.5.

Table 2.5: Extender section instrumentation locations.

Distance from Fuel Injector (x/H)	Wall	Type
53.528	West	PT
55.120	West	PT
56.400	West	PT
57.128	West	PT
58.128	West / East	ETC
59.136	West	PT
61.120	West	PT
61.732	West	TC
62.916	West	PT
64.720	West	PT
67.132	West	PT
68.332	West / East	ETC
69.420	West	PT
71.140	West	PT
72.736	West	PT
73.728	West	TC
75.920	West	PT
76.740	West	PT
77.744	West	PT
80.540	West	PT

The extender section is the final hardware section that completes the DMSJ assembly. A full assembly of the Configuration C DMSJ hardware is presented in Fig. 2.14.

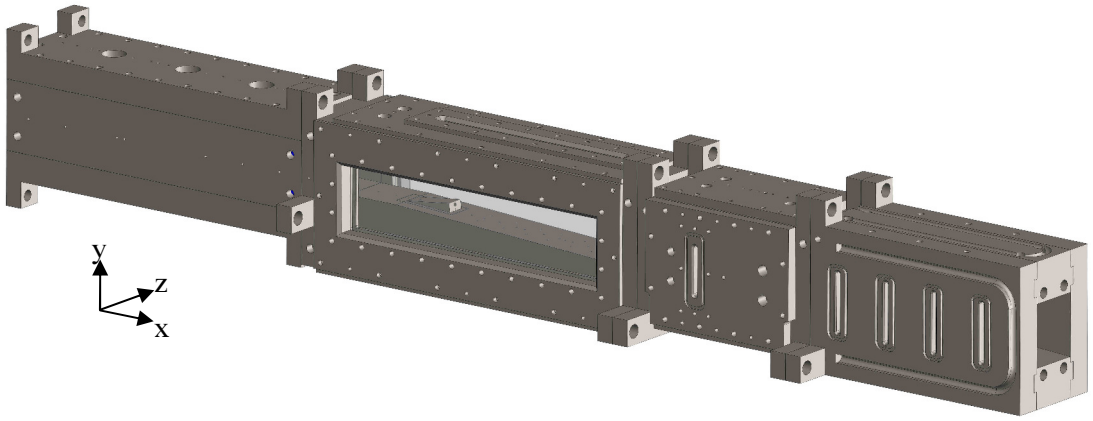

Figure 2.14: Configuration C Modular Supersonic Combustion Tunnel.

For planar streamwise measurements, a laser sheet can be delivered through the observation side window in the x-y plane and a camera can view through the side windows. For planar transverse measurements, the laser sheet can be delivered through the side windows perpendicular to the flow in the y-z plane with cameras viewing from above or below at an oblique angle. In addition, the flowpath enables line-of-sight and point laser measurements throughout the combustor and at the specified slot locations in the CA section and extender section.

Chapter 3

SPIV Background and Experimental Equipment

First, a general description of the basic PIV theory is given. The concepts of the 2D PIV method are discussed including the critical components of a PIV experiment. Next, the extension of the PIV theory to a Stereoscopic PIV setup in order to measure 3 components of velocity is discussed. Some of the optical constraints and necessary conditions are presented. Lastly, the optical equipment is presented and the subsystems, such as laser deliver system, camera systems, and seed delivery systems, are described.

3.1 Particle Image Velocimetry (PIV): Theory

The four main components to a classic PIV experimental setup are a double-pulsed laser sheet, tracer particles, cameras, and correlation software. An illustration of the PIV experimental method, as applied to the DMSJ flowpath, is depicted in Fig. 3.1.

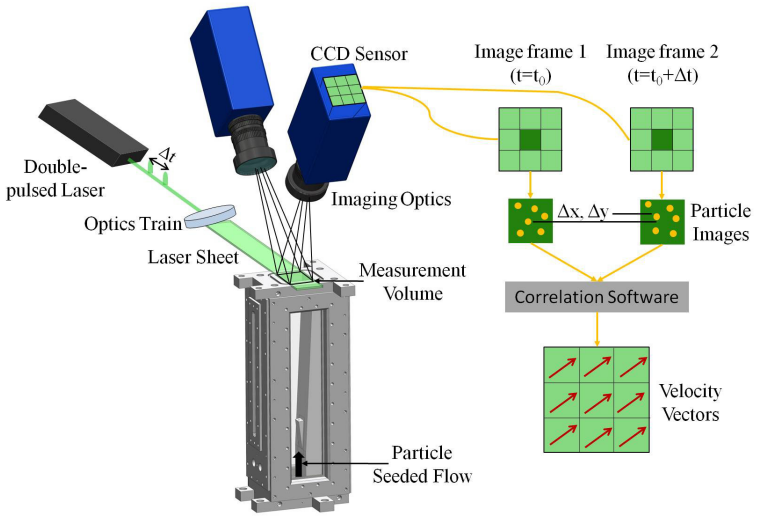

Figure 3.1: PIV experimental components diagram.

The double-pulsed laser sheet is formed through the use of several cylindrical lenses which collimate the width and/or thickness of the sheet. The flow is seeded with sub-micron tracer particles that are used to track the flow. Two particle image pairs must be captured by the cameras during two distinct laser pulses separated by a small time delay, Δt. The image pairs are broken down into interrogation sub-regions where a cross-correlation algorithm determines the most likely displacement in two directions. Lastly, the entire vector field is calculated by combining the displacement and time information.

Particle Image Velocimetry relies on several concepts and assumptions. PIV is a non-intrusive, indirect, planar measurement technique. This means that there is an assumption that the particles added to the flow do not impart any disturbances and are not chemically reactive. PIV is indirect because the technique does not directly measure the fluid velocity but instead relies on particles to faithfully track the flow. The planar nature of the PIV technique allows whole field imaging and thus measurement of velocity at a particular interrogation sub-region. Therefore it is necessary to break an image up into small interrogation sub-regions in order to measure displacement [42]. It is assumed that all the particles within an interrogation sub-region have a homogeneous displacement. The spatial resolution of the technique is defined by the size of an interrogation sub-region and the percent overlap between sub-regions.

There are also several concepts and assumptions regarding the illuminating light source. A high powered, coherent laser is necessary as the light source in order to achieve adequate scattering from small particles. It is assumed that the duration of a single laser pulse is short enough to effectively freeze the particles in time. The time delay between laser pulses must be long enough to allow the tracer particles to move an adequate

distance to statistically measure displacement but also short enough to prevent particles from moving through the laser sheet [43].

Regarding particles, there exists a particle velocity lag between that and the fluid. The proper material and size of particles must be determined and analyzed to ensure faithful fluid tracing. This is increasingly important in flows with large velocity gradients or shocks. If the particle density is sparse, particle tracking velocimetry can be performed where individual particles are resolved in an image and displacement can be determined. If the particle density is dense, individual particles cannot be resolved and a correlation method must be used in order to determine the displacement of a group of particles in a particular sub-region. In addition, it is preferred that the particles are homogeneously distributed throughout the measurement area and that no particles accumulate in particular regions of the flow.

A basic 2D PIV setup with a camera viewing normal to the object plane and laser sheet is depicted in Fig. 3.2.

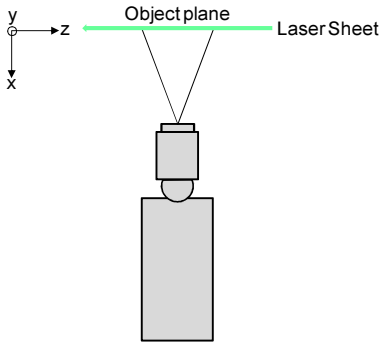

Figure 3.2: Single camera 2D PIV system

Fig. 3.2 shows a top view of the camera and the laser sheet which is delivered in the y-z plane with depth in the y-direction and thickness in the x-direction. In this orientation, both velocity components in the z and y-direction that lie in the plane of the laser sheet

can be determined. The camera is viewing in a side-scatter orientation with respect to the laser sheet. If optical restraints dictate a non-normal viewing angle, a calibration procedure is necessary to account for optical distortion [44]. In a 2D PIV setup, the laser sheet is very thin and it is assumed that out-of-plane velocity is minimal and therefore there is no through sheet particle movement. For a 2D PIV setup, calibration can either be performed by calculating the reproduction ratio of the lens or by using a dot pattern target to provide the dewarping of the image.

Due the interaction of the experimental parameters previously discussed, a set of guidelines for PIV measurements needed to be developed. In 1990, Keane and Adrian developed classic PIV design rules based on synthetic data [45]. Guidelines were developed to address the issues of particle density, in-plane motion, out-of-plane motion, spatial gradients, and peak detection. The PIV design rules are as follows:

1) The number of particle pairs per interrogation sub-region should be greater than 15
2) The in-plane motion of particles should be less than 25% of the interrogation region size
3) The out-of-plane motion of particles should be less than 25% of the sheet thickness
4) The velocity gradients within an interrogation sub-region should be less than 5% of the sub-region size
5) The peak detection ratio, defined as the ratio between the largest peak and the next largest peak, should be 1.2-1.5

The above rules developed by Keane and Adrian are useful for determining the proper laser pulse time delay. For example, assume a 2D PIV experimental with typical axial velocity of 1000 m/s, a reproduction ratio (magnification) of 1:1, and interrogation sub-regions of 32x32 pixels. In order to satisfy the in-plane motion criterion (2) the proper laser pulse time delay, Δt, would be 60 ns. Commercial pulsed lasers typically have a minimum Δt=100 ns, therefore a larger reproduction ratio would be necessary such that the particles do not have in-plane motion greater than 25% of the sub-region.

3.1.1 Correlation Methods for PIV

The two main correlation methods for PIV measurements are auto-correlation and cross-correlation. The auto-correlation method involves taking a double exposure of a single frame. The particle intensity from both the first laser pulse and second laser pulse (separated by Δt) are both recorded on the same image. This process is presented in Fig. 3.3.

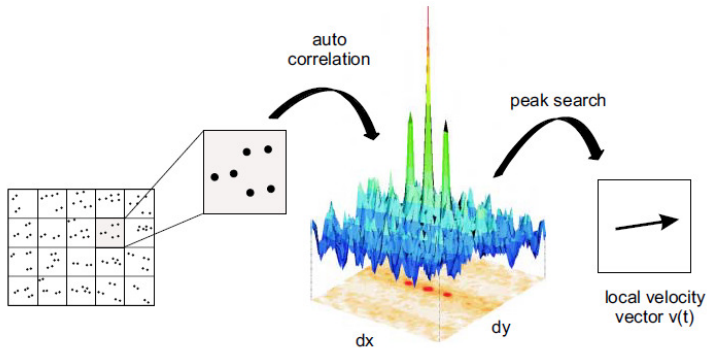

Figure 3.3: Auto-correlation procedure of a single frame double exposure [46].

Each image is divided into integration sub-regions of 124x124, 64x64, 32x32, or 16x16 pixels depending on the expected flow velocities. The displacement of the group of particles at each sub-region is indicated by the two secondary peaks symmetric about the

central peak corresponding to a zero displacement. Two peaks occur due to the inability of the auto-correlation method to detect direction. Therefore, the auto-correlation method can only be utilized for flows in which the flow directions are known a priori. Some weaknesses of the auto-correlation method include difficulty in detection of small displacements and relatively small correlation peaks compared to cross-correlation. This can be particularly problematic in situations where background noise is high and the displacement peaks cannot be detected.

The cross-correlation method involves the double exposure of a double frame. The intensity signal from the particles is recorded on the first frame during the first laser pulse and on the second frame during the second laser pulse (separated by Δt). The cross-correlation method is depicted by Fig. 3.4.

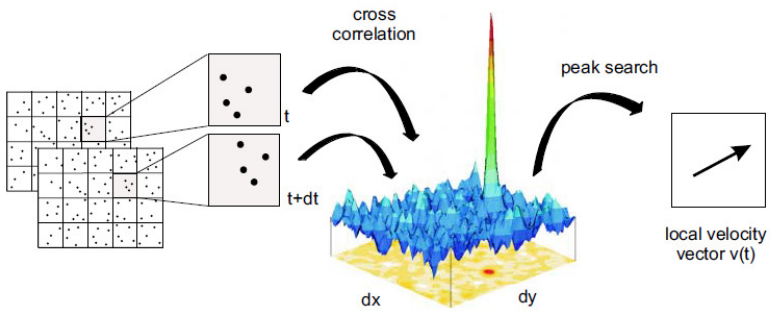

Figure 3.4: Cross-correlation procedure for a double frame double exposure [46].

Again the image is divided into interrogation sub-regions. For the cross-correlation method only one primary peak is detected which determines the displacement of the particles because direction is measured inherently in the process [47]. To filter out spurious vectors or images with strong background noise, a minimum peak detection

ratio, Q, defined as the ratio of the highest to second highest peak, is enforced. The formula for the correlation function is defined in Eqn. 3.1.

$$C(dx,dy) = \sum_{x=0,y=0}^{x<n,y<n} I_1(x,y)\, I_2(x+dx, y+dy) \tag{3.1}$$

In Eqn. 3.1, I_1 and I_2 are the image intensities of the first interrogation window and the second interrogation window with some dx and dy displacement. The correlation function indicates the correlation strength between the two interrogation windows, 1 and 2 and thus the most likely displacement vector. The correlation function uses a standard cyclic FFT-based algorithm that calculates the correlation of particle intensity from the first exposure with the second exposure at each interrogation window [48].

3.1.2 Stereoscopic Particle Image Velocimetry

Stereoscopic Particle Image Velocimetry (SPIV) is an extension of 2D PIV which enables the measurement of all three velocity components through the aid of two cameras viewing the measurement plane from oblique angles. Fig. 3.5 shows a typical SPIV setup and the method for determining the third velocity component, which is perpendicular to the sheet and acts in the x-direction.

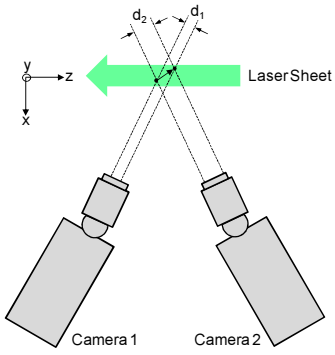

Figure 3.5: Two camera Stereoscopic PIV system (determination of third velocity component).

As was possible with the 2D PIV setup in Fig. 3.2, the components of velocity in the y- and z-direction can be determined with only one camera. By adding a second camera viewing from a different perspective, the third component of velocity in the x-direction can be measured. To prevent the situation in which the particles move through the sheet, a significantly thicker laser sheet is necessary for SPIV measurements as compared to 2D PIV. As shown in Fig. 3.5, the movement of the particle in the x-direction is viewed as having a larger displacement in camera 2 than camera 1. Based on the angle of the cameras relative to the laser sheet and the image-to-world calibration function, the velocity in the x-direction is resolved [49].

The calibration consisted of inserting a precise target pattern of dots perpendicular to the flow and parallel to the measurement plane. Both cameras image the target at the measurement plane and at a set distance above and below the measurement plane. The processing of raw PIV particle images consisted of the following steps:

1) Subtract the background intensity from an ensemble average of the background noise without particles.
2) Utilize a multi-pass interrogation scheme starting with an interrogation sub-region size of 128x128 pixels stepping down to 64x64 pixels and finally 32x32 pixels with 50% overlap and 5 passes at each sub-region size.
3) Apply the cross-correlation algorithm with a peak detection criterion of $Q<1.2$ (a vector is deleted if the peak ratio, Q, is less than 1.2).
4) Apply a 4 pass median filter which removes a vector if >2 times the RMS of neighbors and reinserts a vector if <3 times the RMS of neighbors in order to filter out spurious vectors. The filter is explained in detail by Nogueira et al [50].

5) Calculate vector and scalar statistics.

For an instantaneous PIV calculation, if a vector is rejected in one of the above steps, the sub-region is left blank and no vector interpolation is performed.

3.1.3 Scheimpflug Criterion

In a SPIV setup it is necessary for both cameras to view the measurement plane at oblique (non-normal angles). In this situation, the angle between the camera image plane and object plane creates distortion of the image and varying focus across the measurement plane due to a limited depth of field. In order to attain images completely in focus, the lens plane must tilt with respect to the image plane [49]. The angle for this condition to be met is such that the object plane, lens plane, and image plane all intersect in a common line. Fig. 3.6 shows a schematic of the necessary Scheimpflug criterion.

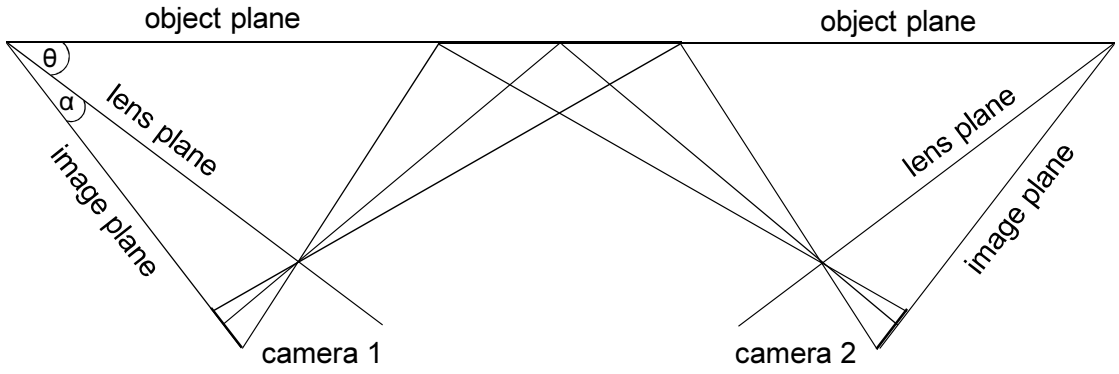

Figure 3.6: Scheimpflug condition optical arrangement schematic.

The angle between the object plane and lens plane is denoted θ and the angle between the lens plane and image plane is denoted α. The lens plane tilt angle is controlled by a Scheimpflug adapter that interfaces between the camera body and the lens. The lens plane tilt angle, α, can be calculated based on Eq. 3.2, where θ is defined as the angle between the object plane and lens plane and R is defined as the lens reproduction ratio.

$$\alpha = \tan^{-1}\left(\frac{\tan(\theta)}{R}\right) \tag{3.2}$$

Based on the optical arrangement, there are limited camera angles at a given reproduction ratio that allowed for the Scheimpflug condition to be satisfied. This is due to the fact that the Scheimpflug adaptor did not allow for lens plane tilt angles (α) greater than approximately 16°. Figure 3.7 shows the necessary lens plane tilt angle at varying reproduction ratios and camera angles.

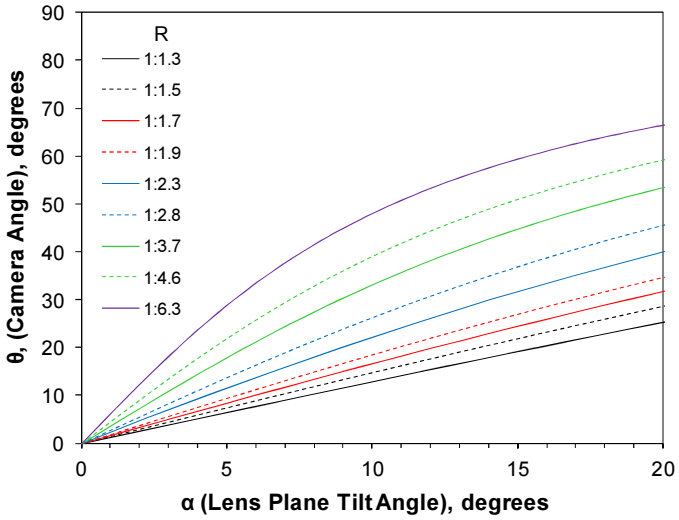

Figure 3.7: Lens plane tilt angle necessary to meet the Scheimpflug condition at varying camera angles and reproduction ratios.

Typical optical arrangements consisted of a camera angle of approximately 30 degrees with a reproduction ratio of 1:4.6 which would require a lens plane tilt angle of approximately 7.2 degrees.

3.2 SPIV Experimental Equipment

3.2.1 Optical Components

A commercial SPIV system was purchased from LaVision Inc. The system consists of a dual-cavity Nd:YAG laser, two CCD cameras and controllers, camera lenses with Scheimpflug mounts, optical filters, laser sheet forming optics, camera mounting rotational stages, and translational stages.

Laser

The laser utilized in this research was a Spectra Physics Quanta-Ray PIV 400-10 dual-cavity Nd:YAG which emitted laser pulses of wavelength λ = 532 nm and 10 nsec pulse widths. The repetition rate of the dual pulses was 10 Hz and the minimum time delay was Δt=100 ns. Typical experimental operating laser energy ranged from 90-150 mJ/pulse and typical laser pulse separation time, Δt, ranged from 400-800 nsec. The laser power is controlled by either adjusting the power of the flash lamps or adjusting the q-switch which controls the amount of time the laser light remains in the optical resonator. The laser crystal is temperature controlled and constantly supplied with a nitrogen purge of 0.2 scfm.

LaVision Cameras, Lens, and Filters

The commercial SPIV system from LaVision Inc. included two ImagerProX2M, 14 bit, CCD cameras. The main components of the camera assembly are shown in Fig. 3.8.

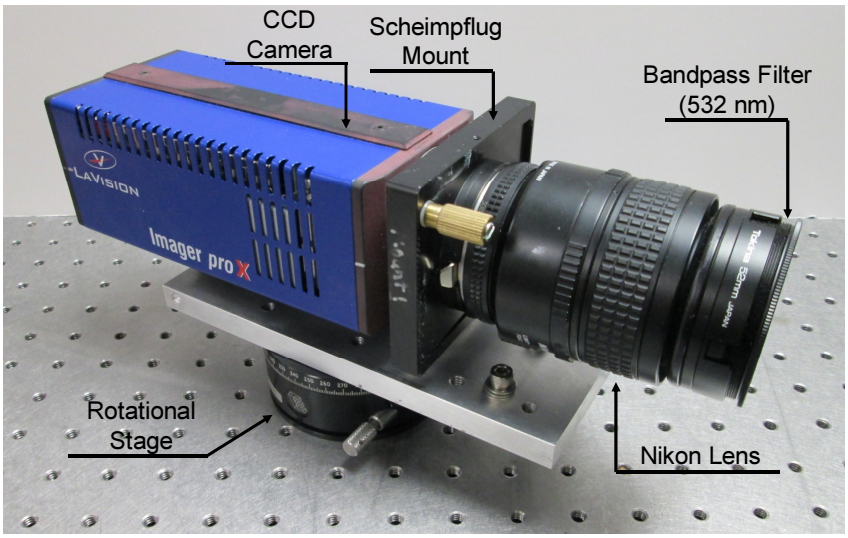

Figure 3.8: LaVision ImagerProX2M CCD Camera and Nikon Micron Nikkor 60 mm lens.

Each camera was connected to a controller which provided power and communicated with a LaVision Programmable Timing Unit (PTU-9) housed in a custom-built personal computer. The camera components and data flow diagram are presented Fig. 3.9.

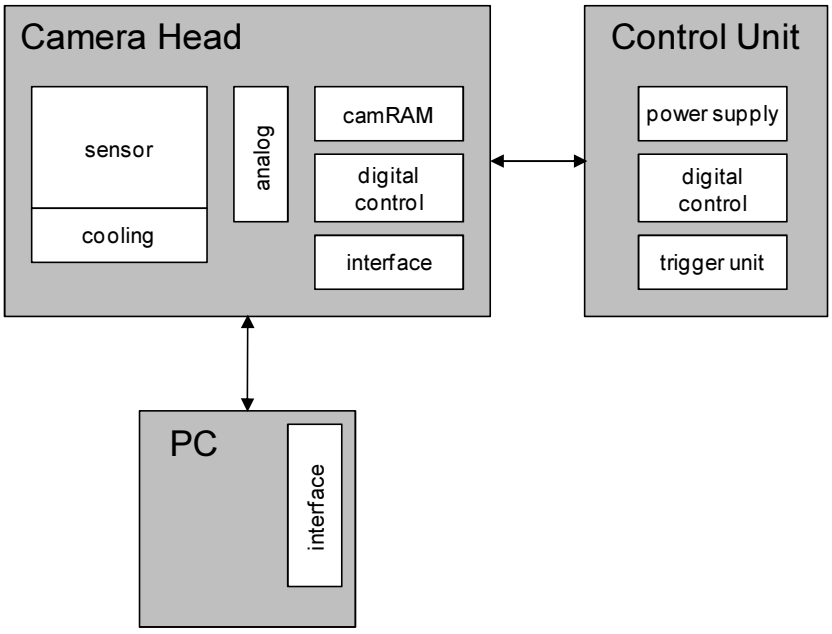

Figure 3.9: LaVision CCD camera, control unit, and PC data flow chart [46].

All electronic components were controlled with the LaVision DaVis 7.2 software package which enabled both data acquisition and analysis. The cameras have a resolution of 1600 x 1200 pixels. The pixel size is 7.4 x 7.4 μm^2 and the CCD size is 12.2 x 9 mm^2. All other technical camera information is listed in Table A.1 in Appendix A. Two sets of Nikon AF Micron-Nikkor lenses with 105 mm and 60 mm focal length attached to the camera body via a Scheimpflug mount which accepts F-type lens mounting. The Scheimpflug mount is necessary when imaging from a non-normal angle and allows the lens to tilt, altering the angle between the lens plane and image plane (the Scheimpflug criterion was discussed previously in section 3.1.3). The 60 mm Nikon lens aperture ranged from f/2.8 at the most open position to f/32 at the most closed position. Reproduction ratios from 1:1 to 1:31 can be achieved with the 60 mm lens. The depth of field at typical SPIV experimental settings (f/11 and 1:3.7) is 8 mm. Like the 60 mm lens, the 105 Nikon lens aperture also ranged from f/2.8 to f/32. The reproduction ratios ranged from 1:1 to 1:27. The depth of field for the 105 mm lens at f/11 and 1:3.2 was 9 mm. The lens was fitted with a narrow bandpass filter which only allowed the green laser light and blocked all other wavelengths of light for the purpose of maximizing the signal-to-noise ratio. The Edmund Optics (NT65-216) hard coated OD4 (optical density) transmission curves are presented in Fig. 3.10.

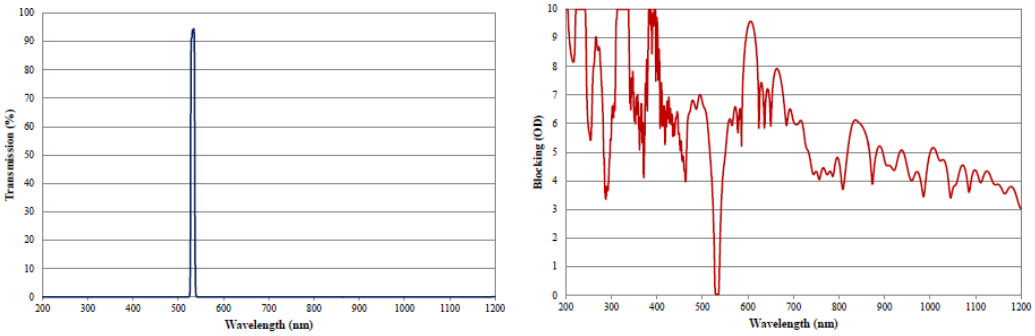

Figure 3.10: Edmund Optics hard coated narrow band pass filter: a) Wavelength transmission curve, b) Wavelength blockage curve [51].

The filters have a central wavelength of λ = 532 nm with a tolerance of ±2.00 nm. The full width-half max (fwhm) is 10.0 nm with a tolerance of ±2.00 nm. The filters achieve a minimum transmission of 85% at the desired 532 nm wavelength. Fig. 3.10(b) shows that all other wavelengths are blocked above an OD of 4. Optical density is a ratio of the intensity of light transmitted through a medium and of the incident light intensity. Fig. 3.9 shows the cameras mounted to a rotational stage which enabled precise control of the angle between the camera CCD and the object plane. All other pertinent camera information is listed in Appendix A.

Camera and laser positioning system

Both ImagerPro2XM cameras were mounted to rotational stages which allowed precise control of the camera angle relative to the measurement plane. The rotational stages were then mounted to a large rail which allowed sliding translation of each camera in the z-direction. The components of the camera and laser positioning system are highlighted in Fig. 3.11.

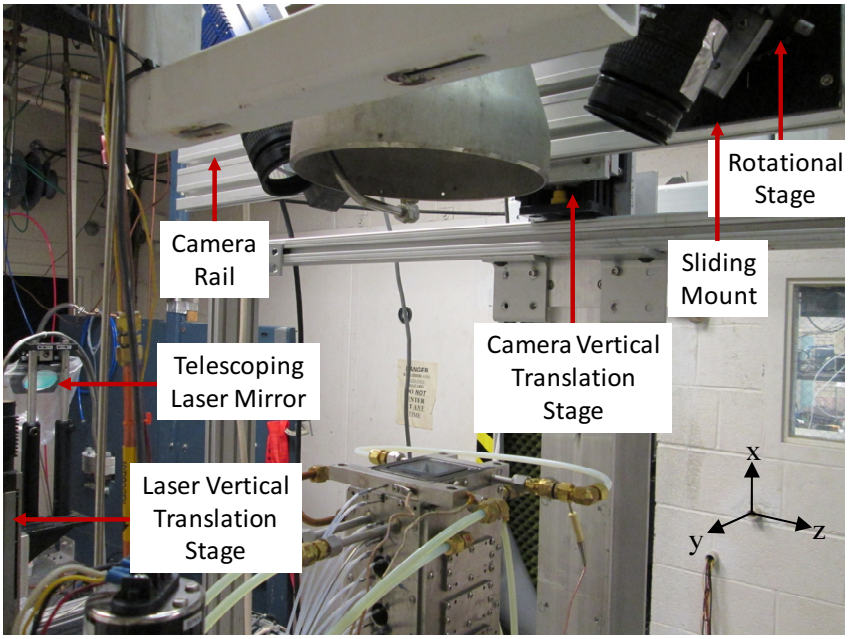

Figure 3.11: Camera and laser positioning system.

The camera rail was then mounted to a vertical Velmex motorized translational stage. The Velmex stepping motor was capable of movements equal to .005 mm/step (in the x-direction). It was advantageous to mount both cameras to a common rail in order to achieve similar optical paths. In addition, both cameras mounted to the vertical Velmex translational stage allowed the imaging system to be easily translated in the x-direction which was necessary for calibration. The calibration target was held stationary and the cameras were translated above and below the center of the laser sheet to acquire calibration images. A total of three calibration images were necessary with one location at the center of the measurement plane (laser sheet), one below, and one above, each separated by 1 mm. The Velmex vertical translation stage was also useful for moving between different measurement planes, for example between x/H=6 and x/H=12. The telescoping laser sheet mirror was mounted to a Klinger stepping motor to allow

translation of the laser sheet in the x-direction. The Klinger stepping motor allowed movement of the laser sheet in increments of .001 mm.

Calibration targets

Two calibraton targets were purchased from Edmund Optics. Both targets were constructed of a photographic film grid. The first target (EO 62-212) was a 50 x 50 mm square grid with 0.25 mm diameter dots at 1 mm spacing. The full square length of the grid was utlized since there were no size restrictions at the combustor exit plane and the extender exit plane. The second target (EO 57-984) was a 50 x 50 mm square grid with 0.5 mm diameter dots at 1 mm spacing. The grid was cut and attached to an aluminum plate which allowed the target to fit inside the combustor test section. The final dimension of the grid was 30 columns and 21 rows. Both targets are shown in Fig. 3.12.

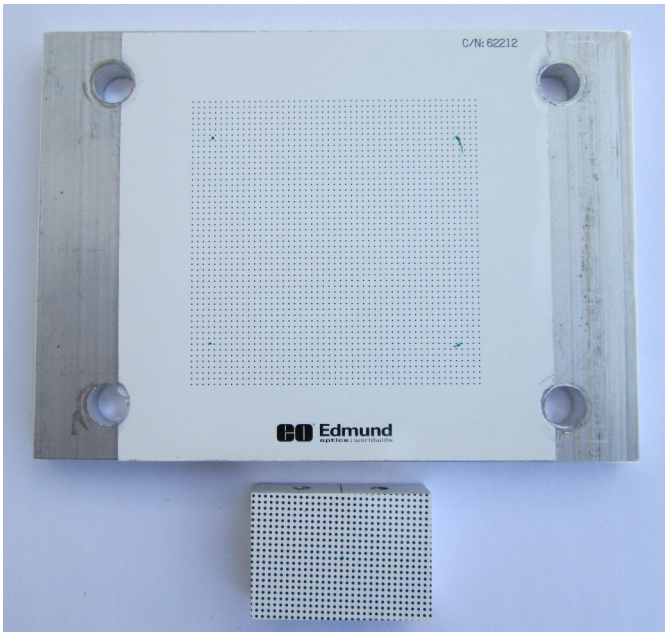

Figure 3.12: Calibration target 1 and target 2

Both targets received a certification of accuracy from Max Levy Autograph, Inc. The film grid is accurate to within ± 0.035 mm corner to corner and the dot spacing is accurate to ± 0.005 mm. The calibration process and the procedure for dewarping the imaged are depicted in Fig. 3.13.

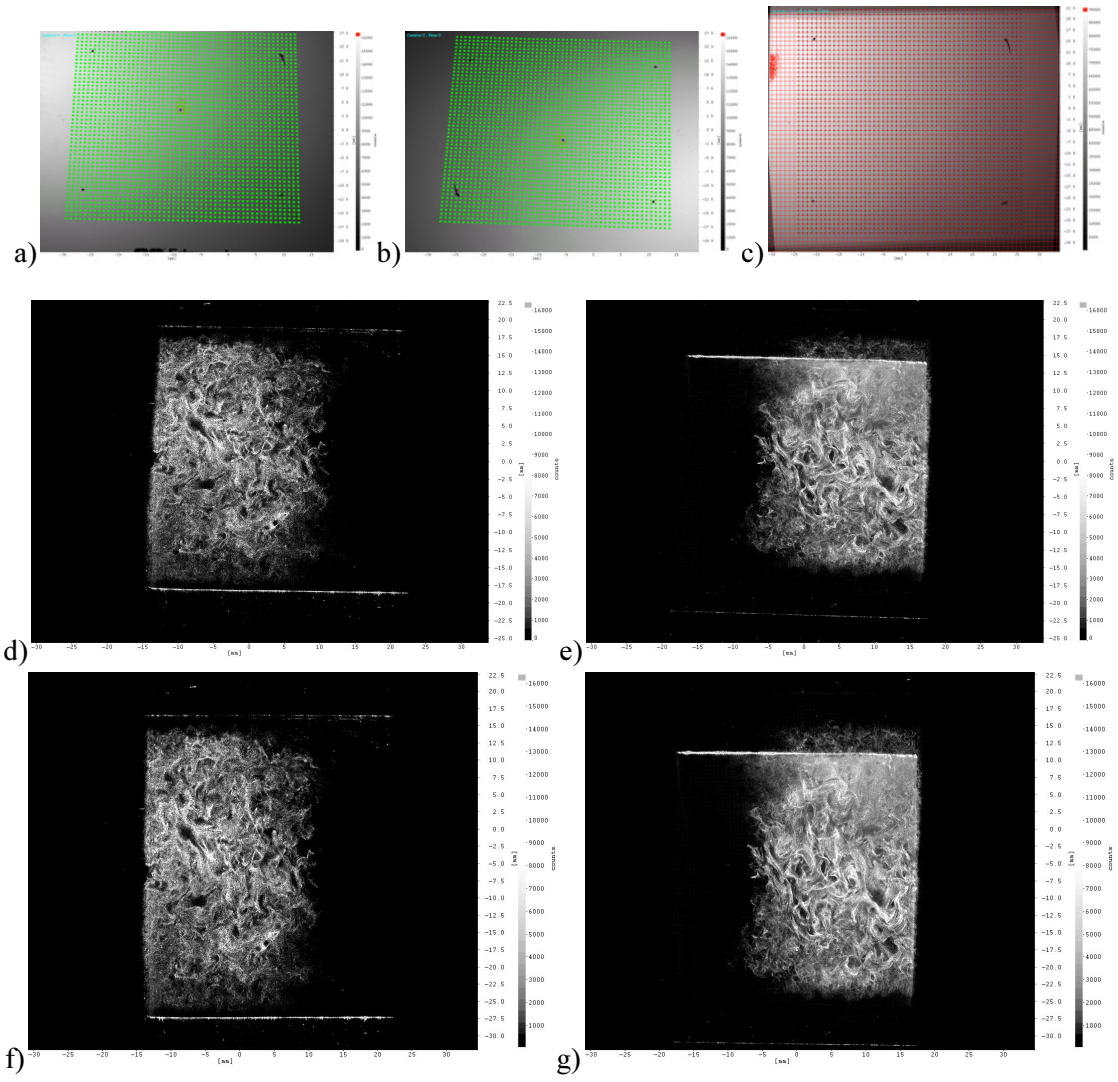

Figure 3.13: Calibration process and image dewarping procedure: a) Camera 1 dot pattern image, b) Camera 2 dot pattern image, c) Both cameras dewarped dot pattern image, d) Camera 1 particle image, e) Camera 2 particle image, f) Camera 1 dewarped particle image, g) Camera 2 dewarped particle image.

Fig. 3.13(a)/(b) show the distorted view of the calibration target from camera 1 and 2. Fig. 3.13(c) shows the dewarped (undistorted) view from both cameras. Evidence of non-normal viewing angles can be seen in Fig. 3.13(a)/(b) with a trapezoid shaped grid that

has been corrected and lies on a rectangular grid in Fig. 3.13(c). Fig. 3.13(d)/(e) show raw particle images with a distorted view from camera 1 and camera 2 and the corresponding corrected particle images in Fig. 3.13(f)/(g). Lines that were angled in Fig. 3.13(d)/(e) now appear parallel to the left/right boundary of the image in Fig. 3.13(f)/(g).

Laser delivery and sheet-forming optics

The laser is converted to a sheet with constant width of approximately 47 mm and a thickness of 2.5 mm. The width of the sheet can be adjusted with the use of a baffle mounted to the window frame to account for different duct dimensions at different measurement planes. The laser sheet is achieved through the use of four uncoated quartz lenses. The primary components of the optical train are depicted in Fig. 3.14.

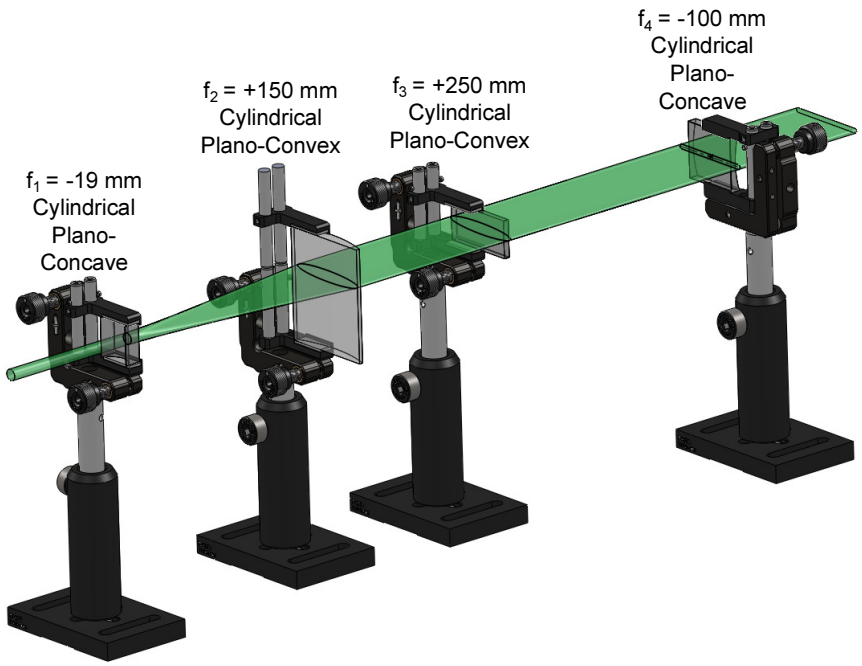

Figure 3.14: Laser sheet-forming optics.

The beam begins as a 10 mm circular spot and an aperture is utilized to decrease the spot size to 6 mm. The beam is first spread by a -19 mm focal length cylindrical plano-

concave lens. The second lens, a 150 mm focal length cylindrical plano-convex lens, was positioned 131 mm away in order to create a constant width of 47 mm. The third lens, a 250 mm focal length cylindrical plano-convex lens, focused the beam thickness down to 2.5 mm. The final lens, a -100 mm focal length cylindrical plano-concave lens was positioned 150 mm from the third lens in order to maintain a constant sheet thickness.

The laser is located in a room adjacent to the UVaSCF and therefore the beam must be delivered through a small tube mounted in the adjoining wall. The laser delivery path is outlined in Fig. 3.15.

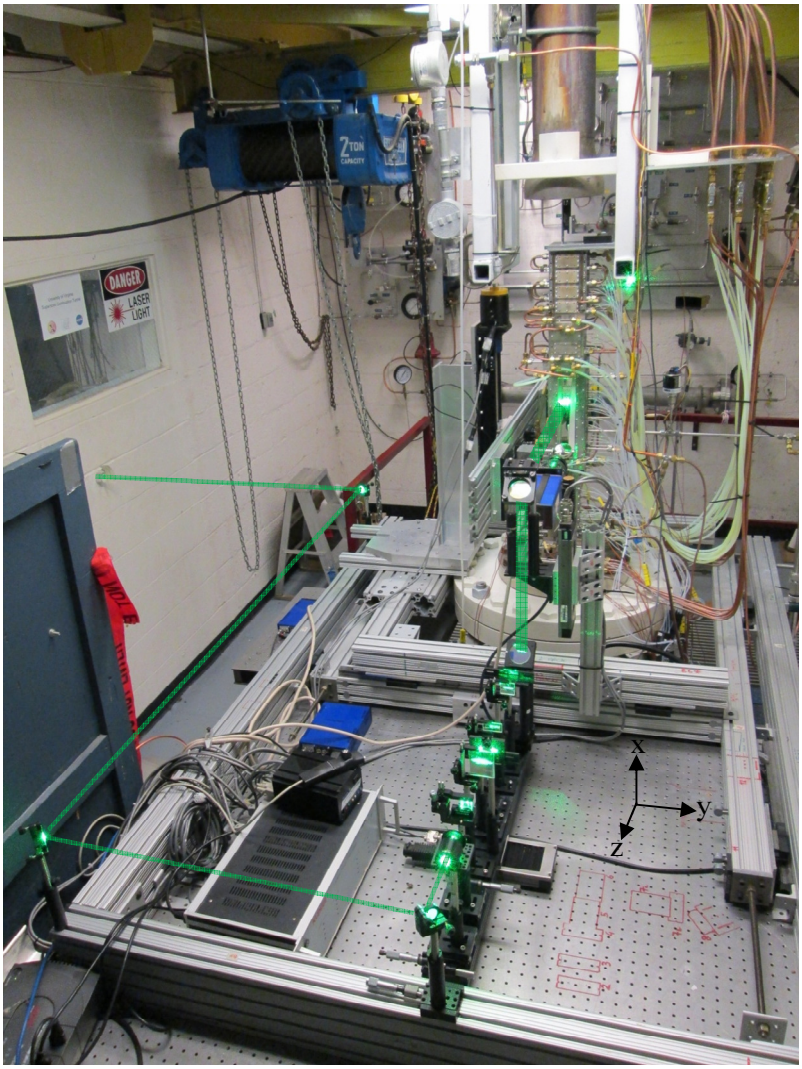

Figure 3.15: Laser sheet delivery path

Several laser mirrors redirect the beam to the optical train which is mounted on a Klinger translational stage which allows for movement in the y-direction. After the laser sheet was formed, a periscope was constructed with two 45° mounted mirrors which directed the beam vertical and then horizontal, delivering the beam to the measurement volume perpendicular to the test section and flow direction. The last mirror was mounted to a Klinger translational stage that enabled precise movement in the vertical x-direction allowing for beam delivery at any of the four measurement planes.

3.2.2 Particles and Seeding Method

The most common tracer particles used for PIV applied to high-speed, combusting flows are metal oxide and glass oxide powders such as aluminum oxide (Al_2O_3), titanium dioxide (TiO_2), and silicon dioxide (SiO_2). Silicon dioxide has been chosen for the current experiments due to the spherical shape and availability at low cost and a wide range of diameters. The particles were purchased from the Fiber Optic Center Inc. and an SEM photograph of the silica spheres is shown in Fig. 3.16.

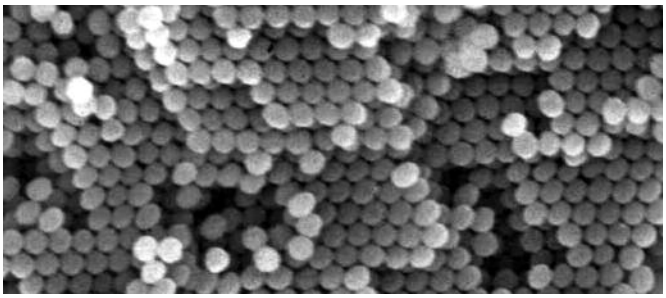

Figure 3.16: Silica particles scanning electron microscope (SEM) photograph [52].

The spherical shape of the particle was advantageous due to both superior flow tracking capability as compared to non-spherical particles, and the minimization of particle agglomeration. The properties of the silica particles are listed in Table 3.1.

Table 3.1: Tracer particle properties.

Property		Unit
Material	SiO_2 (Silica)	
Shape	Spherical	
Size	0.25	μm
Size distribution	Standard deviation <10%	
Density	1800	kg/m^3
Refractive index	~1.42	
Melting point	1840	°C
Stokes number	0.08	

Another advantage of the silica particles was the high melting point, which was necessary for the high-temperature, reacting flowfield. A particle diameter of 0.25 μm was chosen based on the trade-off with particle diameter in which large particles have better light scattering characteristics and small particles have better flow tracking capability. Therefore a balance must be reached where adequate signal-to-noise ratio can be achieved while still incurring minimal particle slip velocity. Depending on the size of particles, different light scattering occurs. For example, in the case of molecules, which typically have a diameter much less than the wavelength of light, Raleigh scattering occurs. PIV particles, which have diameters much larger than a molecule, produce Mie scattering which is non-linear with particle diameter. Therefore, a large enough particle must be chosen in order to maximize the signal-to-noise ratio of the PIV images. The scattering cross-section, C_s, is a ratio of the total scattered power to the laser intensity. The scattering cross-section is highly non-linear with particle diameter. For example, the scattering cross-section of a 1 μm diameter particle is approximately proportional to

$(d_p/\lambda)^4$ and a 10 μm diameter particle is approximately proportional to $(d_p/\lambda)^2$, where d_p is particle diameter and λ is the laser wavelength [53]. For reference, a 1 μm diameter with refractive index 1.6 has a scattering cross-section of approximately 10^{-12} m^2, whereas the Rayleigh scattered from a molecule has a scattering cross-section of approximately 10^{-33} m^2.

According to Melling [53], particle diameters less than 1 μm accurately track turbulent fluctuations on the order of 10-25 kHz. The Stokes number is a ratio of particle response time to flow time scales which quantifies the ability of a particle to accurately track the flow. Equation 3.2 defines the particle Stokes number and Equation 3.3 gives the expression formulated by Erbland [54] for calculation of particle response time, τ_p.

$$St = \tau_p \frac{U}{d} \tag{3.2}$$

$$\tau_p = \frac{\rho_p {d_p}^2}{18\mu_g}\left[1 + Kn\left(2.492 + 0.84e^{\frac{-0.435}{Kn}}\right)\right] \tag{3.3}$$

The particle response time is a function of the particle density ρ_p, the particle diameter d_p, the fluid viscosity μ_g, and the Knudsen number Kn, which is a ratio of the mean free path and particle diameter. The characteristic flow velocity was 1000 m/s and the domain length scale was the duct height equal to 25.4 mm. The particle response time and Stokes number for the SiO_2 particles is 1.9 μs and 0.075 respectively. The particle Stokes number based on the average cross-plane velocity (15 m/s) and the turbulent mixing length scale (5mm) is .005. Therefore, the particles are capable of accurately tracking both the large velocity in the axial direction and the turbulent vortex structures in the cross-plane. A computational analysis of a particle laden compressible shear layer, by Samimy and Lele [55], reports the Stokes number limit for accurate flow tracking to be

less than 0.25. The authors report an error of about 2% for a Stokes number of 0.2. The same criterion of St<0.25 was experimentally verified by Clemens and Mungal [56] and Urban and Mungal [57] in which the particle relaxation time was measured across a Mach 1.8 oblique shock for various particle diameters. Based on those criteria, it can be concluded with confidence that the seed particles selected for these experiments accurately track the flow despite large velocity gradients, and errors due to slip velocity are much less than 2%.

In order to estimate the particle concentration, a peak finding algorithm was utilized to calculate the number of intensity peaks across a raw particle image. It is assumed that an intensity peak that is distinguishable with reference to its neighbors corresponds to the occurrence of a particle. Fig. 3.17a shows an isolated rectangular region of a typical raw particle image with units of pixels on the axes.

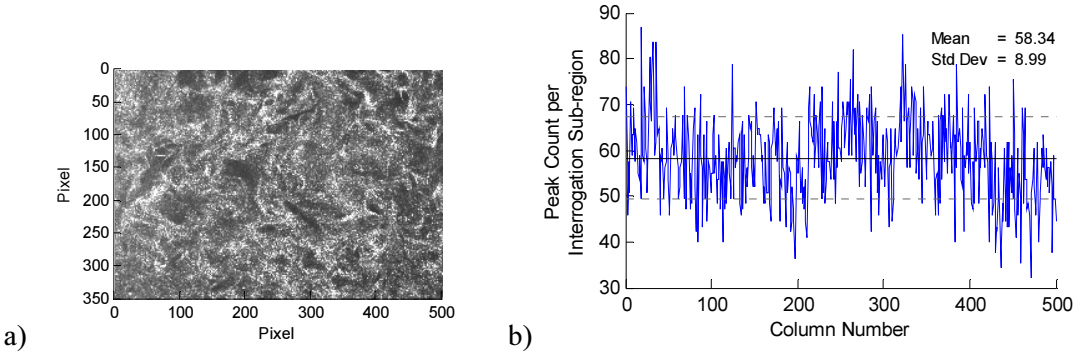

Figure 3.17: Particle peak finding routine: a) Rectangular raw particle image, b) Peak count per interrogation sub-region versus column number.

A column vector of intensity was the input to the peak finding algorithm with a minimum peak height of 400 counts and a peak-to-neighbor threshold of 40 which is twice the standard deviation of the background intensity. The output of the algorithm is the number of peaks across a vertical column and this was repeated 500 times across the raw particle

image. The results of this analysis are presented in Fig. 3.17b which shows the number of peaks (or particles) per interrogation region length at every column. Since the peak finding algorithm only works for vectors, this 1-D particle concentration was simply squared to estimate the particles per interrogation region (32x32 pixels). The results indicate an average number of particles per interrogation sub-region of 58 with a standard deviation of 9. It is of note to mention that this number is significantly higher than the minimum number of particle pairs per interrogation sub-region suggested by Keane and Adrian [45].

It is possible to seed both the freestream air upstream of the facility nozzle and the fuel stream. Both the fuel seeder and freestream seeder are fluidized bed aerosol generators which operate by flowing gas through a bed of dry particles. The fuel seeder, shown in Fig. 3.18, features three primary flowpaths.

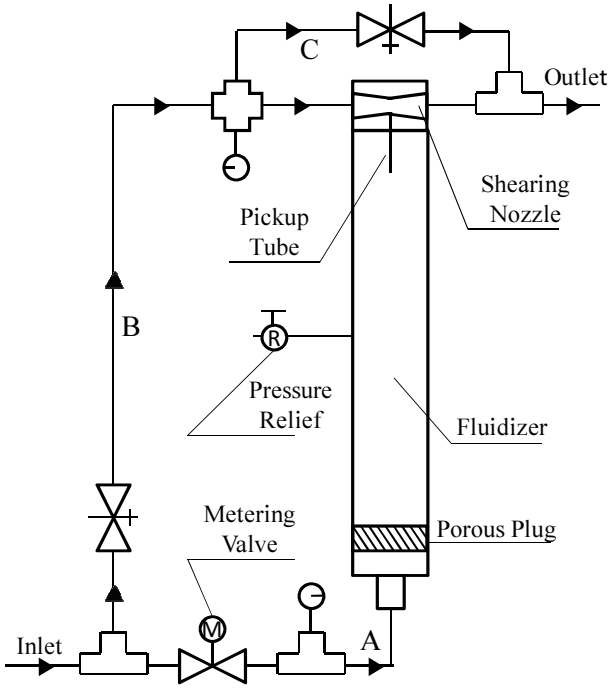

Figure 3.18: Fluidized bed aerosol particle generator (fuel seeder) [58].

The particles sit on the porous plug in which hydrogen gas flows through path A, causing the particles to suspend and travel vertically in the fluidizer. The particle-laden flow is then delivered through the fuel injector. Key features of the fuel seeder are the shearing nozzle and pickup tube. Flow along path B enters the shearing nozzle and accelerates the hydrogen to Mach 3. The high speed flow causes a pressure gradient which serves to pull the particles up into the pickup tube. At this point the high speed flow impacts the particles with a shearing force causing breakup of particle agglomeration. Path C is a hydrogen by-pass loop which was utilized at high fuel mass flow rates. The needle valve is adjusted such that the proper fuel mass flow can be achieved. This is verified and measured at the outlet with a mass flow sensor. The flow rate through the fluidizer is controlled remotely via a metering valve and this allows for adjustment of seeding density during an experiment. The freestream seeder followed the same basic design but no shearing nozzle is utilized due to lower injection pressure. The freestream particles are introduced directly upstream of the facility nozzle to ensure complete coverage of the duct. For x/H=6 and x/H=12 only the fuel seeder was operated and thus measurements were conducted in the combusting plume. At x/H=29 and x/H=82 both seeders were operated to ensure full coverage of the duct and avoid biasing effects. Pressure is monitored on both seeders in order to deliver a constant seed density to both streams during all three seeding cases and seed density is assessed qualitatively. The seeder design and operation is documented by Howison and Goyne [58]. These investigators also verified quantitatively the seeder produced particle size and shape and showed that the apparatus is capable of delivering seed with predominantly the characteristics of the

primary particles [58]. According to Howison, the average particle size delivered by the seeding apparatus was 0.27 μm diameter with a standard deviation of .07 μm.

Chapter 4

SPIV Experimental Configurations

SPIV experiments were conducted at a total of 4 measurement planes downstream of fuel injection, shown in Fig. 4.1, with reference to the Config. C tunnel hardware.

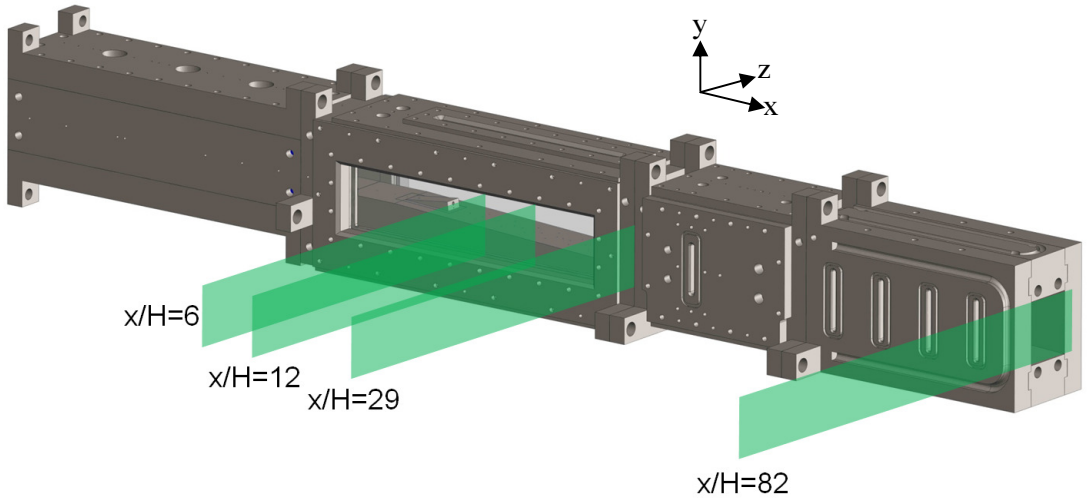

Figure 4.1: Isometric view of MSCT with SPIV measurement plane locations specified.

To study the two different modes of combustion (ramjet mode and scramjet mode) experiments were conducted at x/H=6, x/H=12, and x/H=82 (extender exit). The measurement planes in the combustor section were determined by the NCHCCP and the exit plane enabled combustion efficiency measurements when combined with TDLAT. The scramjet mode of operation is simulated with an equivalence ratio, φ=0.18, and the ramjet mode of operation is simulated with an equivalence ration, φ=0.49. To study the effect of velocity bias due to seeding, an experiment was performed at x/H=29 at the exit plane of the combustor. The current chapter describes the SPIV optical setup at each plane and documents the key experimental parameters.

4.1 Measurement Plane Location x/H=6

The most upstream measurement location at x/H=6 is nearest to the ramp fuel injector. This measurement plane required the most extreme camera viewing angle, θ, due to the fact that the plane is located nearly in the middle of the side window. Therefore, no significant advantage is achieved by viewing the measurement plane with the cameras from below or above. Fig. 4.2 shows the SPIV experimental configuration for x/H=6.

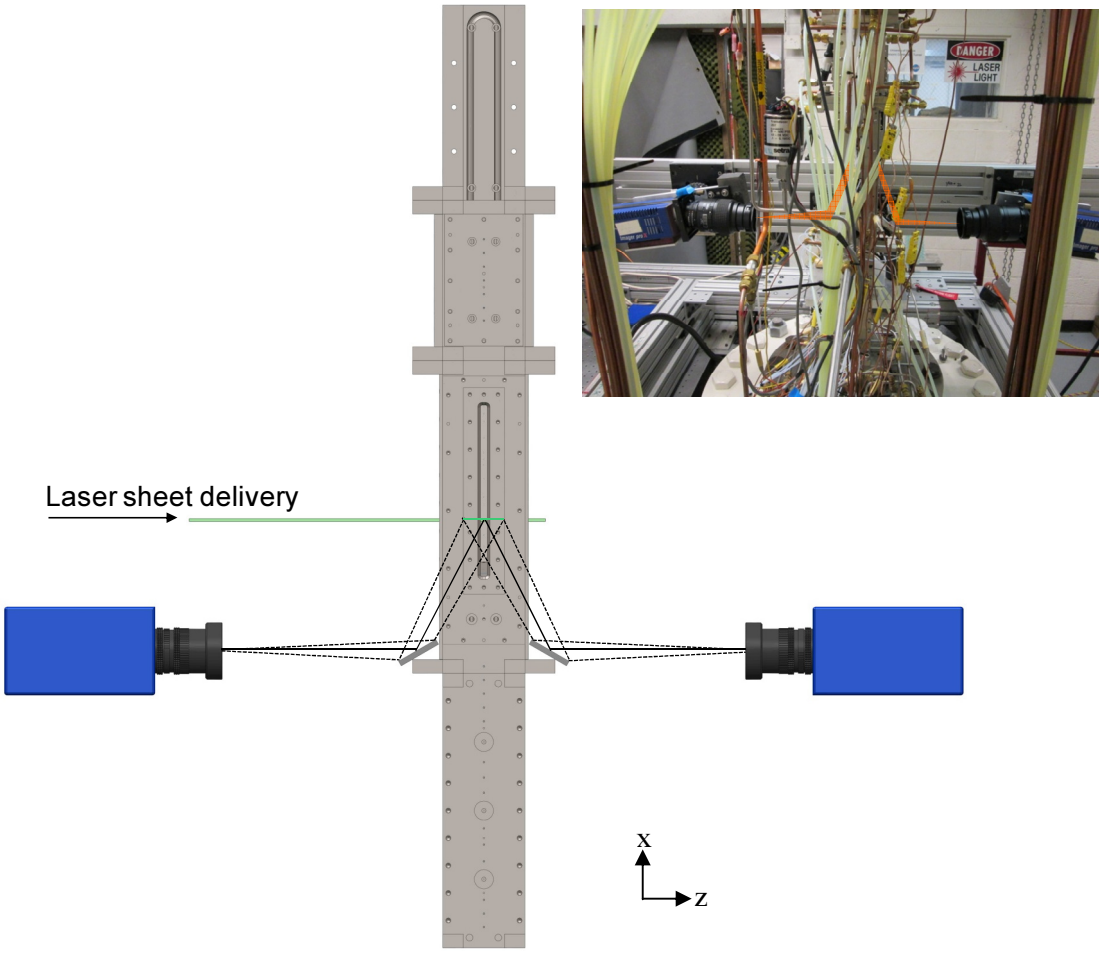

Figure 4.2: SPIV optical configuration at x/H=6.

Due to the physical dimensions of the flowpath hardware, cameras, and lenses, the cameras could not be positioned close enough to the flowpath hardware at the necessary camera viewing angle without interference. Therefore, two 2 in. diameter first surface

mirrors were utilized and positioned at the most upstream location possible without interference with the combustor tabs or cooling tubes. The mirrors are attached to a tip-tilt optical mount which allows precise control of the camera viewing angle, θ, defined as the angle between the central light ray trace and the x-axis. The mirrors serve to redirect the optical path of the cameras and allow imaging at x/H=6. Fig. 4.1 shows that the light sheet was delivered in the z-direction and the left camera collects back-scattered intensity from the particles and the right camera collects forward-scattered intensity. Backscatter has less intensity than forward scatter which is a drawback of this camera configuration. To adjust for this disparity, the aperture of the camera lens (f#) viewing in backscatter is opened one step up allowing more light to reach the CCD. This effectively balances the signal-to-noise ratio between the two cameras while maintaining a large enough depth of field to cover the laser sheet thickness. The key experimental parameters are given in Table. 4.1.

Table 4.1: Experimental equipment and parameters at x/H=6.

Experimental Equipment			
SPIV System	LaVision Inc.	**PIV Cameras**	Imager ProX2M
Laser	Quanta Ray PIV 400-10	**Camera CCD Dimensions**	8.88 x 11.84 mm 1200 x 1600 pix
Seeder	Fuel seeder	**CCD Pixels Physical Size, ℓ_{pix}**	7.4 x 7.4 μm
Calibration Target (Ø dots, spacing)	Target A (Ø 0.5 mm, 1 mm)	**Camera Lenses**	105 mm, AF Micro-Nikkor
SPIV Experimental Parameters			
Seed Particles	Silicon Dioxide (SiO_2)	**Dist. Object to CCD ℓ**	383 mm
Particle Diameter d_p	0.25 μm	**Reproduction Ratio**	1/2.9
Pulse Separation Time Δt	400-700 ns	**Field-of-View z x y (undistorted)**	34.4 x 25.8 mm
Laser Sheet Thickness	2.5 mm	**Camera Angle θ**	38°
Laser Sheet Width	29 mm	**Image Plane Angle α**	15°
Laser Energy	80-100 mJ/pulse	**Camera Lens Aperture $f^{\#}$**	f/11, f/8
Laser Sheet Delivery	Through side-windows	**Sub-region Size, ℓ_I**	32x32 pixels
Camera Viewing Arrangement	Forward scatter/ back scatter	**Sub-region Overlap**	50%

Note that a laser pulse time delay, Δt, of 400 ns was delivered during the φ=0.49 fuel condition due to higher expected axial velocities from the fuel jet. The field-of-view is set to be slightly larger than the laser sheet area to ensure overlap between the two cameras and compensate for the distortion of the image as a result of an oblique viewing angle.

4.2 Measurement Plane Location x/H=12

The measurement plane x/H=12 is located in the combustor section but is further downstream of fuel injection. It remains advantageous to again view from below the measurement plane with the assistance of mirrors to redirect the optical path. The SPIV experimental configuration is shown in Fig. 4.3.

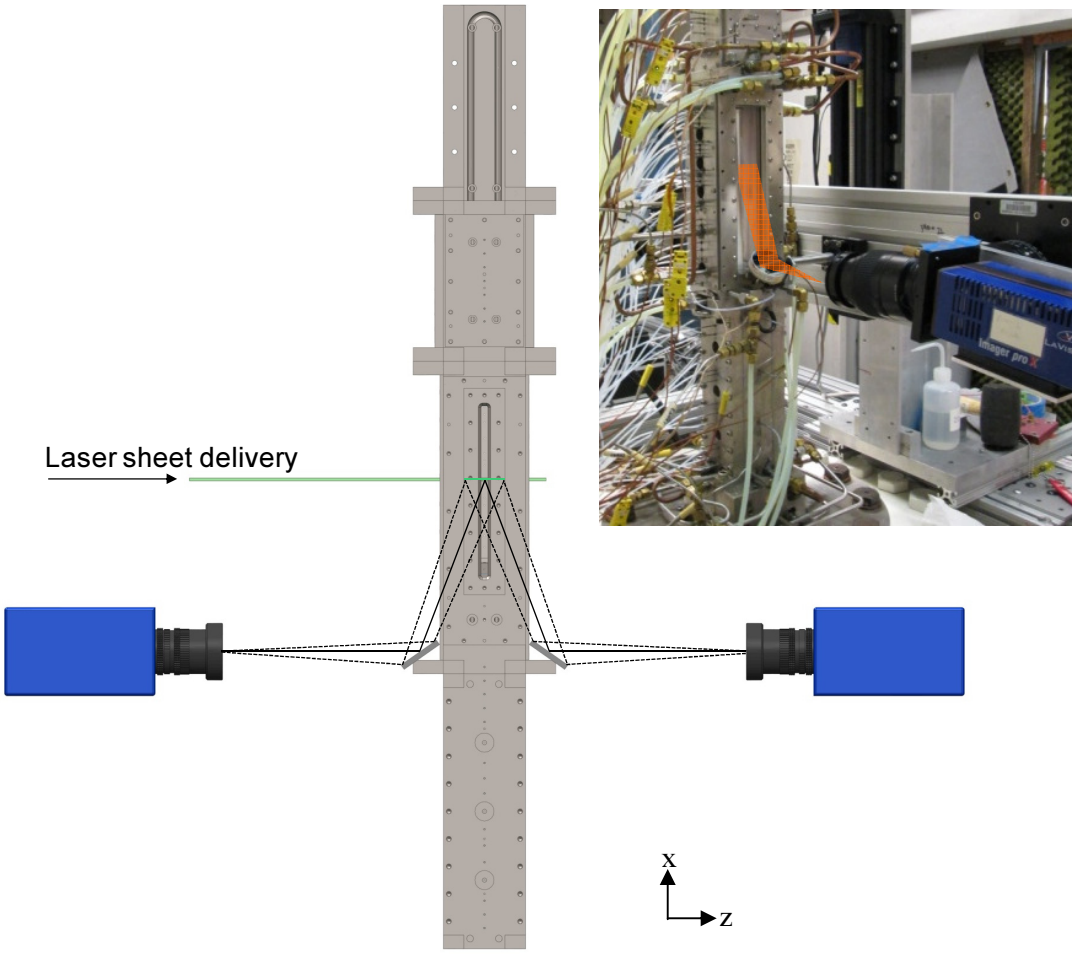

Figure 4.3: SPIV optical configuration at x/H=12.

Since the measurement plane is further downstream, a smaller camera angle, θ, is necessary. This is advantageous because it minimizes the image distortion and Scheimpflug angle. Due to the divergence of the combustor-side of the flowpath, a

slightly larger field-of-view is necessary to capture the duct area. The primary experimental parameters for x/H=12 are listed in Table 4.2.

Table 4.2: Experimental equipment and parameters at x/H=12.

Experimental Equipment			
SPIV System	LaVision Inc. Commercial System	**PIV Cameras**	Imager ProX2M
Laser	Quanta Ray PIV 400-10	**Camera CCD Dimensions**	8.88 x 11.84 mm 1200 x 1600 pix
Seeder	Fuel seeder	**CCD Pixels Physical Size, ℓ_{pix}**	7.4 x 7.4 μm
Calibration Target (Ø dots, spacing)	Target A (Ø 0.5 mm, 1 mm)	**Camera Lenses**	105 mm, AF Micro-Nikkor
SPIV Experimental Parameters			
Seed Particles	Silicon Dioxide (SiO_2)	**Dist. Object to CCD ℓ**	379 mm
Particle Diameter d_p	0.25 μm	**Reproduction Ratio**	1/2.8
Pulse Separation Time Δt	500-700 ns	**Field-of-View z x y (undistorted)**	33.7 x 25.2 mm
Laser Sheet Thickness	2.5 mm	**Camera Angle θ**	34°
Laser Sheet Width	30 mm	**Image Plane Angle α**	13.5°
Laser Energy	80-100 mJ/pulse	**Camera Lens Aperture $f^{\#}$**	f/11, f/8
Laser Sheet Delivery	Through side-windows	**Sub-region Size, ℓ_I**	32x32 pixels
Camera Viewing Arrangement	Forward scatter/ back scatter	**Sub-region Overlap**	50%

The laser sheet is again delivered in the z-direction and the cameras view in forward and back scatter orientations. A slightly larger laser sheet width is necessary due to the divergence of the flowpath in the y-direction. Again, the 105 mm Nikon lenses are utilized and a similar reproduction ratio and distance of the object to CDD is achieved as in x/H=6.

4.3 Measurement Plane Location x/H=29 (Combustor Exit)

The measurement plane at x/H=29 is located at the exit of the combustor section. This is the closest plane downstream of fuel injection where measurements can be taken of the external DMSJ flow without the hindrance of windows. The goal of this measurement plane was to assess and quantify the errors associated with the method of seeding the fuel stream only. This was accomplished by measuring the velocity field during three seeding scenarios 1) fuel stream seeded, 2) fuel stream and freestream seeded, and 3) freestream seeded. The combustor exit plane was necessary to enable seeding of the freestream which is only possible due to the lack of windows. For this measurement plane location the constant area section and extender were removed. Details of this experiment and further justification of the plane selection will follow in Chapter 5. The removal of the constant area section and extender section enabled a camera configuration viewing from above without the need for mirrors. The experimental configuration for x/H=29 is shown in Fig. 4.4.

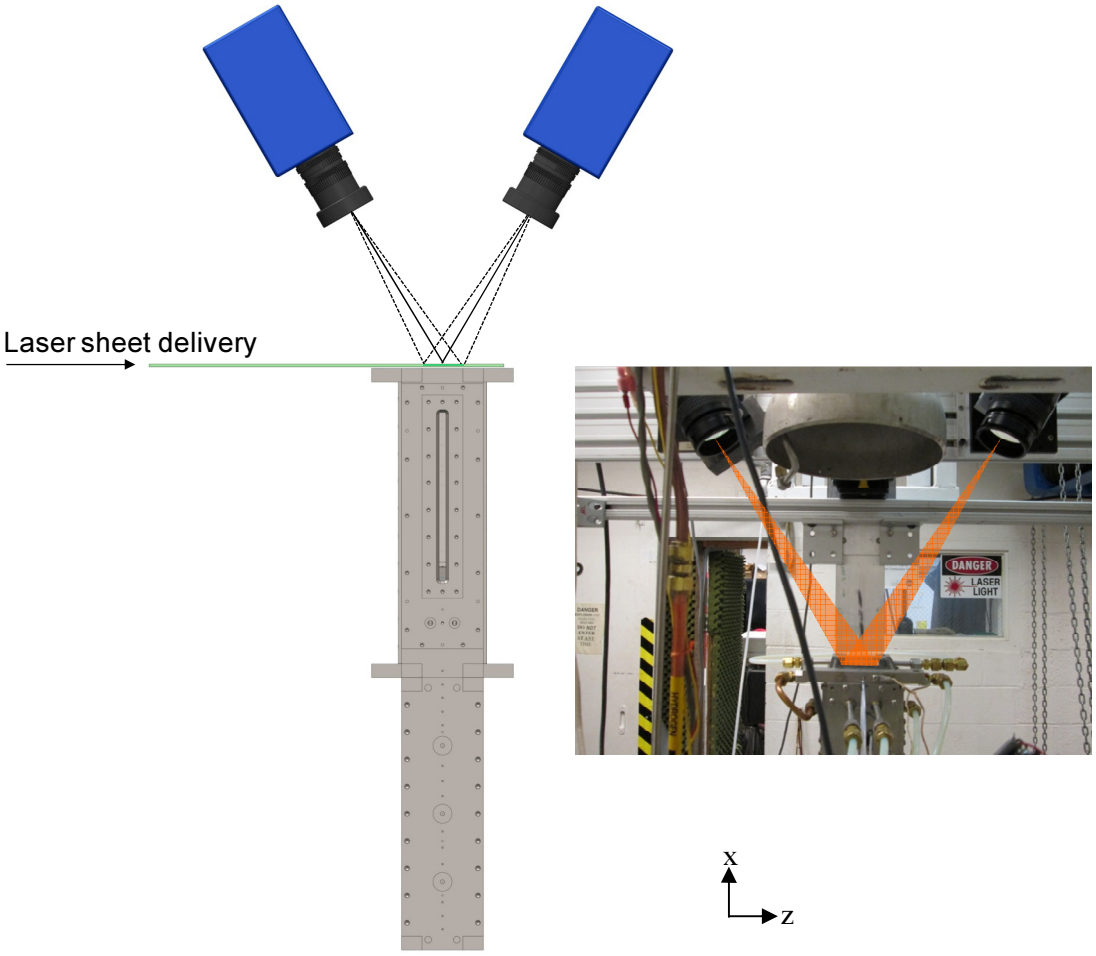

Figure 4.4: SPIV optical configuration at x/H=29.

This camera configuration is preferred over the camera configuration at x/H=6 and x/H=12 because the complication of mirrors and additional alignment is avoided. The cameras are positioned in the x-z plane and view from above. To maintain consistency with other planes and avoid an excessively long and complex laser beam path, the laser sheet is delivered in the z-direction. It can be seen that the camera lenses protrude past the physical extent of the flowpath hardware which was not possible at x/H=6 or 12. The camera placement is limited by the extent of the high-temperature, burning flame which exits the combustor and enters an exhaust duct. Therefore, the camera angle, θ=38°, is necessary for viewing this measurement plane. The 60 mm Nikon lenses were utilized at

this plane due to the necessity of a larger reproduction ratio. For example, at the given reproduction ratio the 105 mm lenses would have required a focused distance of approximately 0.7 m, which was not feasible due to physical restrictions of the facility. All other experimental parameters for the x/H=29 plane are listed in Table 4.3.

Table 4.3: Experimental equipment and parameters at x/H=29.

Experimental Equipment			
SPIV System	LaVision Inc. Commercial System	**PIV Cameras**	Imager ProX2M
Laser	Quanta Ray PIV 400-10	**Camera CCD Dimensions**	8.88 x 11.84 mm 1200 x 1600 pix
Seeder	Fuel and freestream seeder	**CCD Pixels Physical Size, ℓ_{pix}**	7.4 x 7.4 μm
Calibration Target (Ø dots, spacing)	Target A (Ø 0.25 mm, 1 mm)	**Camera Lenses**	60 mm, AF Micro-Nikkor
SPIV Experimental Parameters			
Seed Particles	Silicon Dioxide (SiO_2)	**Dist. Object to CCD ℓ**	428 mm
Particle Diameter d_p	0.25 μm	**Reproduction Ratio**	1/5.5
Pulse Separation Time Δt	800 ns	**Field-of-View z x y (undistorted)**	64.8 x 48.6 mm
Laser Sheet Thickness	2.5 mm	**Camera Angle θ**	38°
Laser Sheet Width	38 mm	**Image Plane Angle α**	8°
Laser Energy	120 mJ/pulse	**Camera Lens Aperture $f^{\#}$**	f/11, f/8
Laser Sheet Delivery	No windows	**Sub-region Size, ℓ_I**	32x32 pixels
Camera Viewing Arrangement	Forward scatter/ back Scatter	**Sub-region Overlap**	50%

The expected axial velocities at this plane were slightly less than at x/H=12 and a Δt=800 ns was used. Higher laser energy was permitted at this measurement plane due to the absence of windows which typically causes high intensity laser reflections. The

measurement plane area of 1.44x1.5 facilitated a large reproduction ratio and the resulting Scheimpflug angle of only 8° despite a camera angle of 38°.

4.4 Measurement Plane Location x/H=82 (Extender Exit)

The measurement plane at x/H=82 is located at the exit of the extender section in the DMSJ flowpath. This measurement location, along with x/H=6 and 12 served the goal of measuring the velocity field of the DMSJ during both modes of combustion. The extender section exit plane is particularly interesting because when SPIV velocity measurements are combined with spatially resolved water mole fraction determined by Tunable Diode Laser Absorption Tomography (TDLAT) the combustion efficiency can be calculated [86]. The camera configuration at x/H=82 is illustrated in Fig. 4.5.

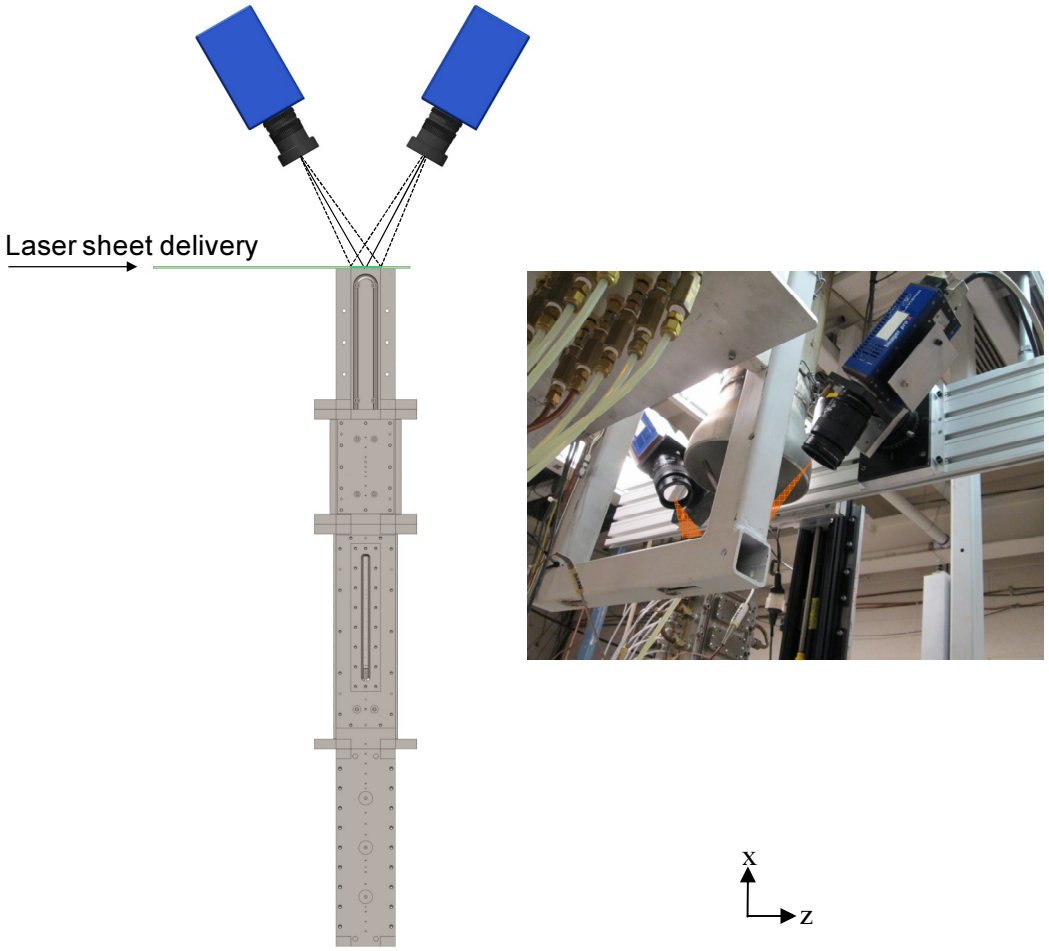

Figure 4.5: SPIV optical configuration at x/H=82.

The constant area section and extender section were both installed to form the full Configuration C flowpath as for the measurements plane locations x/H=6 and 12. As was the case for the measurement plane at the exit of the combustor (x/H=29), the cameras are positioned to view from above with no need for mirrors. The measurement plane and resulting camera configuration at the extender exit is essentially the same as that at the exit of the combustor except for a larger measurement area. The experimental parameters for the measurement plane location at x/H=82 are listed in Table 4.4.

Table 4.4: Experimental equipment and parameters at x/H=82.

Experimental Equipment			
SPIV System	LaVision Inc. Commercial System	**PIV Cameras**	Imager ProX2M
Laser	Quanta Ray PIV 400-10	**Camera CCD Dimensions**	8.88 x 11.84 mm 1200 x 1600 pix
Seeder	Fuel and freestream seeder	**CCD Pixels Physical Size, ℓ_{pix}**	7.4 x 7.4 μm
Calibration Target (Ø dots, spacing)	Target A (Ø 0.25 mm, 1 mm)	**Camera Lenses**	60 mm, AF Micro-Nikkor
SPIV Experimental Parameters			
Seed Particles	Silicon Dioxide (SiO_2)	**Dist. Object to CCD ℓ**	336 mm
Particle Diameter d_p	0.25 μm	**Reproduction Ratio**	1/4.5
Pulse Separation Time Δt	800 ns	**Field-of-View z x y (undistorted)**	53.3 x 40.0 mm
Laser Sheet Thickness	2.5 mm	**Camera Angle θ**	41°
Laser Sheet Width	48 mm	**Image Plane Angle α**	10.9°
Laser Energy	120 mJ/pulse	**Camera Lens Aperture $f^{\#}$**	f/11, f/8
Laser Sheet Delivery	No Windows	**Sub-region Size, ℓ_I**	32x32 pixels
Camera Viewing Arrangement	Forward Scatter/ Back Scatter	**Sub-region Overlap**	50%

Again, the 60 mm Nikon lenses were used due to the necessity to position the cameras closer to the measurement plane while achieving the proper reproduction ratio. Due to the absence of windows at the exit plane, seeding of both the fuel stream and freestream with silica particles was implemented. Therefore, negligible velocity bias errors due to seeding were incorporated.

Chapter 5

Seeding Bias and Experimental Uncertainty

Chapter 5 focuses on measurements conducted at the exit plane of the combustor (x/H=29) for the purpose of quantifying the velocity bias errors associated with seeding the ramp fuel injector only. Uniform seeding is important for Particle Image Velocimetry (PIV) due to the fact that all velocity data is derived from the movement of particles as fluid tracers. However, in some wind tunnel applications uniform seeding is not possible due to severe fouling of windows. One such application is in the University of Virginia Supersonic Combustion Facility (UVaSCF). Past PIV measurements in this facility have potential velocity bias errors due to non-uniform seeding, since particles were only introduced in the fuel stream and not the freestream of a dual-mode scramjet (DMSJ) combustor. The present study seeks to experimentally quantify the velocity bias errors associated with introducing seed particles into a single stream of a fuel and freestream mixing and combusting region of the scramjet flowpath. The velocity bias is quantified by measuring the velocity field at the combustor exit using stereoscopic PIV (SPIV) under three seeding scenarios: 1) fuel stream only seeded, 2) fuel and freestream seeded, and 3) freestream only seeded. The measurements serve to isolate the effect of the seeding method on the ensemble averaged quantities of mean velocity and RMS velocity. The case of seeding both the fuel and freestream was taken as the baseline, or most ideal solution. The results indicate that the effect of seeding bias is relatively small since seeding the fuel only, results in an average seeding bias error of 3.7% in mean velocity

and 2.5% for the case of freestream only seeded. For RMS velocity, the average error induced by seeding bias was 6.6% and 4.1% respectively.

5.1 Measurement of Velocity Bias due to Seeding Method

5.1.1 Introduction and Background

Particle Image Velocimetry (PIV) is an increasingly utilized fluid flow diagnostic technique to measure multiple components of velocity in a plane. As the technique has matured over time both the complexity of the measurement system and the difficulty of the application flowfield has increased. One such example is the application of Stereoscopic Particle Image Velocimetry (SPIV) to a Dual-Mode Scramjet (DMSJ) model combustor to measure the three dimensional combusting flowfield [34, 59]. Measurement of velocity provides critical information concerning the transport of fuel, air and combustion products, as well the turbulent nature of the flow. The measurements are particularly difficult due to many factors including: a high-speed flow with large dynamic range and velocity gradients; highly turbulent and three dimensional flow; elevated temperatures in excess of 2000 K; limited optical access; particle seeding restraints; and window fouling. One of the most prohibitive challenges with the measurement is window coating/fouling due to particle adhesion to the windows. Particles build a static charge due to collisions with walls and other particles causing an attractive force toward the windows. In addition, the elevated temperatures result in a thermophoretic effect in the slow moving boundary layer that causes particles to adhere to windows [60, 61]. As particles coat the windows, the signal-to-noise ratio is reduced in two ways: 1) cameras viewing through a translucent surface and 2) scattering of light due

to laser delivery through coated windows. This decrease of the signal-to-noise ratio degrades the quality of the PIV images resulting in depreciation of measurement accuracy and eventual loss of measurement area. As a result, the freestream air could not be seeded for the previous studies within the UVaSCF combustor due to rapid window coating and degradation of PIV images [31, 34, 59]. Out of necessity, only the fuel was seeded and this stream was introduced through a single fuel injector that was transversely separated from the windows. The spreading angle of the fuel plume was such that few particles reached the windows and this left the optical path clear. Ideally, both the fuel and freestream would be seeded in order to enable velocity determination across the entire measurement area and avoid velocity biasing errors.

Velocity bias can occur when seeding only one stream of a two stream flowfield particularly when there is a velocity difference between the two streams. It becomes increasingly significant in the extreme case of a high-speed stream mixing with a low-speed stream. In the case of the DMSJ, there exists a high-speed fluid freestream, a high-speed fuel jet core, and a lower speed fuel/air mixing/combusting region, depicted in Fig. 5.1. As the hydrogen and air mix, the combustion process decelerates the flow in that region due to heat release and separation. Theoretically, velocity bias can have an effect on all three velocity components. For the current flow, the highest velocity differential occurs in the axial x-direction, so therefore the U-component of velocity is assumed to be most influenced by velocity biasing.

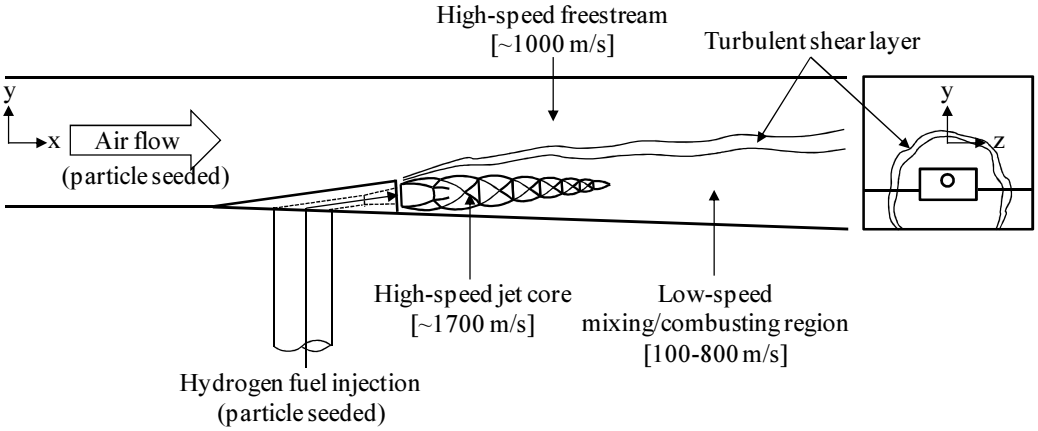

Fig. 5.1: DMSJ flow structures and seeding schematic.

Since PIV is dependent on measuring the displacement of particles, areas without seeding cannot generate velocity vectors. Therefore, when only seeding a lower speed region, for example, the mean velocity can be biased towards lower velocities [62]. This occurs when there are no particles present that originated from the high-speed stream. Due to the turbulent nature of the shear layer and interaction of the ramp induced vortices, fluid structures from the freestream may or may not be present in an instantaneous sense when only seeding the fuel in the present application. Therefore, ensemble averaging many instantaneous velocity fields in order to obtain mean velocity, $\bar{U}$, can bias towards the velocity of the seeded mixing/combusting region in the measurement plane in Fig. 5.2. In a similar way, seeding only one stream and not the other can lead to errors in the root-mean-square (RMS) velocity, u. Furthermore, velocity bias errors can also occur when only seeding a high-speed stream and not the low-speed stream. Seeding bias is typically mitigated by simply seeding both streams, but in the present application this is not possible.

There is little experimental data published which quantifies the magnitude of error caused by seeding bias for PIV studies in high-speed flows. McLaughlin and Tiedermann

[63] conducted laser Doppler Velocimetry (LDV) measurements of a turbulent boundary layer and reported mean velocities that were higher than theory predicted. It was proposed that higher speed velocities would deliver a greater number of particles per unit time through the probe area and thus result in a greater number of velocity measurements for the high-speed flow and thus biasing the mean velocity. This form of bias is widely recognized for LDV measurements and several authors have proposed methods for correcting the velocity the error [64, 65, 66]. The most common correction is an inverse velocity weighting which has been shown to decrease the velocity bias. A common method for assessing the velocity bias error, by Meyers [64], reasons that if high velocities increase the data rate and low velocities decrease the data rate then there must be a correlation between velocity and data rate. This velocity-data rate correlation has been utilized by Petrie [65] and Bulusu [67] for the assessment of velocity bias in high-speed shear layers. For PIV experiments, high velocity does not increase the data rate and low velocity does not decrease the data rate. Therefore there should not exist a correlation between velocity and data rate. Alternatively, when two streams are seeded, velocity bias could occur if one of the streams has a greater particle density or size resulting in higher intensity correlations and more frequent vector calculation of one stream.

A study by Smith [68] pertaining to Planar Doppler Velocimetry (PDV) measurements of a M=0.85 compressible jet addressed seeding of a co-flow surrounding a core flow. When seeding the co-flow only, no experimental data was attainable past a certain jet radii due to the lack of particles. In the region of the co-flow there was excellent agreement of velocity data for the cases of seeding the co-flow only, the core flow, and both streams. The study also showed excellent agreement over the entire

measurement area for the case of the core-flow seeded and both streams seeded. This would indicate that in the case of the present study, seeding the fuel only would result in less overall disagreement. Li et al [69] addressed velocity bias errors due to concentration gradients of seed particles by conducting a Particle Tracking Velocimetry (PTV) experiment in a low speed turbulent channel flow and showed that the bias is proportional to concentration gradient. In addition Li et al [70] performed a computational study of velocity bias errors due to velocity gradients present in the flow of interest. While the issue of concentration and velocity gradients of seed particles is related to the present problem, it does not adequately answer the question of non-uniform seeding of a two-stream flow.

A similar study by Thurow [87] conducted PDV measurements in a supersonic compressible free jet during different seeding scenarios. The goal of the study was to measure the convective velocity of large scale coherent structures through the two-point space time correlation function. The study concluded that the convective velocity is very sensitive to which streams were seeded resulting in differences of approximately 50% in the most extreme case. The authors state, that this was mostly due to the method in which the space time correlation function was tracking coherent structures. For example, when seeding only the mixing layer, the velocity in the core flow is wrongly set to zero because there are not sufficient particles present. This creates an artificial interface between the mixing layer and core flow where the most defined flow structures occur in the high speed mixing layer as opposed to the co-flow. Therefore, the convective velocity is over-measured in this situation. For the current study, a mask is purposely defined such that there does not exist a clear boundary between areas with and without seeding. Therefore,

velocity vectors are able to be calculated everywhere in the measurement region and the bias is solely due to under sampling of a particular stream.

Several notable PIV experiments on scramjet combustors employ seeding methods that may potentially induce velocity bias errors. As a solution to window fouling problems, non-uniform seeding delivery methods for PIV measurements of scramjet combustors have been employed by Smith et al. [29, 32], Tuttle et al. [33], and Kirik et al [71]. In the experiments by Smith et al. the fuel was seeded and the delivered through the base of a ramp fuel injector. The spreading angle of the seeded fuel was such that the particles did not reach the windows. This is a major advantage and allows for quality PIV images to be taken in the mixing fuel plume area of a reacting scramjet. The drawback of seeding only the fuel is a smaller measurement area and possible errors due to velocity bias. The experiments by Tuttle et al. and Kirik et al. involved 2D PIV measurements in a high-speed cavity flameholder for scramjet applications. In these studies, the upstream boundary layer was seeded via angled wall injection located on the center plane of the flowpath. The particles were entrained in the cavity region allowing for measurements on the cavity centerplane. As a result of not seeding the freestream there is a possibility for biasing errors particularly in the region of the shear layer between the cavity recirculation and freestream. The motivation of the present study, therefore, is to quantify the effect of the inability to seed both the freestream and fuel stream with tracer particles during PIV measurements in a DMSJ. The present study is particularly relevant to the work of Smith et al. who used a similar scramjet flowpath and fuel injection scheme. In summary, the objectives of the research reported here are to:

1) Design an experiment that enables seeding of both freestream and fuel streams in a DMSJ flowpath such that PIV measurements can be obtained at a plane without windows that will foul.
2) Conduct an experiment to isolate the effect of velocity seeding bias by comparing three seeding cases of fuel only, freestream only, and both streams seeded.
3) Quantify the velocity bias error in mean and RMS velocity in order to draw conclusions on the presence of velocity bias in past, ongoing, and future PIV measurements.

This work represents the first quantification of velocity seeding bias in a DMSJ flowpath. Chapter 5.1.2 begins with a description of the facility and flow conditions.

5.1.2 Facility and Flow Conditions (Config. C_{mod})

As discussed in Chapter 2, Configuration C has been studied extensively within the NCHCCP through both experiments and computation modeling [37, 38, 39, 40]. The full Configuration C was not tested for the current study. The current experiments were conducted on a modified version of the flowpath, Configuration C_{mod} shown in Fig. 5.2, that consisted of only the isolator and combustor sections directly connected to the Mach 2 nozzle (ie the constant area section and extender removed). Measurements were conducted at the exit of the combustor section nearest to the point of fuel injection in order to most closely replicate the flow conditions in the scramjet combustor without the hindrance of windows. The lack of windows allowed velocity bias to be addressed because seeding of both the fuel stream and freestream were possible. In addition, the fuel does not spread far enough at the combustor exit such that there is a clear boundary

between the seeded and unseeded regions of the flow. The difference between Configuration C and Configuration C_{mod} are highlighted in Fig. 5.2 with the flowpath in bold black lines and the measurement plane at x/H=29 in a dashed white line.

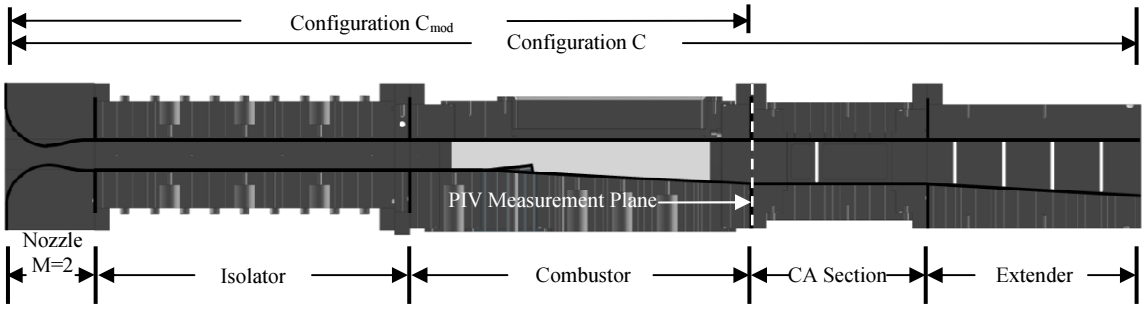

Fig. 5.2: UVa Supersonic Combustion Facility DMSJ flowpath side view.

The combustor section and ramp fuel injector were the same 10° unswept ramp fuel injector that is 12.7 mm wide and 6.35 mm high. Hydrogen fuel is injected through a Mach 1.7 conical nozzle located at the base of the ramp that is parallel to the face of the ramp. The injection-side wall starts a divergence of 2.9° at the leading edge of the compression ramp that is maintained until the exit of the combustor. The DMSJ flowpath terminates with an atmospheric backpressure at the exit of the combustor. The facility flow conditions and fuel equivalence ratios are presented in Table 1.

Table 5.1: Facility test conditions for Configuration C_{mod}.

Parameter	Air	Uncertainty	Fuel		Uncertainty
			Case A	Case B	
Equivalence ratio			.16	.27	±5%
Total pressure (kPa)	300	±1%	416	834	±3%
Total temperature (K)	1200	±0.8%	300	300	±3%
Mach number*	2.03	±1%	1.7	1.7	±0.5%
Static pressure* (kPa)	37	±1.4%	219	440	±3%
Static temperature* (K)	709	±1%	190	190	±3%

*Property at nozzle exit determined using nozzle areas and isentropic flow assumption.

The choice of test conditions was determined by selecting a scramjet mode of operation for Configuration C that produced atmospheric pressure at x/H=29 during combustion. For Configuration C at an equivalence ratio of 0.27, the pressure at the

combustor exit nearly matches atmospheric pressure. In order to match both the pressure rise due to combustion and the pressure at the exit of the combustor, an equivalence ratio of 0.16 was chosen for Configuration C_{mod}. The pressure trace in Fig. 5.3 indicates that both test cases depict a scramjet mode of operation with no pre-combustion shock train and supersonic flow at the combustor entrance.

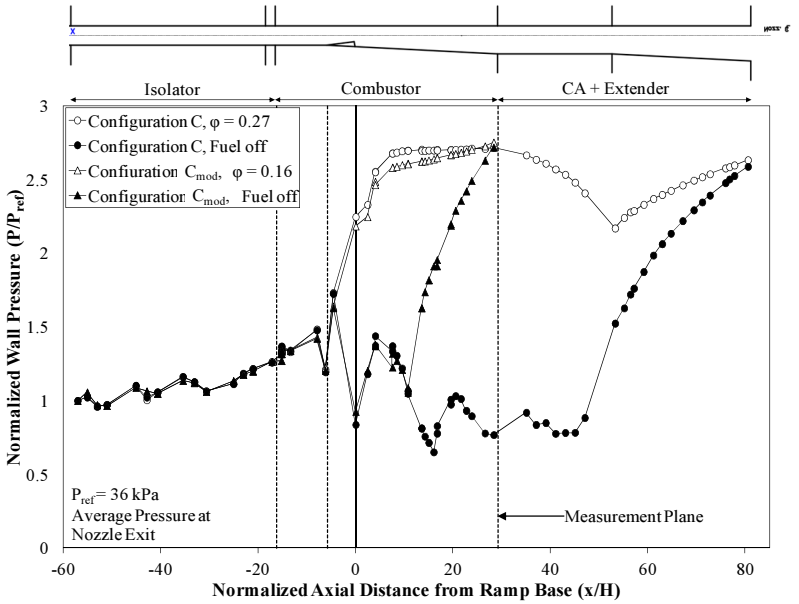

Fig. 5.3: Axial centerline static pressure distribution.

In both cases the pressure rise due to combustion and heat release begins at the point of fuel injection and the slope and magnitude is matched ending with atmospheric pressure at the combustor exit. The pressure traces show that flow within the combustor is essentially the same for both configurations. The fuel off pressure traces match well with the only difference being the onset of the exit shock train up to the atmospheric back pressure. It is therefore concluded that velocity seeding bias effects that are observed for Configuration C_{mod} will also be present in Configuration C.

5.1.3 Measurement Uncertainty Analysis

For PIV, the definition of velocity is the displacement of particles, Δx, divided by the time between pulses, Δt. Therefore the uncertainty in velocity is a combination of the random and systematic errors associated with displacement and timing. For a measurement of velocity, the uncertainty is a function of several independent variables, (a_1, a_2, a_3, ... , a_n) according to Eqn. 5.1.

$$U = U(a_1, a_2, a_3, \dots, a_n) \tag{5.1}$$

To illustrate the uncertainty analysis, the U-component of velocity is considered but the same procedure is performed for the W and V-component of velocity. The uncertainty in the measurement of U is defined as c_U and the uncertainties in each independent variable (a_1, a_2, a_3, ..., a_n) are c_1, c_2, c_3, ..., c_n. Based on those definitions and assuming each source of uncertainty has the same probability, the uncertainty in U, c_U, is defined according to Eqn. 5.2.

$$c_U = \sqrt{\left(\frac{\partial U}{\partial a_1} c_1\right)^2 + \left(\frac{\partial U}{\partial a_2} c_2\right)^2 + \cdots + \left(\frac{\partial U}{\partial a_n} c_n\right)^2} \tag{5.2}$$

The sources of uncertainty can be broken down into several categories. There are uncertainties due to the equipment, such as the camera, imaging optics, and laser source. There are also uncertainties due to particle slip and sampling. Lastly, the main source of uncertainly is due to the cross-correlation method or the ability of the processing algorithm to accurately predict the displacement of the particles.

Equipment

The primary sources of uncertainty associated with the equipment are calibration uncertainties of the imaging optics and timing uncertainties of the laser. The calibration

uncertainty results from scaling magnification uncertainty which relates the size of a pixel on the CCD to the physical size in the object plane and timing uncertainties refer to the separation between laser pulses.

To determine the uncertainty in scaling factor, the calibration target is utilized. The calibration procedure has been previously described where a precise dot pattern target is placed at the measurement plane to coincide with the laser sheet. The cameras image the calibration target and the conversion between pixels and physical space in mm is determined. The magnification is equivalent to the inverse of the reproduction ration according to Eqn. 5.3.

$$m = \frac{l}{L} = \frac{\xi}{f} \tag{5.3}$$

where l is the length of the physical calibration target in mm, L is the length of the calibration target in the image in pixels, ζ is the distance from the CCD to the object plane, and f is the camera lens focal length. For the current SPIV experiment the target length (l) was 50 mm and the length of the target in the image plane (L) was 1234.57 pixels resulting in a magnification of .0405 mm/pixel. According to the certification of the calibration target, the distance on the target is assumed to be accurate to within ±.035 mm (c_l). The distance of the target in the image plane is computed from two points in the image plane therefore contains an associated uncertainty of 1 pixel (c_{L1}). Typical uncertainties due to optical distortion and aberrations of the imaging optics have been reported in the literature as 0.5% of the length of the calibration target which is 6.17 pixels (c_{L2}) [88]. Lastly, there is uncertainty associated with the positioning of the calibration target which was mounted to a translational stage capable of 0.1 mm accuracy (c_ζ). Registration error is a systematic displacement error for SPIV due to misalignment

of the laser sheet and the calibration target [73]. In order to minimize this error source, a self-calibration procedure was performed after the manual calibration using the DaVis 7.2 software [74]. Weinke reported a maximum reconstruction error of 0.01 pixels for several reference calibrations which is negligible compared to the other dominant sources [74].

The random uncertainty in timing is due to laser jitter, delay generator jitter, and the pulse duration. The laser uncertainty due to laser pulse jitter has been previously estimated as ±1 ns (c_{t1}) for this experiment [28]. The uncertainty in the PTU-9 programmable timing unit which triggers the laser is stated to be ±1 ns (c_{t2}) by the manufacturer. Lastly, there is an uncertainty in Δt due to the laser pulse width of ±10 ns (c_{t3}) because the particles aren't truly frozen in time. Since the velocity is a product of the magnification, the displacement in pixels, and the laser pulse separation, the derivatives in Eqn. 5.2 can be evaluated in terms of the independent variables (l, L, ζ, and t) according to Eqn 5.4.

$$c_U = \sqrt{\left(\frac{\partial U}{\partial l} c_l\right)^2 + \left(\frac{\partial U}{\partial L} c_{L1}\right)^2 + \left(\frac{\partial U}{\partial L} c_{L2}\right)^2 + \left(\frac{\partial U}{\partial \xi} c_\xi\right)^2 + \left(\frac{\partial U}{\partial t} c_{t1}\right)^2 + \left(\frac{\partial U}{\partial t} c_{t2}\right)^2 + \left(\frac{\partial U}{\partial t} c_{t3}\right)^2} \qquad (5.4)$$

$$c_U = \sqrt{U_{avg}\left[\left(\frac{1}{L} c_l\right)^2 + \left(\frac{-l}{L^2} c_{L1}\right)^2 + \left(\frac{-l}{L^2} c_{L2}\right)^2 + \left(\frac{1}{\xi L} c_\xi\right)^2\right] + \left(\frac{U_{avg} l}{\Delta t L}\right)^2 [{c_{t1}}^2 + {c_{t2}}^2 + {c_{t3}}^2]} \qquad (5.5)$$

Based on Eqn. 5.5, the total equipment uncertainty in U, V and W is 2.87 m/s, .09 m/s, and .12 m/s respectively.

Particle Slip and Sampling

The uncertainty due to particle slip cannot be properly determined for the SPIV data based on Newton's law because a derivate in the x-direction for particle acceleration is not measureable. For an estimate, the particle slip is assumed in a 2-D sense where acceleration is only due to movement in the z- and y-direction. Performing a force

balance assuming only Stokes drag on the particle gives Eqn. 5.6 with the right hand term in parenthesis equal to particle acceleration.

$$U_{slip} = \frac{1}{18}\frac{\rho_p {d_p}^2}{\mu_f}\left(\frac{\partial U_p}{\partial x_p}\frac{dx_p}{dt} + \frac{\partial U_p}{\partial y_p}\frac{dy_p}{dt}\right) \tag{5.6}$$

This calculation is performed using finite difference to evaluate the derivatives at a point in the flow with large gradients. The viscosity was estimated based on Sutherland's formula. Performing this calculation reveals a slip velocity of .012 m/s for the W and V component of velocity with is negligible compared to the other sources. Since the slip velocity will be the most significant for the U-component but the derivative can't be evaluated in that direction, a typical value of 1% slip velocity has been assuming based on the literature [55].

The uncertainty due to a finite sample size, convergence uncertainty, is simply calculated by taking the 95% confidence interval for mean velocity. This is accomplished by calculating the uncertainty based on a 95% confidence interval according to $\sigma_{avg} = 1.96\sigma/\sqrt{N}$, where σ is the average RMS velocity and N is the sample size.

Cross-correlation

The random displacement error due to the cross-correlation technique is estimated by utilizing actual raw particle images and deforming the image by a known vector field, as discussed below [72]. Using actual particle images is advantageous because it takes into account parameters such as particle shape, particle size, particle intensity, seeding density, optical aberrations of the imaging lens, camera viewing angle, focal distance, and peak locking. The process for deforming the raw particle images is depicted in Fig. 5.14.

The LaVision DaVis 7.2 commercial software package was utilized for both data acquisition and data analysis.

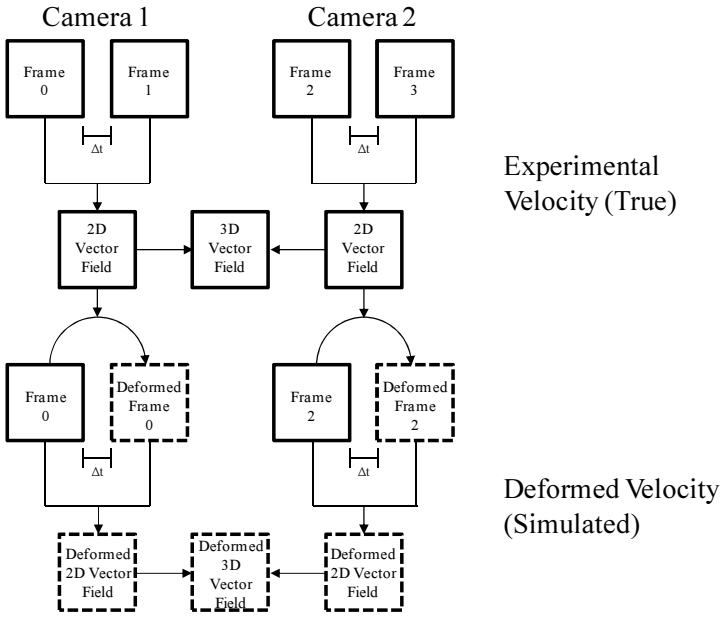

Fig. 5.4: Particle image deformation process for uncertainty estimation.

First, the standard cross-correlation algorithm calculates the appropriate instantaneous 2D vector fields for both cameras. These vectors are combined using the image-to-world calibration mapping function in order to determine what is assumed to be the "true" 3D experimental velocity field. The true 2D vector fields are then used to deform Frame 0 and Frame 2 from the respective camera. It is more accurate to utilize the assumed true velocity distribution to deform the particle images because they account for the velocity range, velocity gradients, and flow structures present in the experiment. The same standard cross-correlation algorithm from step 1 calculates the "deformed" 2D vector fields from both cameras and is then combined in the same way previously to generate the deformed 3D vector field. This provides a direct comparison between the true 3D velocity field and the deformed 3D velocity field. The average difference in U,

V, and W velocity between the true and deformed 3D velocity fields was 6.4 m/s, 1.3, and 2.2 with the average velocity U_{avg}, V_{avg}, and W_{avg} equal to 414 m/s, 13 m/s and 17 m/s. Using the time delay, Δt=800 ns, this average uncertainty in displacement due to cross-correlation is .00512 mm, .001 mm, and .0018 mm in U, V, and W respectively. Table 5.3 summarizes the PIV uncertainty sources in each component of velocity.

Table 5.3: Summary of PIV uncertainty sources.

Source	Velocity Component			Unit
	U	V	W	
Equipment				μm
Optics/Calibration	±2.3	±.07	±.09	N/A
Laser jitter	±1	±1	±1	nsec
Delay generator jitter	±1	±1	±1	nsec
Laser pulse separation	±10	±10	±10	nsec
Cross-correlation	±5.1	±1	±1.8	μm
Convergence	±2.8	±1.1	±1.5	m/s
Particle Slip	1%	1%	1%	N/A

To combine all sources of uncertainty, the root-sum-square is taken of the four primary sources due to equipment, particle slip, sample size, and correlation according to Eqn. 5.7.

$$\varepsilon_T = \sqrt{\varepsilon_{eq}^{\,2} + \varepsilon_{ps}^{\,2} + \varepsilon_{ss}^{\,2} + \varepsilon_c^{\,2}} \tag{5.7}$$

Performing this calculation for each component of velocity results in a total uncertainty of 8.8 m/s, 1.9 m/s, and 2.9 m/s for U, V and W. When taken as a percentage of the average velocity (U_{avg}=414 m/s, V_{avg}=13 m/s, and W_{avg}=17 m/s) the total percent uncertainty for U, V, and W respectively is 2.1%, 14.6% and 17.1%.

5.1.4 Results

Examples of raw PIV images, under different seeding scenarios, are first presented before examining the velocity field in the measurement plane of the flow. Bias in the

mean and RMS velocity are then examined. As will be seen below, the underlying velocity field had a significant effect on the distribution of the seeding bias. Sample raw particle images are shown in Fig. 5.5. The different seeding scenarios are apparent from left to right, with fuel only seeded, fuel and freestream seeded, and freestream only seeded.

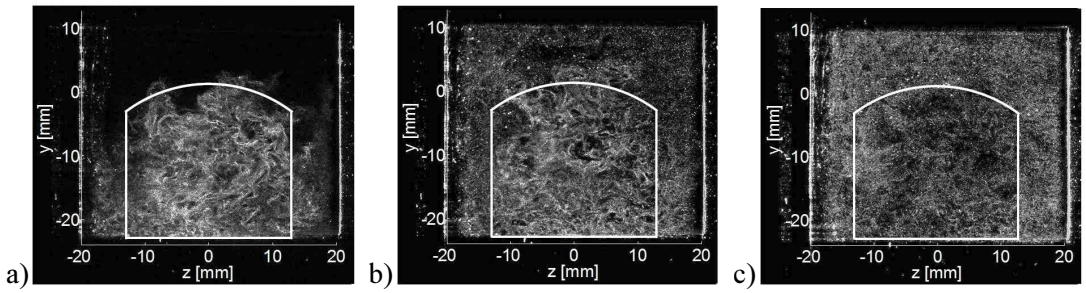

Fig. 5.5: Raw particle images: a) fuel seeded, b) fuel and freestream seeded, c) freestream seeded.

The white mask in each of the images indicates the measurement area of interest. The mask was generated by averaging of all images and creating a cut-off limit of intensity (typically on the order of 1000 counts) in order to eliminate areas with poor signal-to-noise ratio. The same mask is applied for all seeding cases in order to allow for a one-to-one comparison of the velocity fields and to isolate the effect of velocity bias. It can be seen that for these instantaneous snapshots, there is a greater population of areas of less dense seeding in both the case of fuel only seeded and the case of freestream only seeded. It is evident that, while there are still some regions of varying seed density, the ideal case is with both the fuel and freestream seeded. This results in the most uniform distribution of seed particles across the entire camera field of view.

Before addressing the velocity bias it is important to consider the convergence of the mean and RMS velocity to ensure the sample size used to determine these quantities is large enough. To ensure that the data is fully converged, the mean and RMS velocities

were calculated at varying number of samples and normalized by the reference velocity. A single point in the measurement plane is first considered. This point, located at z=0 mm and y=-6 mm, was chosen because it is located in a shear layer between the low-speed mixing and combusting plume downstream of the fuel injector, and the high-speed freestream. This point is thus associated with elevated levels of turbulence. Figure 5.6 shows the mean velocity in filled circles and the RMS velocity in unfilled circles, for this particular point in the flow. The corresponding 95% confidence intervals are plotted in dashed lines.

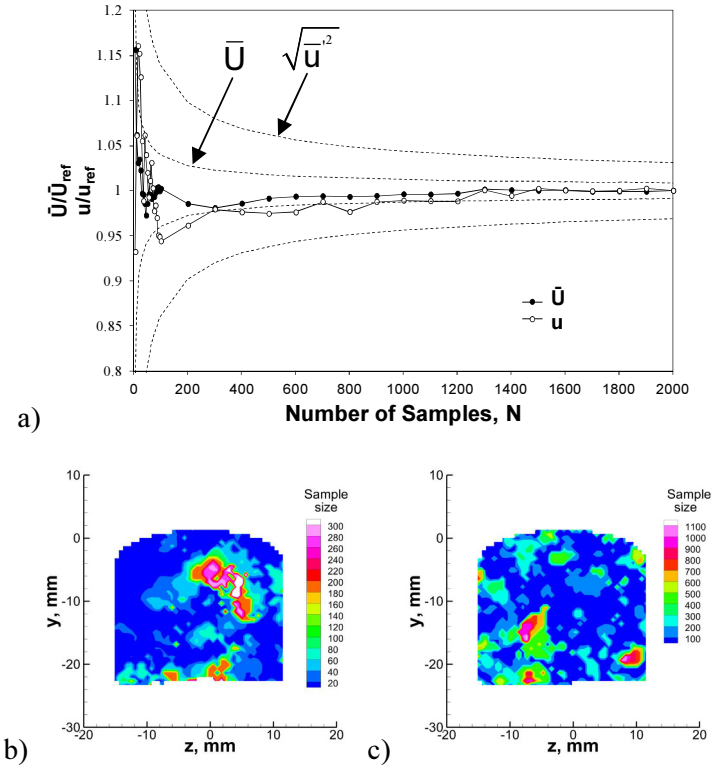

Fig. 5.6: Convergence of mean velocity, Ū, and RMS velocity, u: a) convergence at the point (0,-6), b) contour of vector count to converge to within 5% for mean velocity, c) contour of vector count to converge to within 5% of RMS velocity.

The same procedure was repeated for every point in the measurement area in Fig. 5.6(b)/(c) and the number of samples necessary to converge to within 5% of the final value was calculated. On average across the measurement area, the mean velocity and

RMS velocity converged to within 5% after 44 and 178 vector counts respectively. Therefore, the sample size of 2000 that was used in the present study is more than adequate to ensure convergence of the calculated statistical quantities.

In order to measure the error due to velocity bias, 2000 images for each seeding case were collected. All experimental parameters were kept constant in order to isolate the effect of seeding. Velocity bias can be potentially induced by the mixing of two fluid streams with significantly different velocities, therefore only the U-component of velocity is considered for this study. In order to better understand the flow features of the combusting DMSJ, Fig. 5.7 represents measured velocity field quantities (mean velocity, cross-plane vectors, and vorticity) for the ideal case where both fluid streams are seeded.

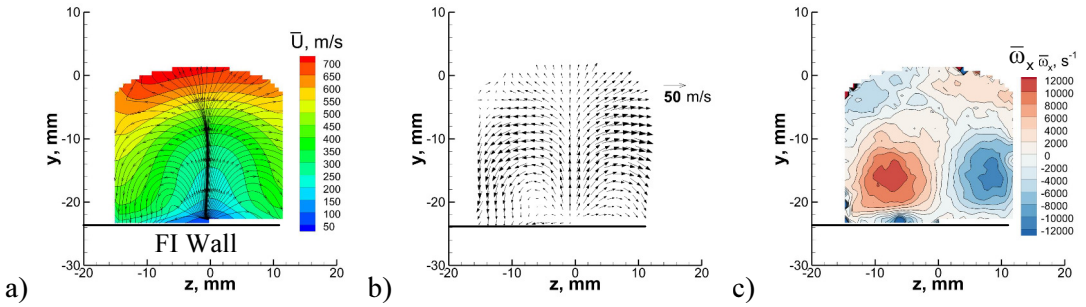

Fig. 5.7: Combustor exit plane velocity field with the fuel and freestream seeded: a) Mean velocity, $\bar{U}$, and $\bar{W}$, $\bar{V}$ streamlines, b) $\bar{W}$ and $\bar{V}$ cross-plane velocity vectors (every other vector displayed), c) vorticity in the x-direction, $\overline{\omega_x}$. The fuel injection (FI) wall is labeled in the Fig. 5.3.

The contours of axial velocity ($\bar{U}$) show a low-speed region close to the fuel injection wall with increasing velocities in both the z and y direction. A typical U-shaped velocity contour symmetric about z=0 mm is formed which has been experimentally observed for DMSJ combusting flows with ramp fuel injection [34, 59]. Figures 5.7(a) and 5.7(b) show two large counter-rotating vortices that are induced by the ramp fuel injector. The left vortex rotates in the counterclockwise direction and the right vortex rotates in the clockwise direction. The strength and extent of the vortices is evident in

Fig. 5.7(c) with typical vorticity values of 6000-10000 s^{-1} and a size of approximately 10 mm. The data of Figs. 5.7(a)-(c) indicate an asymmetric velocity field in terms of the in-plane vectors, streamlines and vorticity. This asymmetry is most likely due to in asymmetry in the velocity field at the inflow to the DMSJ flowpath or physical imperfections of the ramp. This asymmetry is in turn consistent with a static temperature non-uniformity that was measured at the inflow plane by Ref. [39].

Figures 5.8(a)-(c) show a comparison of the mean velocity contour for all three seeding cases in order of fuel only seeded, fuel and freestream seeded, and freestream only seeded.

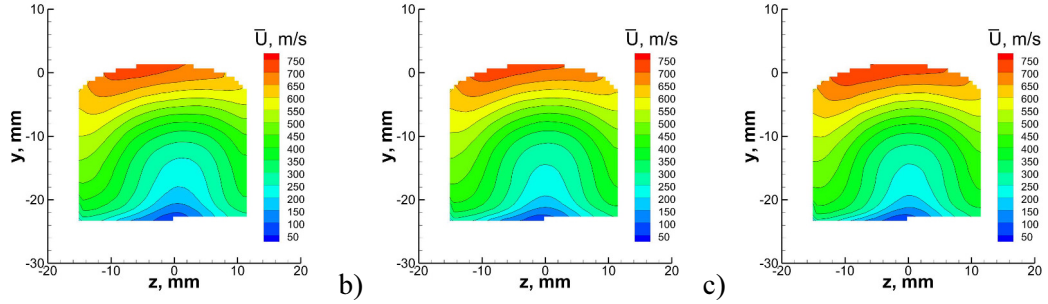

Fig. 5.8: Mean velocity, Ū, contour: a) fuel seeded, b) fuel and freestream seeded, c) freestream seeded.

Overall, the shape and magnitude of the velocity contours match very closely. It is evident that the case of both streams seeded and freestream only seeded have slightly more agreement and exhibit slightly more symmetry than the case of fuel only seeded. The case of fuel only seeded exhibits more asymmetry due to an asymmetric inflow in which velocity bias is more prevalent and velocity on the right hand side is under measured. To highlight the similarities and differences, a horizontal line profile at y=-11 mm and a vertical line profile at z=0 have been plotted in Fig. 5.9. The difference from the ideal case of both streams seeded is presented in the subplot.

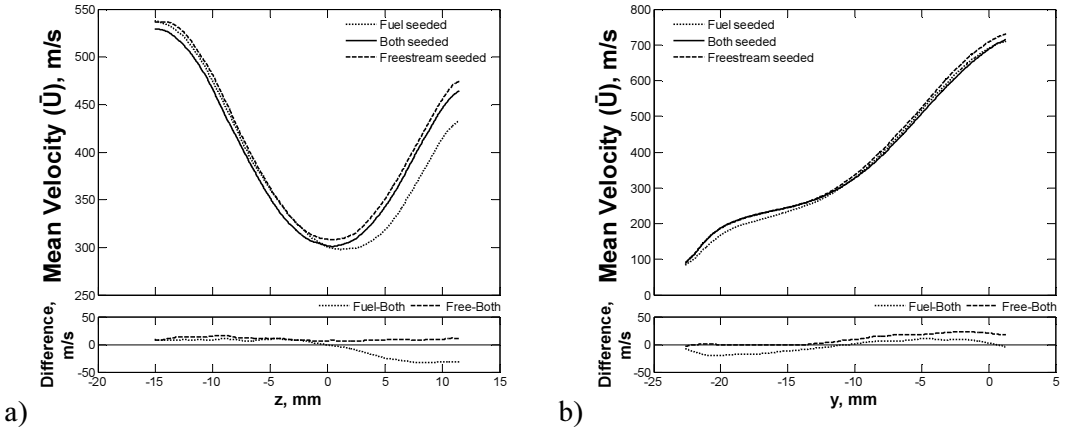

a) b)

Fig. 5.9: Mean velocity, $\bar{U}$, profiles: a) horizontal profile at y=-11 mm, b) vertical profile at z=0 mm.

For the horizontal profile in Fig. 5.9(a) there is very good agreement for all three seeding cases until positive z values where the fuel only seeded case starts to diverge. In this region, the difference between the case of fuel seeded and both only seeded is approximately -40 m/s indicating that the measurement is biased towards the lower speed fuel plume when only seeding the fuel. This is to be expected as the mean velocity is biased towards the velocity of the seeded stream. The centerline vertical profile shows more agreement overall between the three seeding cases. In general, seeding the fuel only under-measures the mean velocity at low y and seeding the freestream only over-measures the mean velocity at high y. In order to quantify the order of magnitude of the velocity bias error over the entire measurement area, the percent difference is calculated by subtracting the velocity fields and dividing by the ideal case of both streams seeded (i.e $100\cdot(\bar{U}_{\text{fuel or freestream}}-\bar{U}_{\text{both}})/\bar{U}_{\text{both}}$). Figure 5.10 shows the percent difference of fuel seeded vs. both seeded and freestream vs. both seeded.

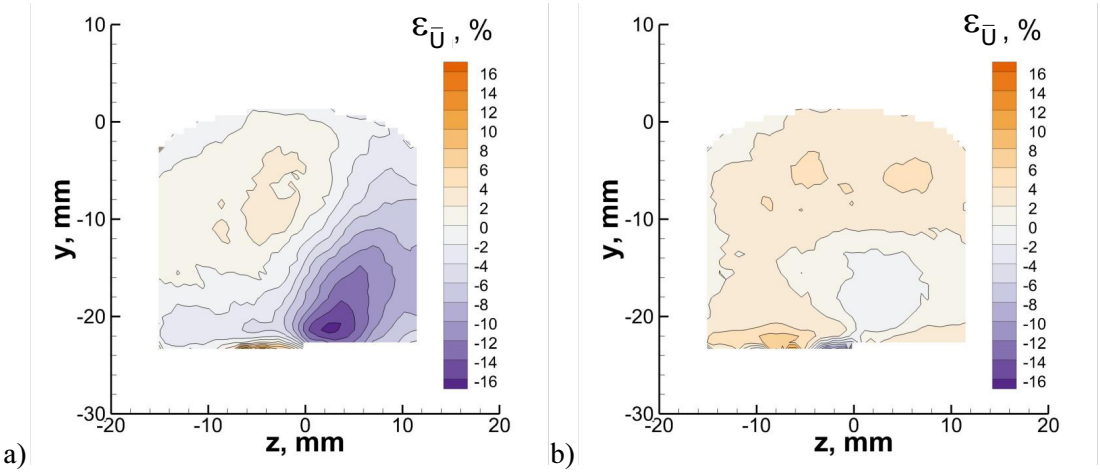

Fig. 5.10: Percent difference in mean velocity, $\bar{U}$: a) fuel seeded vs. both seeded, b) freestream seeded vs. both seeded.

When the percent differences are compared to the 2.1% experimental uncertainty estimate for mean velocity it is evident that seeding bias error is significant. For the comparison of fuel only seeded vs. both streams seeded there is a clear asymmetry about the z=0 line that is consistent with the earlier observations from Fig. 5.7. The freestream vs. both plot in Fig. 5.10(b) is more symmetric and has a low percent error in the center of the plume, with peak values in the shear layer towards the freestream. Overall, seeding the freestream only would appear to be advantageous compared to the fuel only case as it results in less bias error. However, the error is high in only one small region for the fuel seeded vs. both seeded case in Fig. 5.10(a). Integrating over the entire measurement area results in an average error of 3.7% for the fuel seeded vs. both seeded case, as opposed to an average error of 2.5% for freestream seeded vs. both seeded. The average level of seeding velocity bias is therefore relatively low in both cases.

In addition to mean velocity, turbulent statistics such as the RMS of the U-component of velocity (u) can incur errors due to velocity bias. Figure 5.11 presents the RMS velocity for the three seeding cases, in the same format as Fig. 5.6.

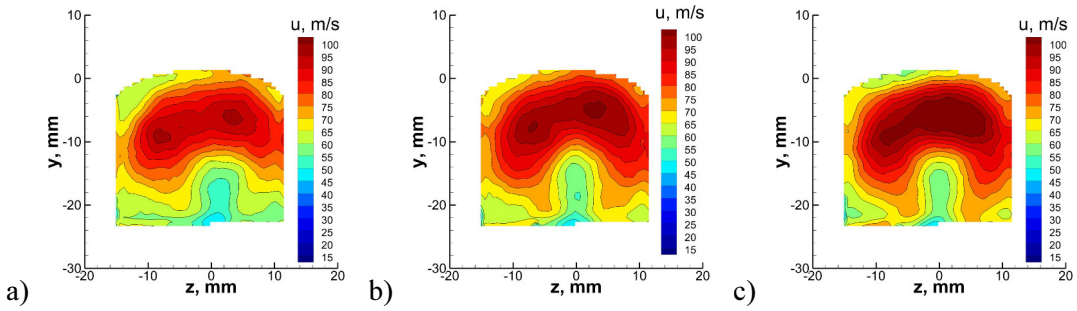

Fig. 5.11: RMS velocity contour: a) fuel seeded, b) fuel and freestream seeded, c) freestream seeded.

The contours indicate peak regions of turbulence in the kidney-shaped region centered at z=0 mm and y=-6 mm. The regions of peak turbulence are coincident with the shear layer between the mixing/combusting plume and the freestream, and with an overlay of the influence of the ramp induced vortices. The difference in RMS velocity between the three cases is more evident than for the comparisons of mean velocity in Fig. 5.8. Again, a horizontal line profile at y=-11 mm and a vertical line profile at z=0 mm is plotted for RMS velocity in Fig. 5.12.

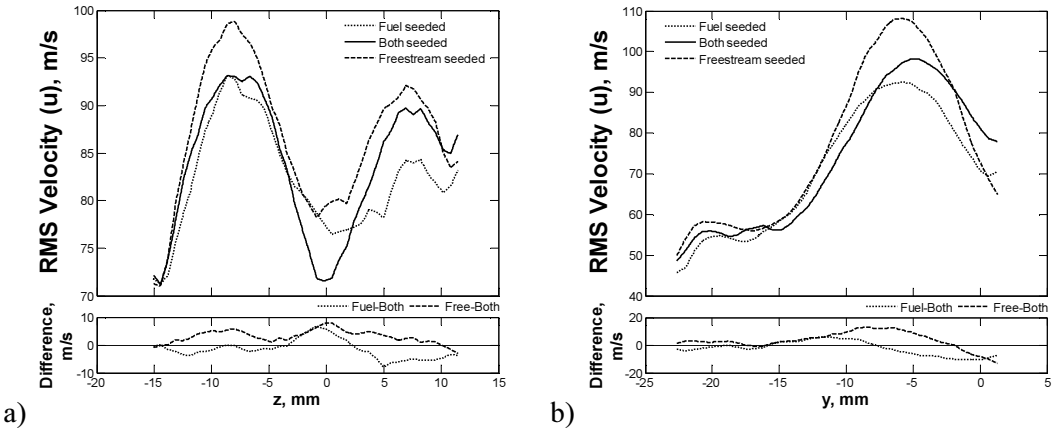

Fig. 5.12: RMS velocity profiles: a) horizontal profile at y=-11 mm, b) vertical profile at z=0 mm.

For the case of fuel seeded the RMS velocity tends to be under-measured and for the freestream seeded case the RMS velocity is over-measured. This indicates that in an average sense, the freestream flow contains more turbulence than the fuel stream. This is

an expected finding because the air flowing over the compression ramp creates turbulent vortices. The percent difference of the two comparison cases is presented in Fig. 5.13.

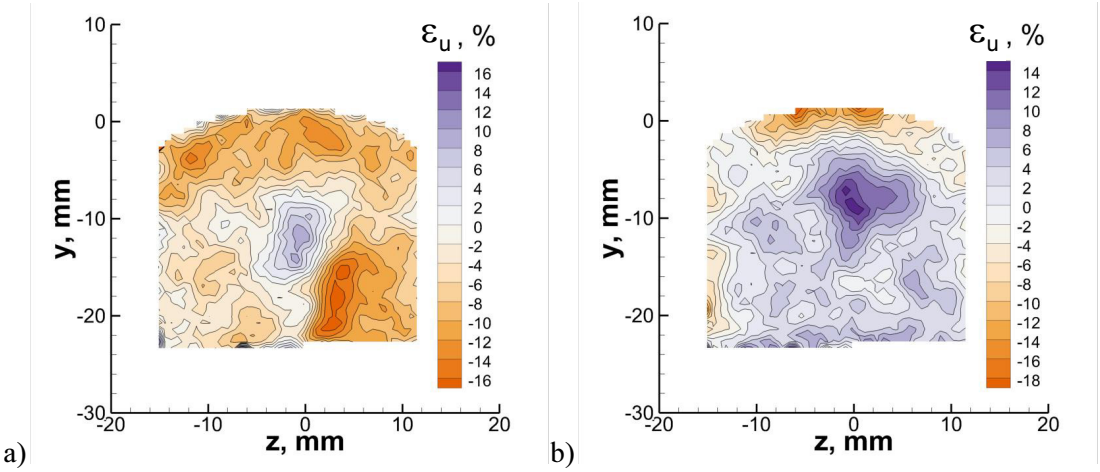

Fig. 5.13: Percent difference in RMS velocity (u): a) fuel seeded vs. both seeded, b) freestream seeded vs. both seeded.

Again, there is a slight asymmetry in the contour of fuel seeded vs. both seeded with higher values appearing on the right hand side of the line z=0. In general, the errors are the smallest for the freestream vs. both case with peak values in the center of the measurement area. A summary of the average and maximum absolute percent error in mean velocity and RMS velocity is presented in Table 5.2.

Table 5.3: Summary of velocity bias percent error for mean and RMS velocity.

	Both seeded vs. fuel seeded only		Both seeded vs. freestream seeded only	
	Average	Max	Average	Max
$\varepsilon_{\bar{U}}$	3.7%	16.6%	2.5%	8.6%
ε_u	6.6%	16.9%	4.1%	15.4%

The asymmetry in error due to velocity bias is a result of asymmetric mixing between the lower velocity mixing and combusting fuel-air plume with the higher velocity freestream. It is first noted that the streamlines and cross-plane velocity vector field (Fig. 5.7) show that the left vortex has a tighter turning radius and slightly higher strength that the right vortex. To aid in the interpretation of this observation, Coherent Anti-Stokes Raman

Scattering (CARS) data of average static temperature and nitrogen mole fraction are shown in Fig. 5.14 [39]. These measurements were taken at x/H=38 in the Configuration C DMSJ flowpath. This plane was 5.6 cm downstream of the present SPIV measurements and is therefore representative of the flow at the measurement plane in Configuration C_{mod} of the present study.

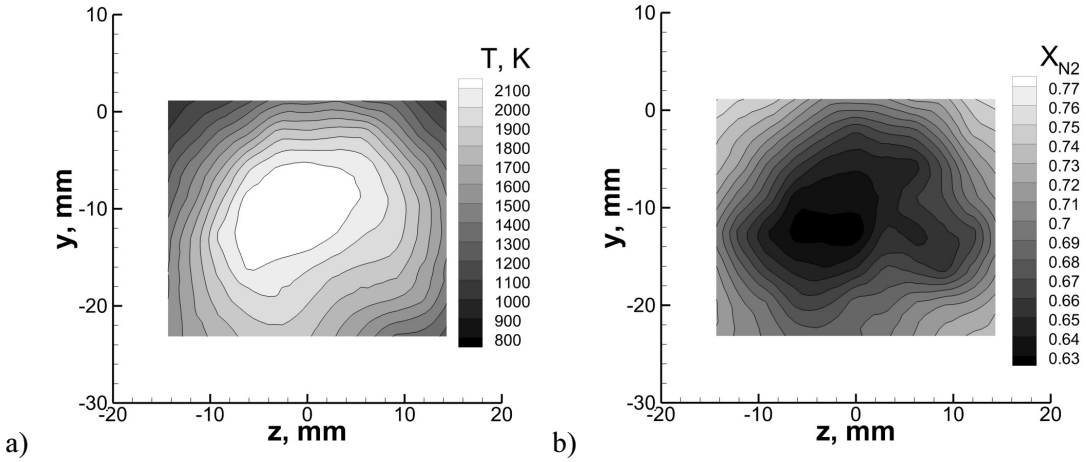

Fig. 5.14: CARS data: a) temperature, b) N_2 mole fraction.

The CARS measurements indicate an asymmetry in temperature and N_2 mole fraction that is consistent with the asymmetry in the velocity field that was observed in Fig. 5.7. One explanation for the asymmetry in the CARS measurements is an asymmetric inflow temperature distribution and physical asymmetries of the compression ramp causing asymmetric vortices and mixing capability. It is evident that the left hand vortex is more effective at mixing the fuel and air resulting in higher combustion efficiency and hotter temperatures. Reference to Fig. 5.7(c) shows that both ramp-induced vortices are slightly shifted to the right. This means that the right hand vortex is displaced further away from the hot central core of the mixing and combusting fuel-air plume. As a result, the right hand vortex convectively transports a greater fraction of cooler freestream air into the

plume that the left vortex. This results in the right hand side of the plume being cooler, as shown in Fig. 5.14(a). The vortex also transports more freestream nitrogen into the mixing and combusting plume, which displaces the hydrogen fuel and combustion products. This results in a higher mole fraction of nitrogen in the right hand side of the plume as shown in Fig. 5.14(b). The effect is particularly evident at positive x values and y values below -12 mm in Figs. 5.14(a) and 5.14(b). This is the same region that high levels of velocity bias were observed for the case of fuel only seeding in Fig. 5.10. In this case, the right vortex is transporting a greater amount of unseeded freestream air into the seeded fuel-air mixing and combusting plume. Since coherent pockets of freestream air that are convected into the plume are not seeded, they do not contribute to the PIV velocity measurement and resulting mean calculated quantities. Therefore, in this region, the process results in biasing towards the lower speed seeded plume. As would be expected, when the freestream is only seeded and not the fuel plume, such as depicted in Fig. 5.10(b), a field that is generally inverse of Fig. 5.10(a) results. Reference to Figs. 5.13(a) and 5.13(b) reveals that the asymmetric vortex field also have an influence on this bias in RMS velocity.

5.1.5 Conclusions

The experimental limitation of single-stream seeding of a two stream flow in previous PIV experiments in the UVaSCF has motivated the study of seeding velocity bias. A suitable measurement plane at the exit of the combustor section, which is the closest in proximity to measurement planes of interest in the combustor, has allowed the assessment and comparison of three seeding cases. It is assumed that seeding both the

fuel and freestream is the ideal case in which no velocity bias errors are incurred. Based on the results of the study there does exist a small bias associated with seeding either just the fuel, or just the freestream, in both mean velocity and RMS velocity. Averaging over the measurement area results in a 3.7% absolute bias in mean velocity associated with seeding only the fuel and a 2.5% absolute bias when seeding only the freestream. Similarly, there is a 6.6% bias in RMS velocity associated with seeding only the fuel and a 4.1% bias when seeding only the freestream. There was one small area for the case of fuel only seeded where biasing was significantly higher than the quoted averaged bias quantities which is in part due to the fact that the velocity in this region is small. However, approximately 90% of the measurement region of interest had a bias in mean velocity of less than 10%. While these errors are important to quantify and locate, they are generally relatively small. Therefore, the results of previous PIV studies that involved only seeding the fuel in a similar scramjet combustor remain valid and useful for understanding the flow and for comparisons with computational models. Finally, it has been shown that the distribution of seeding induced velocity bias is dependent on the structure of the underlying velocity field, and further, independent instream measurement techniques can be used to help predict the location of regions of high seeding bias.

Chapter 6

SPIV Experimental Results x/H=6, 12, 82

The objective of this investigation is to measure the three-dimensional velocity field, on the cross-plane, at three axial stations within a DMSJ flowpath operating in both the scramjet mode and ramjet mode of combustion. Of particular interest is to use the measurements to characterize the strength and size of the counter-rotating vortices which act to enhance the mixing of the fuel and air. This is especially important for understanding how mixing changes for the different modes of DMSJ operation. Key metrics such as turbulent kinetic energy and turbulence intensity can be calculated. The differences imparted in such metrics have not been reported previously in the literature and add to the understanding of the turbulent nature of the DMSJ flow. The experimental results presented at x/H=6, 12 and 82 during both the ramjet mode and scramjet mode of operation constitute the main results of the current chapter. First, the axial pressure trace is presented for the case of fuel-off, φ=0.18, and φ=0.49. The flow conditions are briefly examined based on the pressure trace and a simple 1-D flow analysis. Next, several contour plots of instantaneous U velocity, mean velocity magnitude, in-plane velocity vectors, vorticity, and turbulent kinetic energy (TKE) are presented. General observations are made and several trends comparing the axial development of the flowfield and comparison of the ramjet mode to the scramjet mode.

6.1 Scramjet Mode and Ramjet Mode Combustion

6.1.1 Static Pressure

The axial static pressure distributions in the DMSJ flowpath are first considered in order to examine the characteristics of the fuel-air mixing and combustion environment at the test conditions of interest. Fig. 6.1 shows typical axial pressure traces along the centerline of the flowpath at different fuel equivalence ratios. The results demonstrate the operating range of the UVaSCF, from fuel-off, to fuel-on with scramjet mode and ramjet mode. The SPIV measurement planes are indicated with green lines superimposed on the tunnel flowpath schematic above the pressure trace.

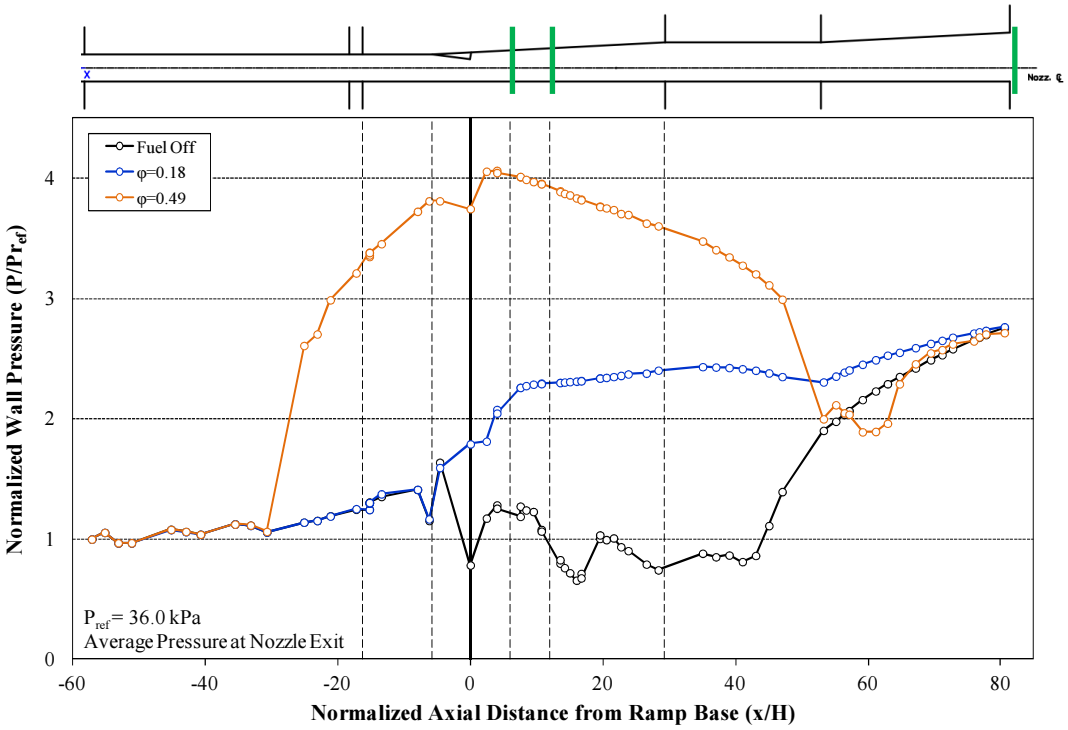

Figure 6.1: Axial pressure distributions, Config. C (fuel off, fuel-air reaction at φ=0.18 and φ=0.49).

Fuel is injected at the base of the ramp, designated x/H=0, and is represented by a bold vertical line in the figure. The dashed vertical lines represent the combustor entrance (x/H=-16.2) and ramp leading edge/start of divergence (x/H=-5.7), as well as the x/H=6

and x/H=12 combustor measurement planes, and the combustor exit (x/H=29). Measured pressure has been normalized by the static pressure at the exit of the facility nozzle, P_{ref}. The fuel-off case shows a slight rise in pressure along the isolator due to boundary layer growth and deceleration of the flow. Assuming one-dimensional, viscous flow in the isolator according to Fanno flow property changes in a constant area duct, the pressure and temperature ratios are given by Eqn. 6.1 and 6.2.

$$\frac{p_2}{p_1} = \frac{M_1}{M_2}\sqrt{\frac{T_2}{T_1}} \tag{6.1}$$

$$\frac{T_2}{T_1} = \frac{\left(1+\frac{\gamma-1}{2}{M_1}^2\right)}{\left(1+\frac{\gamma-1}{2}{M_2}^2\right)} \tag{6.2}$$

In Eqn. 6.1-6.2 the property at station 1 refers to the exit of the nozzle and station 2 refers to the leading edge of the ramp fuel injector (start of divergence). Using the measured static pressure, the nozzle exit Mach number (M=2.03), and γ=1.34, the equations can be arranged to solve for M_2 which reveals the Mach number at the leading edge of the ramp to be 1.57. The presence of the ramp is indicated by a rise in pressure at the ramp leading edge due to an oblique shock followed by a drop in pressure as the air expands over the end of the ramp. Referring to the combustion conditions, the scramjet-mode of operation is evident at φ=0.18 where there exists no pressure rise upstream of fuel injection. Since the pressure at the combustor entrance is the same as for the fuel off case, again, the Mach number at the leading edge of the ramp is 1.57. At φ=0.18 the predominant increase in pressure in the combustor section is due to the existence of a reacting flame. Heat addition increases the pressure in the supersonic flow throughout the combustor and at the downstream end a shock train in the extender equilibrates to the atmospheric back pressure.

As the fuel pressure is increased, the engine transitions to the ram-mode where an upstream pressure rise due to the pre-combustion shock train is apparent. The Mach number at the ramp leading edge in ram-mode is calculated based on a separated flow model of the isolator due to Heiser and Pratt [1] given by Eqn. 6.3.

$$M_2 = \left\{ \frac{\gamma^2 {M_1}^2 \left(1+\frac{\gamma-1}{2}{M_1}^2\right)}{\left(1+\gamma {M_1}^2 - \frac{p_2}{p_1}\right)^2} - \left(\frac{\gamma-1}{2}\right) \right\}^{-1/2} \tag{6.3}$$

Using the nozzle exit Mach number and the measured pressure ratio, Eqn. 6.3 reveals the Mach number at the leading edge of the ramp to be 0.8 for the φ=0.49 case. In this case, heat addition in the subsonic flow decreases the pressure in the combustor. A thermal throat is formed at x/H=53 where decreasing pressure in the diverging extender indicates transition to supersonic flow. As with the φ=0.18 case and fuel-off case, a shock train in the extender brings the pressure up to the atmospheric exit pressure. SPIV measurements were taken at φ=0.18 and φ=0.49 in order to capture the key aerodynamics of both modes of operation.

6.1.2 Three-component velocity

SPIV results for fuel-on conditions in both scram-mode (φ=0.18) and ram-mode (φ=0.49) at x/H=6, x/H=12, and x/H=82 are presented below. A sample raw data set containing image pairs from both cameras is shown in Fig. 6.2. The injection-side wall can be seen on the left of the image for camera 1 and on the right of the image for camera 2 due to viewing perspectives 180 degrees from each other.

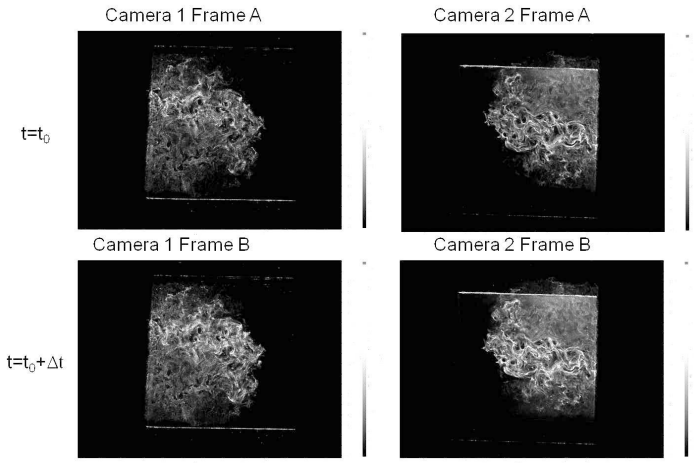

Figure 6.2: SPIV raw image pairs from camera 1 and camera 2.

The images have units of particle intensity and show a high seeding density and high signal-to-noise ratio. It is also evident that only the fuel plume is seeded and thus part of the tunnel area is not seeded. To demonstrate the high quality of the SPIV particle images, Fig. 6.3 represents typical correlation maps for camera 1 and camera 2.

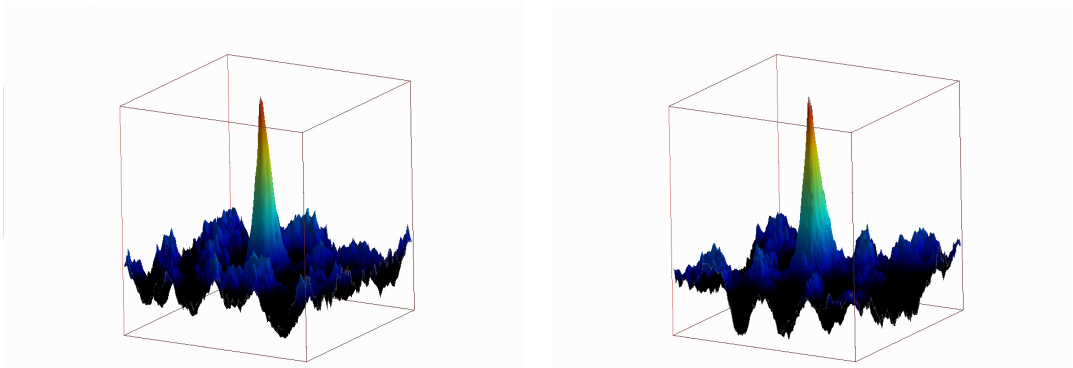

a) b)

Figure 6.3: Correlation peak 3D contour map: a) camera 1, b) camera 2.

The cross-correlation peaks are distinct and clear and there is a high degree of confidence that the accurate displacement has been found. The peaks are sharp and the height of the peak is approximately 3 times that of the noise. The image pairs from both cameras are necessary for a single three-component instantaneous velocity field measurement.

Average quantities are then calculated from a set of 2000 calculated instantaneous velocity measurements. Based on previous SPIV studies performed on the UVaSCF (Fig. 5.6), on average, across the measurement region the mean velocity converged to within 5% of the final value after a sample size of 44 vector counts and RMS velocity converged to within 5% after 178 vector counts [76].

The SPIV mean velocity fields and derived quantities are presented in Figs. 6.4-6.8. For each plane at each equivalence ratio, contour plots are presented of instantaneous U velocity with overlayed in-plane velocity vectors (Fig. 6.4), mean velocity magnitude ($|\bar{V}|$) (Fig. 6.5), mean in-plane velocity vectors ($\bar{V}$ and $\bar{W}$) (Fig. 6.6), mean out-of-plane vorticity ($\bar{\omega}_x$) (Fig. 6.7), and turbulent kinetic energy (TKE) (Fig. 6.8). The three latter quantities are defined in Eqns. 6.4-6.6:

$$\left|\bar{V}\right| = \sqrt{\bar{U}^2 + \bar{V}^2 + \bar{W}^2} \tag{6.4}$$

$$\bar{\omega}_x = \frac{\partial \bar{W}}{\partial y} - \frac{\partial \bar{V}}{\partial z} \tag{6.5}$$

$$TKE = \frac{1}{2}\left[\overline{(u')^2} + \overline{(v')^2} + \overline{(w')^2}\right] \tag{6.6}$$

For clarity, only every other vector is plotted in Fig. 6.6. Note that it was necessary to mask off portions of the plume in the z-direction due to laser reflections. For Figs.6.4-6.8, the injection-side wall (location of the ramp fuel injector) is located on the bottom of the contour plot according to the axes in Fig. 2.2. In this coordinate system the positive x-direction is out of the page and z=0 mm, y=0 mm corresponds to the middle of the duct in the combustor before divergence. The results are presented in order of measurement plane from left to right (x/H=6, x/H=12, and x/H=82) and equivalence ratio from top to bottom (φ=0.18 and φ=0.49).

The typical 3-dimensional instantaneous velocity fields, presented in Fig. 6.4, show contours of the axial velocity component (U) with the transverse velocity vectors (W and V) overlaid. Both the high-resolution and quality of the SPIV data is demonstrated. For display purposes, the contour plot of Fig. 6.4 was interpolated to fill in rejected vectors. For all mean quantities, no vector interpolation is performed is a vector is rejected due to the processing algorithm. Small turbulent structures are apparent at all measurement planes and fuel equivalence ratios. The chaotic nature of the flow is apparent in the cross-plane vectors, however, systematic structure is evident in the U-component contours. Small vortical structures are evident from the transverse velocity vectors. In particular, key flow features such as a velocity gradient, or a shear layer, can be seen in the φ=0.18 case and the high-seed core of the fuel jet can be seen in the φ=0.49 case. As the axial distance (x/H) increases, the turbulent structures and length scales increase in size.

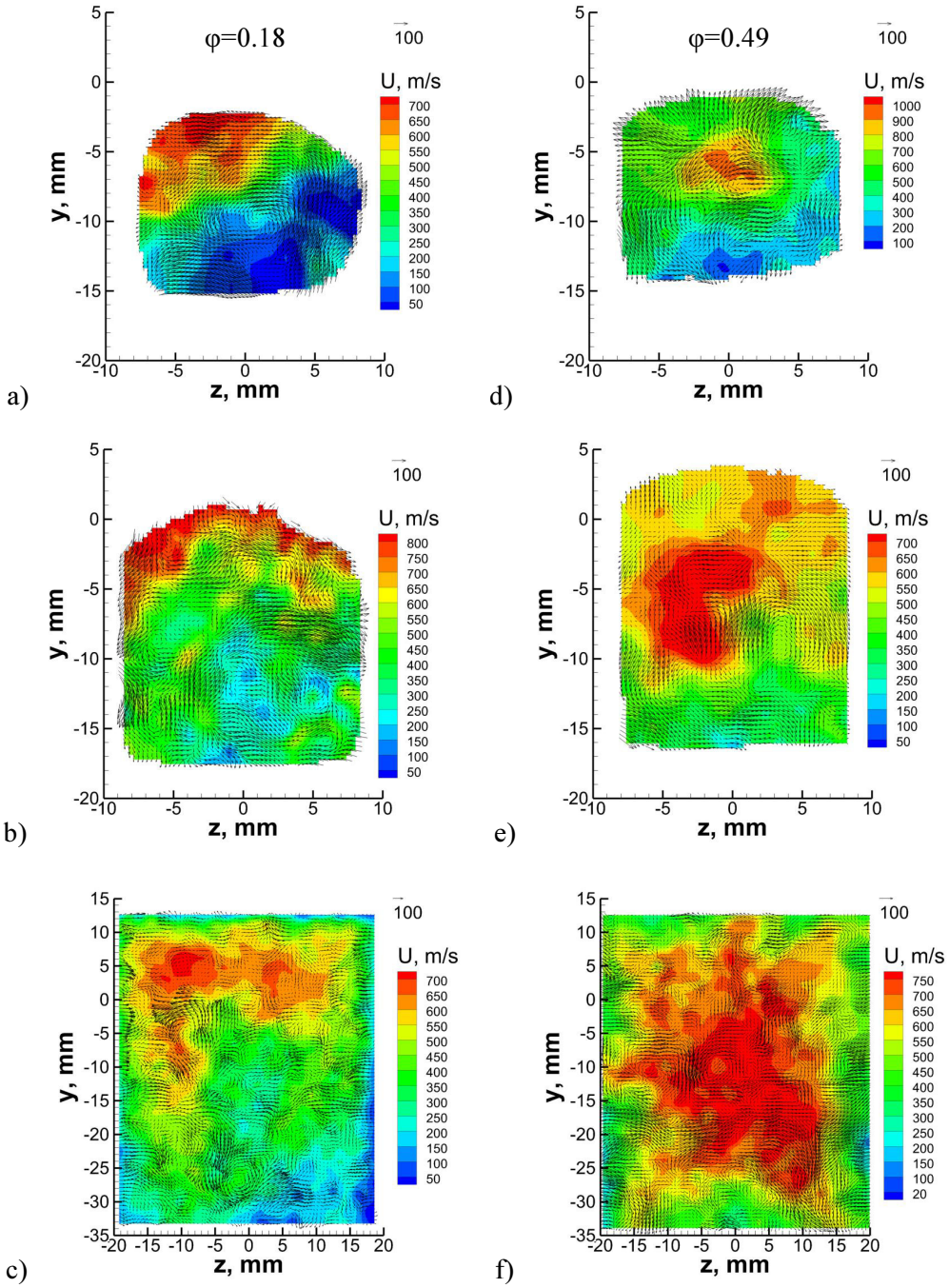

Fig. 6.4: 3D instantaneous velocity fields (contour colored by U with V, and W vectors): a) x/H=6, φ=0.18, b) x/H=12, φ =0.18, c) x/H=82, φ =0.18, d) x/H=6, φ =0.49, e) x/H=12, φ =0.49, f) x/H=82, φ =0.49

Mean velocity magnitude contour plots are presented in Fig. 6.5. At x/h=6 and φ=0.18 (Fig. 6.5a), reference to the spatial location of the velocity contours (which represent the presence of seed particles) will reveal that the fuel plume is relatively small

and has not spread significantly. The effect of the ramp induced vortices is dominant and a kidney-shaped velocity field is present. There is a low-speed region close to the fuel injection wall due to separation and heat release caused by combustion.

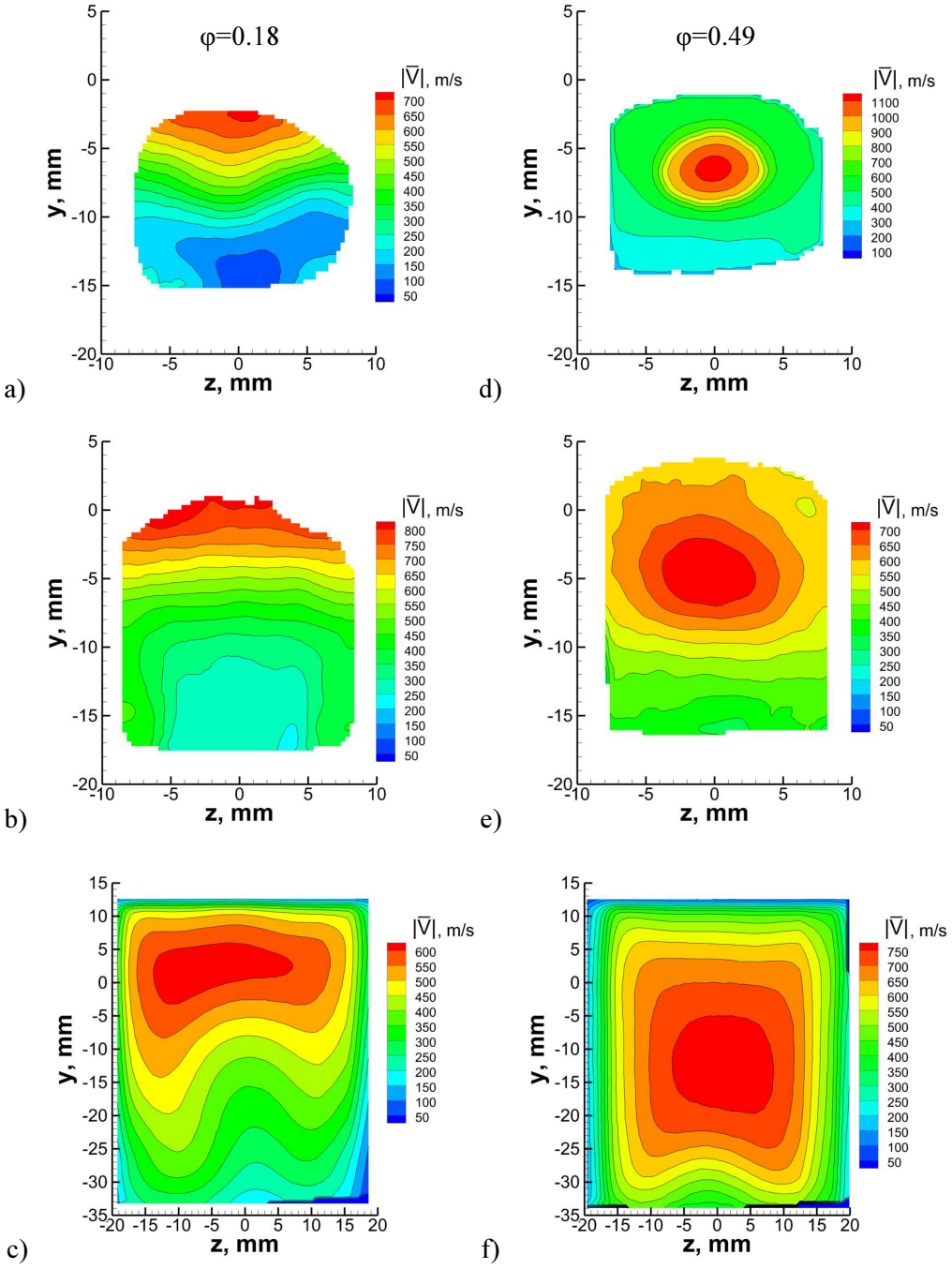

Fig. 6.5: 3D mean velocity magnitude ($|\bar{V}|$): a) x/H=6, φ=0.18, b) x/H=12, φ =0.18, c) x/H=82, φ =0.18, d) x/H=6, φ =0.49, e) x/H=12, φ =0.49, f) x/H=82, φ =0.49

The velocity increases in the y-direction toward the freestream of approximately 700 m/s. Despite a small low-speed region the flow, as indicated by the pressure distribution, is predominantly supersonic and the velocities continue to increase in the y-direction. In the freestream, outside of the measurement area, the velocities are expected to be approximately 900 m/s based on a Mach number of 1.57 and freestream temperatures of approximately 850 K. At x/H=12 and φ=0.18 (Fig. 6.5b), which is further downstream of the fuel injector, the fuel plume has obviously spread more than at x/H=6. The effect of the vortices on the velocity contour is less evident and the kidney-shaped distribution is beginning to form a U-shaped distribution that has been observed in scram mode in a similar scramjet flowpath [Rockwell]. This is most likely a result of the vortex strength, which is weaker at this location and slows the axial velocity to a lesser extent. There still exists low-speed flow in the region of the vortices but it is approximately four times the velocity magnitude than at x/H=6. At the exit of the extender section (x/H=82, Fig. 6.5c and 6.5f), seeding of both the fuel and freestream air is possible due to the lack of windows. As described earlier, freestream seeding is not possible in the combustor section due to particles coating the windows, which precluded imaging. Without the impediment of window fouling, velocity vectors can be measured across the entire duct of the exit plane. For the φ=0.18 case (Fig. 6.5c), the velocity profile forms a large U-shape which extends roughly half way into the duct. A relatively small high-speed freestream region is present at the top of the duct on the order of 600 m/s. There exists an asymmetry to the shape of the measured velocity contours which is not unexpected as no experimental facility is free from physical asymmetries. Physical asymmetries have been

verified by previous SPIV measurements, which showed asymmetric vortices, and CARS measurements that showed an asymmetric in-flow temperature distribution [39, 84].

Significantly for this study, it can be seen in Fig. 6.5 that the velocity field drastically changed once the flowpath was in the ram-mode of combustion. At x/H=6 and φ=0.49 (Fig. 6.5d), the flow field is characterized by a high-speed jet in the center of the fuel plume surrounded by lower speed flow. The fuel jet is predominant at the high equivalence ratio due to a higher fuel total pressure and the resulting greater axial penetration. The velocity in the freestream is expected to be approximately 550 m/s and the combustion consists of predominantly subsonic flow except in the region of the fuel jet which remained supersonic at x/H=6 due to proximity of the fuel injector. At x/H=12 and φ=0.49 (Fig. 6.5e), the flow field is similar to that at x/H=6 with the same fuel condition. The main difference is that the high-speed jet has spread and moved away from the wall as a result of the flowpath divergence and increased fuel penetration. The high-speed core resulting from the fuel jet is approximately 1.6 times slower than at x/H=6 due to deceleration of the under-expanded jet in the axial direction. At x/H=82, for the φ=0.49 case (Fig. 6.5f), the flowfield is characterized by a high-speed core of approximately 750 m/s surrounded by symmetrically decreasing velocities as the walls are approached. The velocity contour again forms a U-shape, but to a lesser degree, and does not penetrate into the flow to the same extent.

The dynamic range (50-800 m/s) of the velocities is very similar for both the scram and ram modes of combustion with the exception of x/H=6 and φ=0.49 which exceeds this in the jet core. For the combustor planes x/H=6 and x/H=12 operating in the scram mode is largely a low speed fuel-air mixing and combusting plume surrounded by a high

speed flow. Alternatively, the ram mode is characterized by a high speed fuel jet surrounded by a low speed flow. This is due to the pre-combustion shock train that lowers the freestream velocity. Lastly, the effect of the thermal throat in ramjet mode is evident with mostly greater velocities than the scram mode. With reference to Fig. 6.1, the pressure increases downstream of the thermal throat in ram mode which is accelerating the flow at the exit plane (x/H=82).

The transverse mean velocity vectors ($\bar{V}$ and $\bar{W}$) are presented in Fig. 6.6. The ramp induced counter-rotating vortices are the predominant flow feature for all planes and fuel equivalence ratios. A counterclockwise vortex is developed on the negative side of the z-axis and a clockwise vortex is developed on the positive side of the z-axis. The size of the vortex grows as the axial direction increases for both fuel conditions. At x/H=6 at φ=0.18 and φ=0.49 (Fig. 6.6a/6.6b), the left-side vortex appears to be closed vortex whereas the right vortex remains open. At x/H=12 for both φ=0.18 and φ=0.49 the size and extent of the vortices have increased and more symmetry is noticed than at x/H=6. For the scramjet mode of combustion the y-component of velocity (V) is predominantly downward (negative) towards the fuel injection wall whereas for the ramjet mode of combustion the V component of velocity is largely outward (positive) away from the fuel injection wall. This indicates that for the scramjet mode of operation more oxygen rich air was transported to the fuel-rich combusting plume. At x/H=82 and φ=0.18 the large elongated vortices extend nearly halfway into the duct whereas for the φ=0.49 case they remain close to the fuel injection wall and only protrude approximately 5 mm. For both modes of operation, at x/H=82, large components of W-velocity can be seed nears the edges of the duct where a significant amount of room air is entrained.

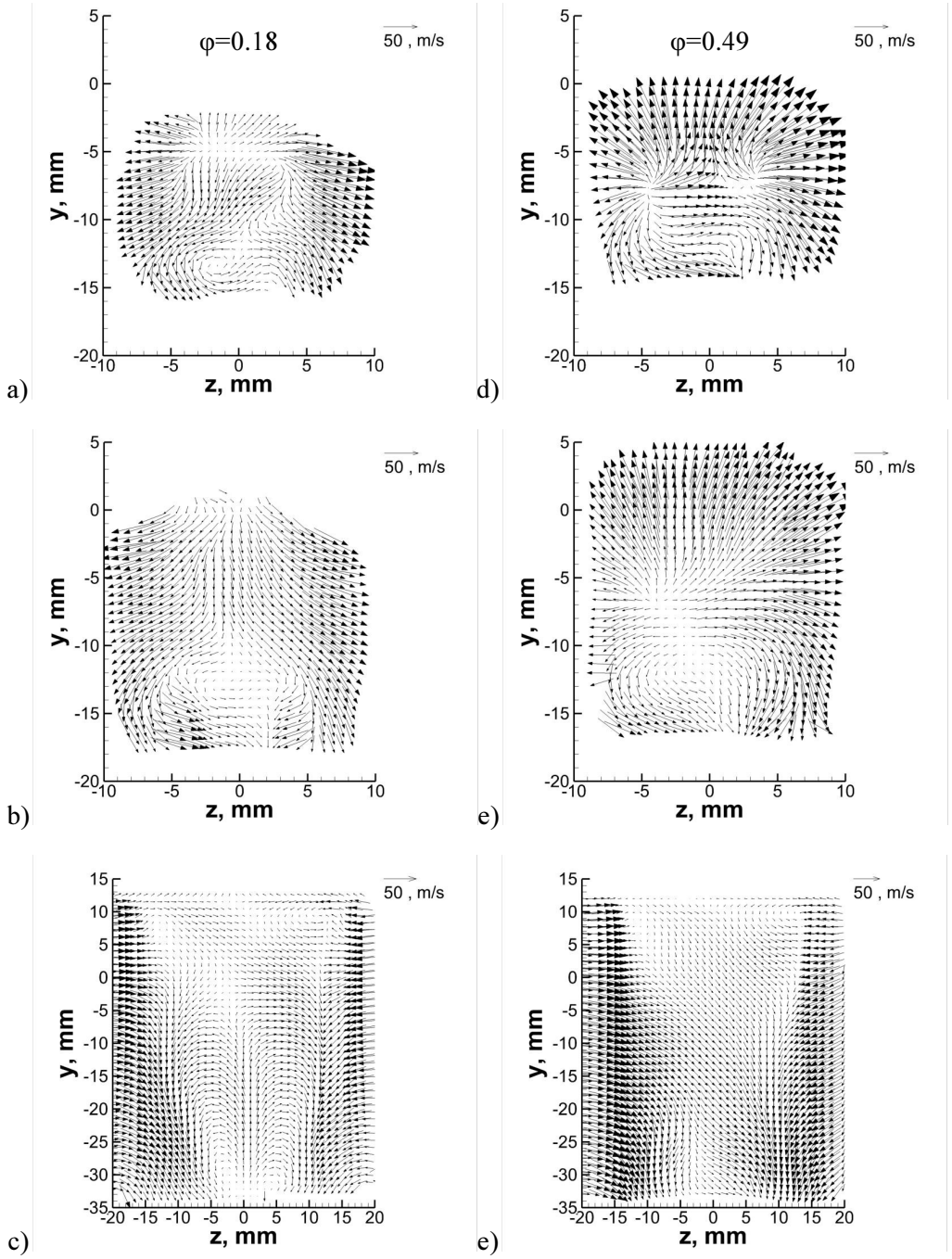

Fig. 6.6: Mean in-plane velocity vectors (V and W vectors): a) x/H=6, φ=0.18, b) x/H=12, φ =0.18, c) x/H=82, φ =0.18, d) x/H=6, φ =0.49, e) x/H=12, φ =0.49, f) x/H=82, φ =0.49

To highlight regions with large rotational motion, the mean vorticity in the axial direction, is presented in Fig. 6.7. As expected, for all axial locations and equivalence ratios, the peak values of vorticity are centered on the ramp induced vortices. Again, it

can be seen that the left vortex is slightly stronger supported by higher vorticity values. At x/H=6, for both equivalence ratios, there exists a smaller secondary region of rotation above the primary vortices that is rotating in the opposite direction. The primary regions of rotation have spread out significantly by x/H=12 for both equivalence ratios. Again, at x/H=82 the evidence of the large elongated (in the y-direction) vortices is shown in Fig. 6.7c. In contrast the vortices at x/H=82 for the φ=0.49 case are small are remain close to the fuel injection wall. Strong corner vortices are also evident at the exit plane for both equivalence ratios. There is no evidence of significantly different vorticity levels at corresponding measurement planes for the ramjet mode vs. the scramjet mode of operation. As the axial distance downstream of fuel injection increases, the vorticity values decrease for both modes of operation.

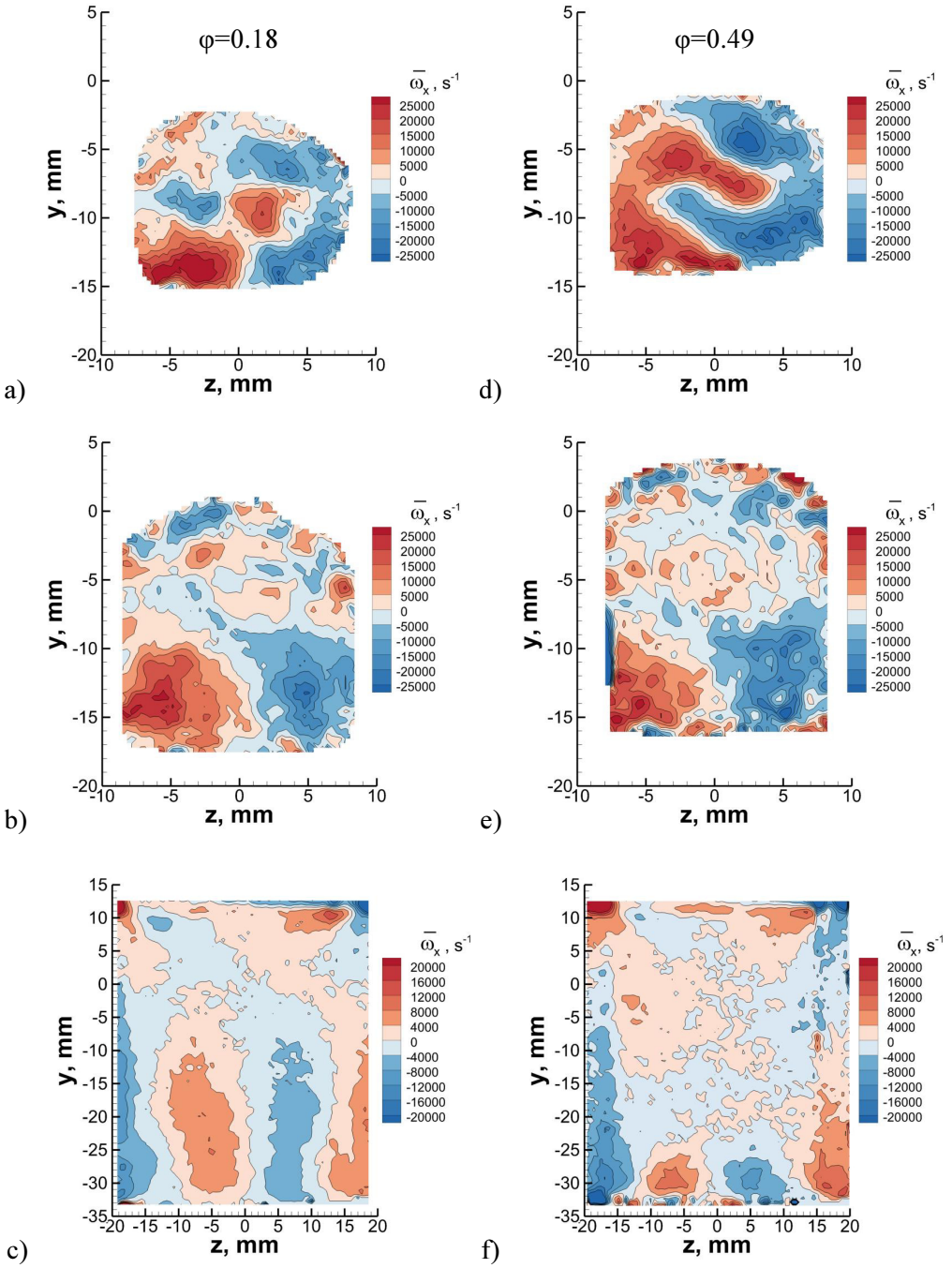

Fig. 6.7: Mean vorticity: a) x/H=6, φ=0.18, b) x/H=12, φ =0.18, c) x/H=82, φ =0.18, d) x/H=6, φ =0.49, e) x/H=12, φ =0.49, f) x/H=82, φ =0.49

Turbulent kinetic energy, defined in Eqn. 6.6, is a measure of the turbulent fluctuations in velocity in all directions. Contour plots of TKE are presented in Fig. 6.8 at the three measurement planes for both fuel equivalence ratios. At x/H=6 and φ=0.18 (Fig.

6.8a) there are two maximum regions of TKE which correspond to the lobes in the velocity magnitude contour (Fig 6.4a) where there exists a shear layer between the low-speed and high-speed velocities. There exists a sharp velocity gradient at this location in the axial direction causing high shear and elevated levels of turbulence. The trend is continued for the φ=0.18 case as the axial location moves downstream where peak TKE levels are concentrated in the shear layer between the combusting core and freestream velocities. At x/H=82 and φ=0.18 the elongated vortices influence the U-shape of the velocity magnitude (Fig. 6.4c) and the location and direction of the shear layer has been altered. It can be seen for this case that the peak TKE levels are located in regions of high shear and vorticity. For the φ=049 case at x/h=6 and 12, the peak levels of TKE occur in the region between the high-speed jet core and the fuel injector wall. Again, this location corresponds to the sharpest velocity gradient and the highest fluctuating velocities associated with the fuel jet. At x/H=82 and φ=.049 the turbulent fluctuations are concentrated to a small region near the combustor wall in the region of highest vorticity.

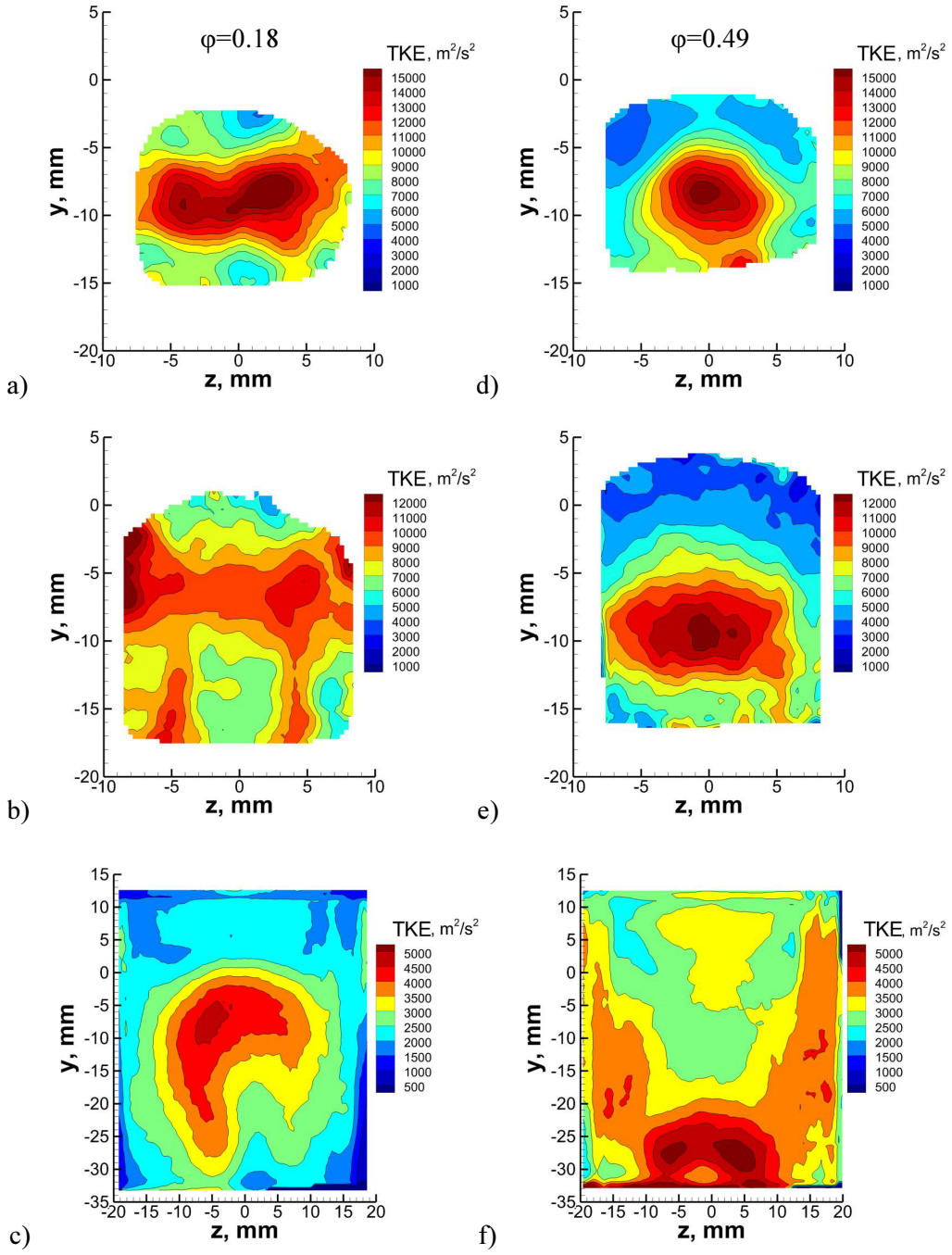

Fig. 6.8: Turbulent kinetic energy (TKE): a) x/H=6, φ=0.18, b) x/H=12, φ =0.18, c) x/H=82, φ =0.18, d) x/H=6, φ =0.49, e) x/H=12, φ =0.49, f) x/H=82, φ =0.49

6.1.2 Turbulent Length Scales

The turbulent length scales were calculated based on the space-time velocity autocorrelation function which takes the form of Eq. 6.7 [77]:

$$R_{ii}(x,r,t) = \frac{\overline{u_\iota'(x,t)u_\iota'(x+r,t)}}{\overline{u_\iota'(x,t)u_\iota'(x,t)}} \tag{6.7}$$

where i is the Cartesian direction (x, y, or z), and u' is the fluctuating velocity component defined as the difference between instantaneous velocity, U, and mean velocity, Ū. The velocity correlation function is normalized by the value at the specified point (zero radius r=0) and ranges in value from 0 to 1. The function quantifies how one point in the flow is correlated with all other points located some distance r away from the point of interest. The integral length scale, Eq. 6.8, was calculated by integrating the velocity autocorrelation function from 0 to infinity along the principal direction of the velocity component.

$$L_{ii} = \int_0^\infty R_{ii}(x,r,t)dr_i \tag{6.8}$$

Therefore, the v' velocity component is integrated along the y-axis and the w' velocity component is integrated along the z-axis. The integral length scale is a measure of the largest turbulent eddies which contribute most of the transport of momentum and energy. The point of interest (0, -11) was chosen to be investigated at all measurement planes and both fuel equivalence ratios. Fig. 6.9 presents the space correlation function at the point of interest for the v' velocity component and Fig. 6.10 presents the space correlation function for the w' velocity component. The contour levels range from 0.2 to 0.9.

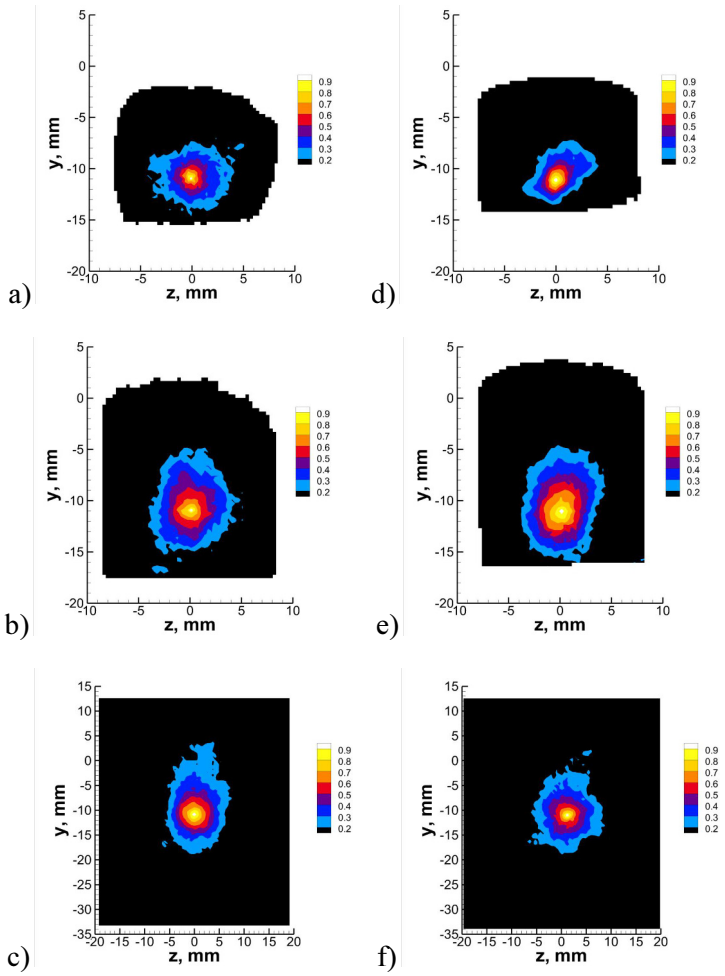

Figure 6.9: Contours of the space correlation function R_{yy} at (0,-11): a) x/H=6, φ=0.18, b) x/H=12, φ=0.18, c) x/H=82, φ=0.18, d) x/H=6, φ=0.49, e) x/H=12, φ=0.49, f) x/H=82, φ=0.49

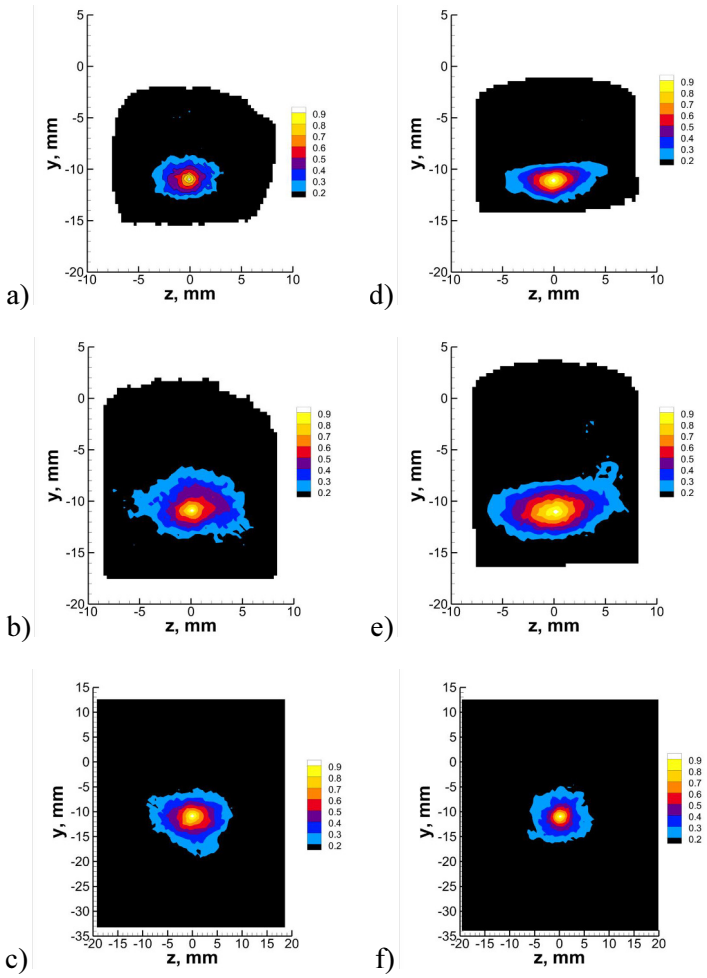

Figure 6.10: Contours of the space correlation function R_{zz} at (0,-11): a) x/H=6, φ=0.18, b) x/H=12, φ=0.18, c) x/H=82, φ=0.18, d) x/H=6, φ=0.49, e) x/H=12, φ=0.49, f) x/H=82, φ=0.49

Note that at x/H=82 in Fig. 6.9 and Fig. 6.10 the axes are on a different scale. The space correlation function by definition takes on the value of unity at the point (0, -11) and decreases radially outward. The space correlation function is fairly symmetric for most planes but is slightly elongated along the direction of the v' velocity component in Fig. 6.9 and w' velocity component in Fig. 6.10. This is typical and has been observed in several studies of subsonic and supersonic jet flows [76, 78, 79, 80]. In order to integrate the correlation function, line plots starting at the point of interest are taken in the y-

direction for R_{yy} and z-direction for R_{zz}. The line plots of the space correlation function are given in Fig. 6.11.

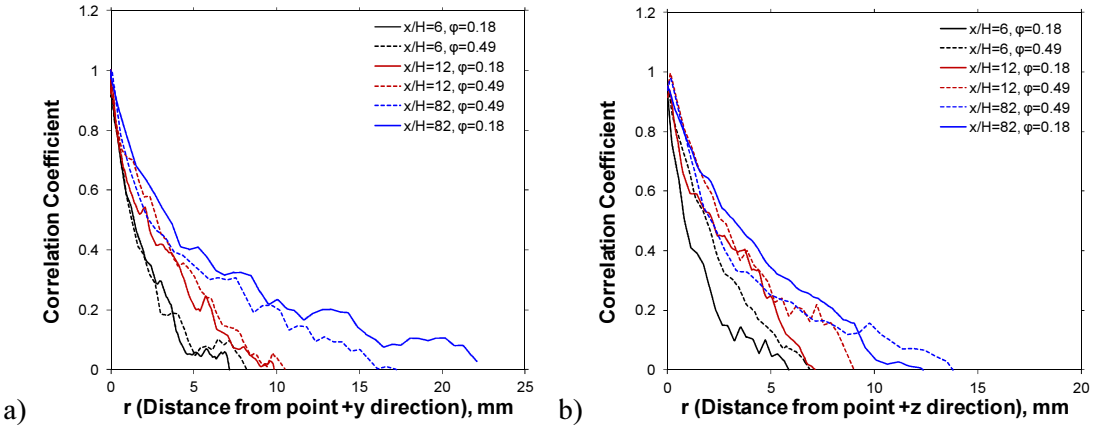

Figure 6.11: Radial distribution of the space correlation functions R_{zz} and R_{yy} at (0,-11): a) R_{yy}, b) R_{zz}

The correlation function is integrated from r=0 until the point at which the correlation falls below zero instead of the theoretical integration to infinity as defined in Eq. 6.8. Numerical integration was performed with the trapezoid method with 1000 evenly discretized grid points with spacing equal to 0.014 mm. It is evident from Fig. 6.11 that there exists a trend in the broadening of the correlation function as the axial location is increased. At a given measurement plane location the correlation coefficients are self-similar. Overall the v' component of velocity exhibits a higher degree of correlation at a further r distance. The results of integration and subsequent calculation of the integral length scale L_{yy} and L_{zz} is presented in Fig. 6.12.

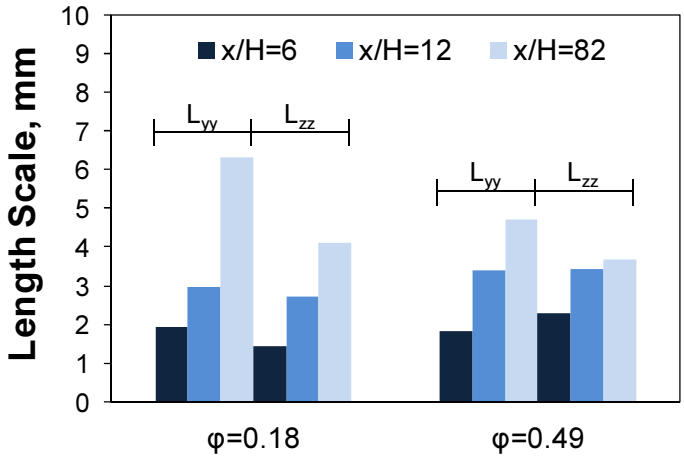

Figure 6.12: Correlation integral length scales L_{yy} and L_{zz} at (0, -11) at x/H=6, 12, 82 and φ=0.18 and 0.49.

The integral length scales L_{yy} and L_{zz} both increase as the axial location increases. This means that the integral length scales near the fuel injector are small, fast, and intense whereas the mixing length scales have stretched or elongated further down in the flowpath. Since the duct is diverging, the domain length scale increases as the location downstream of fuel injection increases and therefore leads to an increase in Reynolds number. An increase in integral length scale could be in part due to an increasing Reynolds number since the integral length scale is proportional to $Re^{3/4}$. The integral length scales are the largest at x/H=82 and φ=0.18 which is supported by the large elongated vortices present in that plane.

6.1.2 Conclusions

The results presented herein are the first reported SPIV measurements conducted during ramjet mode and scramjet mode of operation within a DMSJ model combustor. The results presented give a sample of the derived quantities that can be extracted from the instantaneous velocity data. All other velocity contour data is available in the

Appendix. The measured velocity fields reveal information that was not previously accessible. The influence of the ramp-induced vortices is clearly the key feature of this flowfield. It can be seen that the vortices are the strongest near the fuel injector at x/H=6 and persist all the way until the exit, but to a lesser degree. In addition, the turbulent kinetic energy is the greatest near the fuel injector at x/H=6. The turbulent kinetic energy is slightly reduced at x/H=12 and the turbulent fluctuations are limited at the exit plane. Overall, both vorticity and TKE decrease as the axial dimension increases. The difference between modes of combustion is clear from the velocity distribution. The scramjet mode of operation is characterized by a small low-speed region near the combustor wall with the flow velocity increasing quickly toward the freestream. Alternatively, the ramjet mode of combustion is dominated by a high-speed jet core as a result of increased fuel pressures surrounded by low speed flow caused by deceleration of the shock train. Both modes of combustion produce similar degrees of vorticity at comparable planes despite the largely different incoming flow. There does not appear to be a clear difference in TKE peak levels between the different combustion modes. Rather, the location of the peak TKE levels at a particular plane is determined by the location of the shear layer in the axial velocity component. The results provide an extensive set of reacting velocity data for the use of computational model validation being conducted within the NCHCCP [82]. Chapter 7 follows with comparisons of the SPIV measurements with CFD and independent TDLAS velocity measurements.

Chapter 7

SPIV Comparisons with CFD and TDLAS

Chapter 7 is dedicated to comparing the experimental results obtained with SPIV to concurrent CFD modeling and independent velocity measurements acquired by Tunable Diode Laser Absorption Spectroscopy (TDLAS) that were performed within the National Center for Hypersonic Combined Cycle Propulsion. First, the SPIV measurements are compared to the CFD at three planes in the DMSJ flowpath for both modes of operation. Both qualitative and quantitative comparisons are examined. Experimental data is critical for the purposes of assessing the capability of the predictive model. The SPIV measurements are useful for comparing all three components of mean velocity as well as turbulent fluctuations. In addition, the SPIV measurements were conducted during both the ramjet and scramjet mode of operation and can address the performance of the CFD during both modes. Next, the SPIV measured U-component of mean velocity will be compared to TDLAS measurements of water molecule Doppler shift at x/H=6 and x/H=12 for the φ=0.18 case.

7.1 SPIV Comparisons with CFD, x/H=6, 12, 82 (φ=0.18 and 0.49)

In this section, SPIV measurements are compared with CFD simulations performed by Jesse Fulton and Jack Edwards at N.C. State University. The CFD simulations employ a hybrid LES/RANS method. The time averaged RANS method was performed in regions of the flow such as the boundary layer and acts as a "form of near-wall closure [82]." The main core of the flow was predicted using the LES method which resolves

large scale turbulent motions and effectively spatially filters the Navier-Stokes equations. Since only large-scale turbulent structures are resolved for this method, it is necessary to model the sub-grid scale turbulence. The solver developed at N.C. State University is named REACTMB and solves the three-dimensional compressible reactive Navier-Stokes equations using finite-volume methods. The reaction mechanism utilized in the simulations was provided by Burke [83]. Typically the Jachimowski model was used by the researchers but there was difficulty maintaining a stable flame attached to the ramp fuel injector. The Burke mechanism tends to predict higher reaction rates and heat release and therefore provided a better environment for the stable flame. Both the nozzle exit flow and fuel injector exit flow were solved previously and used as the inflow to the isolator and fuel injector exit. It should be noted that the CFD simulations included an asymmetric temperature distribution at the entrance to the combustor section which was measured by CARS [37, 39]. The mesh in the combustor section of the flowpath contains approximately 33 million cells. To ensure convergence, the time averaged CFD results are calculated by averaging over 5 flow-though times defined as the time for a molecule or particle to travel from the inflow plane to the exit. The quantities being compared are mean velocity magnitude and RMS velocity magnitude defined by Eq. 7.1 and 7.2.

$$|\bar{V}| = \sqrt{\bar{U}^2 + \bar{V}^2 + \bar{W}^2} \tag{7.1}$$

$$|v| = \sqrt{\overline{u'}^2 + \overline{v'}^2 + \overline{w'}^2} \tag{7.2}$$

The total velocity magnitude is convenient for comparison purposes because it takes into account all three velocity components. For qualitative comparison, mean velocity magnitude and RMS velocity magnitude are presented in Figs. 7.1, 7.3, 7.5, and 7.7. In Figs. 7.1, 7.3, 7.5, and 7.7 the SPIV measurements are located to the left of the

corresponding CFD calculations and the measurement plane location moves increasingly downstream from top to bottom.

Figure 7.1 presents the qualitative comparison of mean velocity magnitude for the φ=0.18 case. The CFD distributions have been masked such that the same measurement areas are presented. Note the experimental uncertainty in mean velocity magnitude of approximately 24 m/s. At x/H=6 and φ=0.18, both the SPIV and CFD show a kidney-shaped low momentum region of the flow close to the fuel injection wall. The CFD predicts significantly lower speeds near the wall due to heat release and separation of the flow over the ramp fuel injector. This is consistent with the choice of reaction mechanism which has shown to predict more heat release than experimentally measured. In addition, the CFD predicts higher velocities toward the edge of the fuel plume and there is stronger influence of the fuel jet. By x/H=12 and x/H=82 there is excellent agreement between the SPIV and CFD. The same U-shaped velocity contour is evident and the sharp velocity gradient in the shear layer is well matched. At x/H=12 the CFD again over-predicts the freestream velocities but to a much lesser extent. Not only do the magnitudes agree to a high level but the locations of the flow features are consistent.

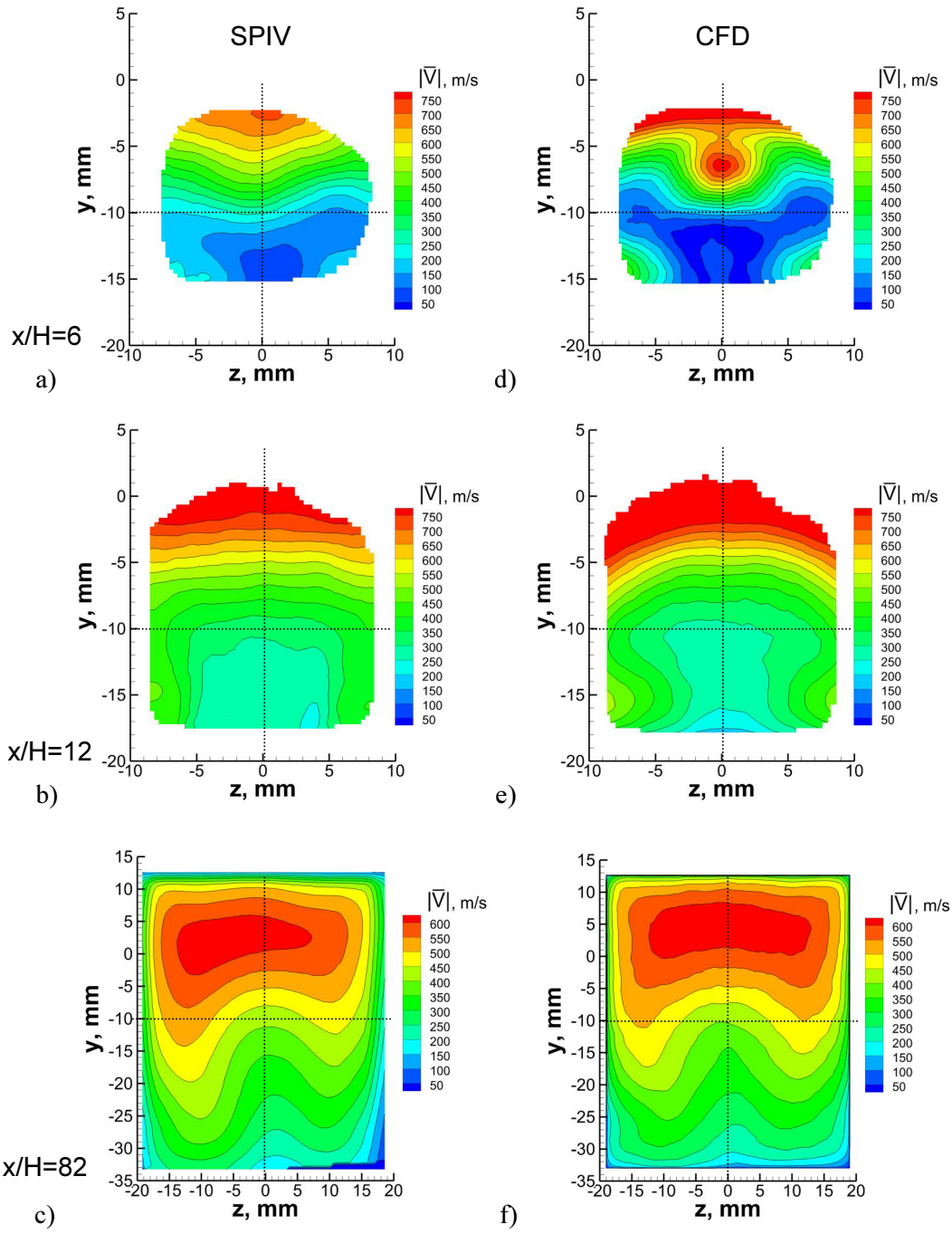

Figure 7.1: Contour comparison of SPIV and CFD Velocity Magnitude, $|\bar{V}|$, φ=0.18: a) SPIV, x/H=6, b) SPIV, x/H=12, c) SPIV, x/H=82, d) CFD, x/H=6, e) CFD, x/H=12, f) CFD, x/H=82 [Experimental uncertainty = ~24 m/s].

In order to gain a more quantitative understanding of the comparisons, a vertical line profile centered at z=0 mm and a horizontal line profile centered at y=-10 mm is presented in Fig. 7.2. The vertical line centered at z=0 mm corresponds to a line of

physical symmetry in the flowpath and the horizontal line centered at y=-10 mm is located approximately in the middle of the mixing/combusting plume where elevated regions of TKE exist.

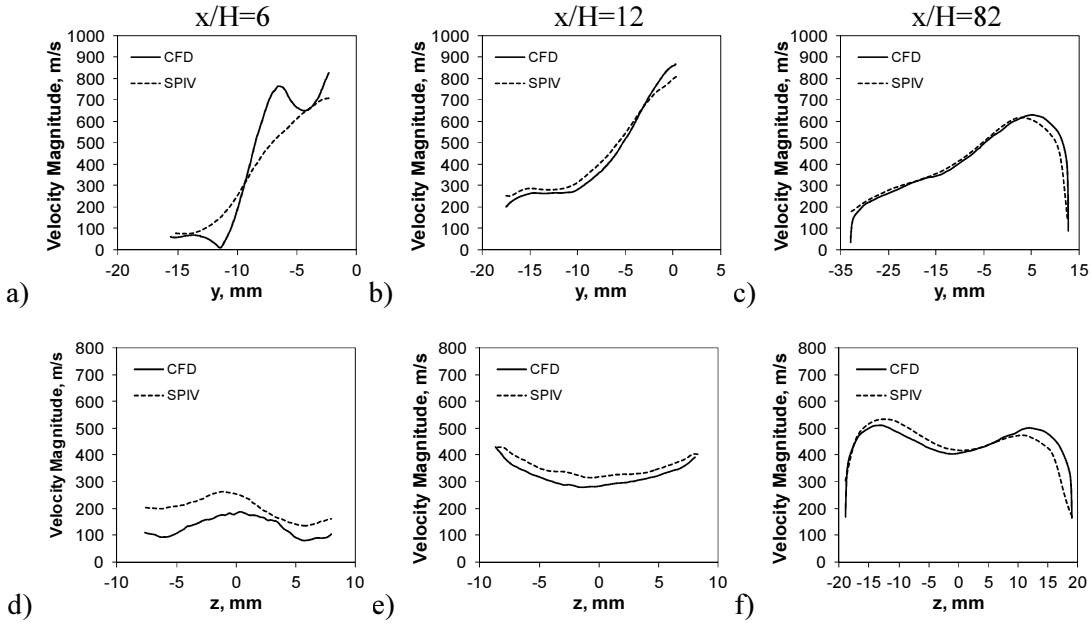

Figure 7.2: SPIV and CFD line comparisons, mean velocity magnitude, $|\bar{V}|$, φ=0.18 ,Vertical line through z=0 mm, horizontal line through y=-11 mm: a) Vertical line, x/H=6, b) Vertical line, x/H=12, c) Vertical line, x/H=82, d) horizontal line, x/H=6, e) horizontal line, x/H=12, f) horizontal line, x/H=82.

Fig. 7.2a shows that the CFD predicts more structure and higher velocity gradients than the SPIV measured at x/h=6 and φ=0.18. The end points at y=-16 mm and y=-2 mm match with a smooth transition measured by the SPIV as opposed to the sharp gradient predicted by the CFD. The maximum difference for this plane and fuel equivalence ratio is approximately 200 m/s. It is clear that the agreement significantly improved for the downstream locations at x/H=12 and x/H=82. This same trend of increased agreement further away from the point of fuel injection has been observed by independent CARS measurements of temperature and species (H_2, N_2, and O_2) concentration on Config. C [37, 39]. This could be a factor of the Burke reaction mechanism utilized by the CFD where the combustion efficiency may differ from reality. It has been reported by Fulton

et al. that the Burke mechanism when, compared to the Jachimowski mechanism, is more reactive and predicts higher heat release. This implies that the CFD model will predict higher temperatures and combustion product species concentrations at a given measurement plane. These trends are verified by CARS measurements. The increased heat release predicted by the model would result in more separation of the flow and therefore deceleration. This is observed in Fig. 7.2 in which the measured SPIV velocity magnitude is typically higher than the CFD. At x/H=12 and x/H=82 there is excellent agreement between the measurements and calculations with maximum differences of approximately 65 m/s and 100 m/s respectively. The velocity gradients are also matched extremely well at x/H=12 and x/H=82.

The RMS velocity magnitude, equal to the square root of turbulent kinetic energy, for φ=0.18 is presented in Fig. 7.3. Overall there is less agreement of the fluctuating velocity components than was observed the mean velocity field between SPIV and CFD.

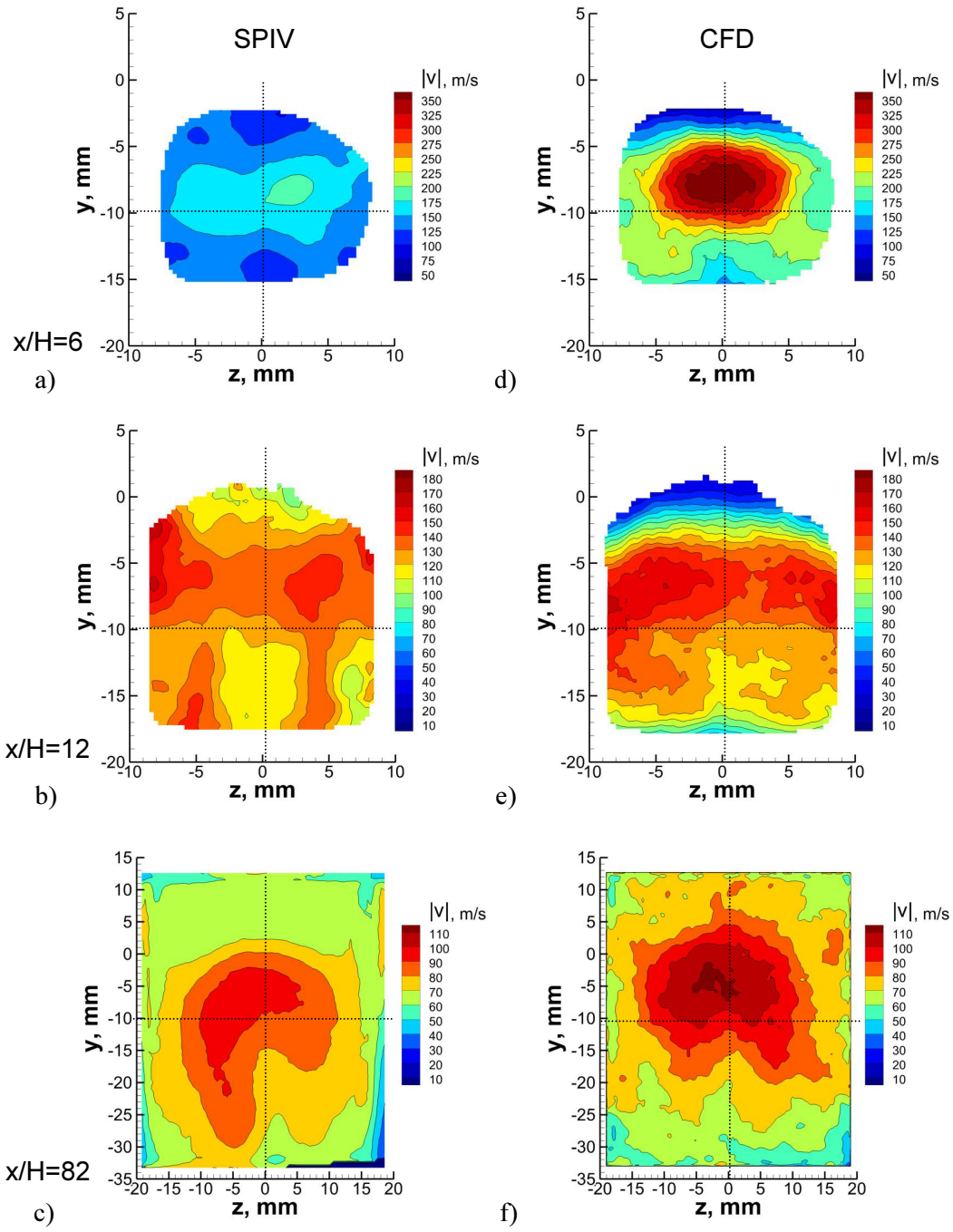

Figure 7.3: Contour comparison of SPIV and CFD RMS Velocity Magnitude, $|v|$, φ=0.18: a) SPIV, x/H=6, b) SPIV, x/H=12, c) SPIV, x/H=82, d) CFD, x/H=6, e) CFD, x/H=12, f) CFD, x/H=82.

This disagreement with CFD and over-prediction of RMS velocity has been observed for previous SPIV measurements conducted on the Configuration A flowpath [84] and for CARS measurements of temperature and species mole fractions on the current flowpath

(Configuration C) [37]. There exists consistent disagreement between the CFD and the experiment results (both SPIV and CARS) particularly at the x/H=6 plane with much more reasonable agreement at the downstream planes. For example, the RMS of temperature, H_2 mole fraction, and O_2 mole fraction, as measured by CARS are all approximately half that predicted by CFD at x/H=6. The discrepancy in temperature, H_2, and O_2 concentration standard deviations could be primarily due to the over-reactive mechanism utilized by the CFD. This is due to the fact that oxygen and hydrogen are both reactive species and are therefore affected by the chemistry model. In order to isolate from the effect of combustion, the fluctuations in N_2 can be examined because the molecule is inert. Therefore the N_2 acts as a tracer of non-reacting fluid and the RMS of N_2 concentration will be a result of turbulent velocity fluctuations. Again, the CFD predicts RMS of N_2 concentration two times higher than the measurement. In reference to Fig. 7.3(a)/(d), the RMS velocity magnitude measured by SPIV is roughly half of that predicted by CFD. Since the same trend of over-predicted RMS is observed, it is more likely that the discrepancy in RMS velocity is due to the LES method, rather than the reaction mechanism.

Since only the largest eddies were simulated in this region of the flow the sub-grid scale must be modeled. Under-estimation of the sub-grid scales which are predominantly dissipative could lead to higher predicted turbulent intensity by the CFD. Turbulent statistics are highly dependent on the length and time scales and therefore could be contributing to higher uncertainties at this location. Thus the LES method is predicting larger turbulent eddies, containing more energy than is measured by SPIV at x/H=6. A potential source for this over-predicted TKE is how the inflow turbulence intensity is

modeled by the CFD. In addition, the PIV method is limited to a particular range of turbulent frequencies (~25 kHz) due to particle response time. If the CFD is predicting higher turbulent frequencies than can be measured by SPIV this could lead to some of the differences shown. However, this is unlikely, because the CARS measurements show the same trend and do not suffer from particle lag issues since they are measuring spectroscopic properties of molecules. At x/H=12 and x/H=82 the CFD turbulence levels agree with the SPIV to a much higher degree. The location of the peak turbulence intensity occurs in the same location, where the shear layer between the low-speed and high-speed flows meet.

Fig. 7.4 shows the same vertical and horizontal line profiles seen in Fig. 7.2 but for RMS velocity magnitude. It is again see that the CFD over-predicts the turbulent fluctuations at x/H=6 by a factor of 2. In the near-field, close to fuel injection, the turbulent structures will be both smaller and faster, as compared to further in the duct where dissipation will occur due to decay of turbulent kinetic energy away from the fuel injector. It has been shown by the SPIV measurements that the highest TKE occurs at x/H=6 and has significantly decreased by x/H=82. Therefore, both the CFD and PIV show better agreement as the length scales increase further axially in the duct. At x/H=12 and x/H=82 the turbulence has dissipated significantly and the CFD matches the SPIV extremely well.

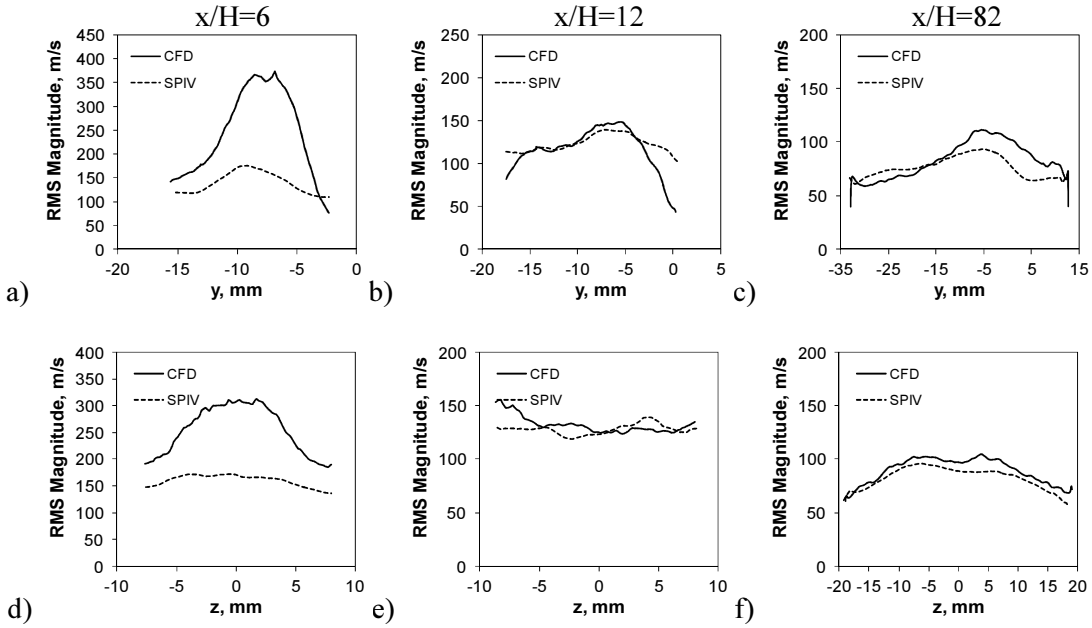

Figure 7.4: SPIV and CFD line comparisons, RMS velocity magnitude, $|v|$, φ=0.18 Vertical line through z=0 mm, horizontal line through y=-11 mm: a) Vertical line, x/H=6, b) Vertical line, x/H=12, c) Vertical line,

Fig. 7.5 presents the contour plots of mean velocity magnitude at φ=0.49 with the SPIV measurements on the left and CFD calculations on the right.

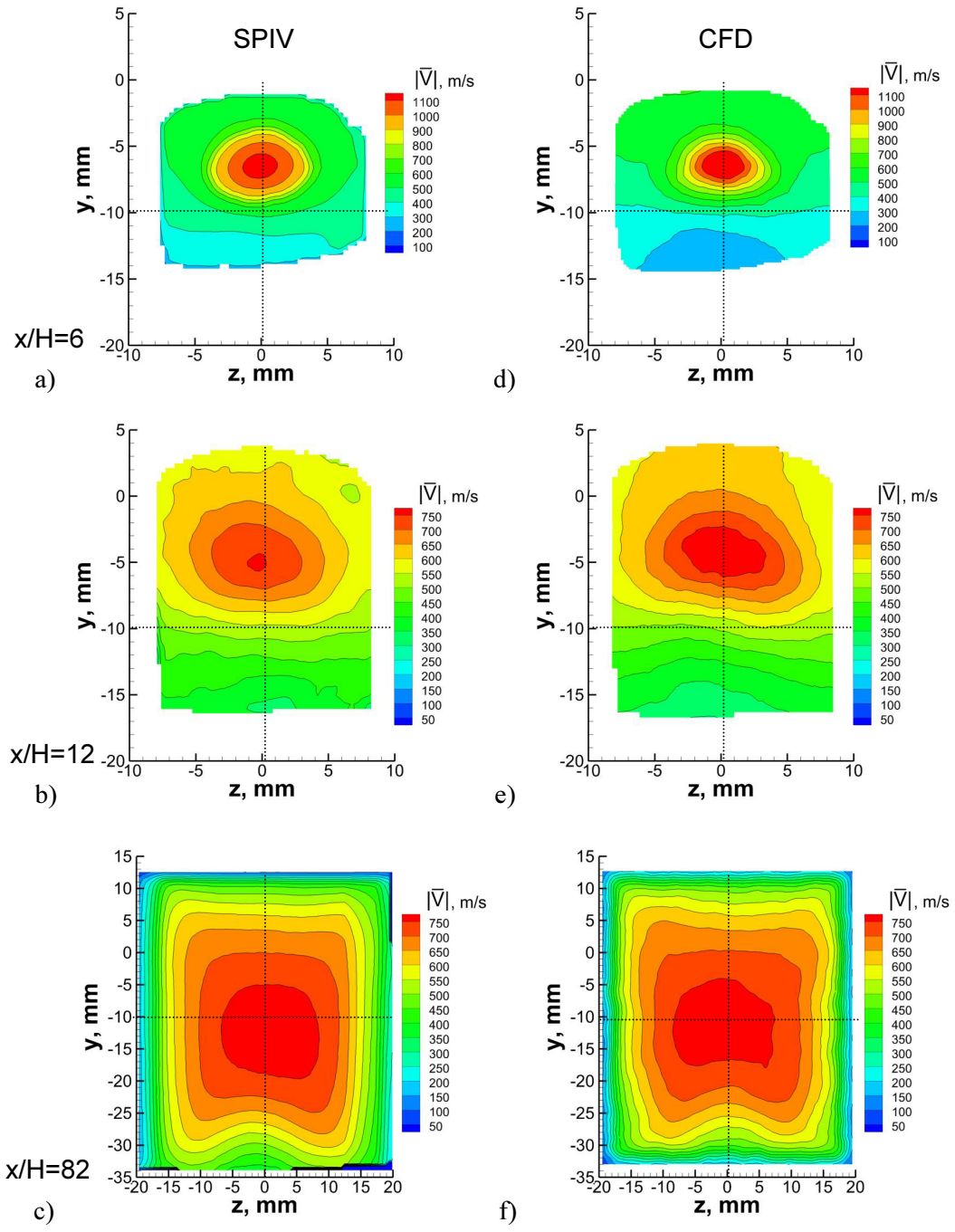

Figure 7.5: Comparison of SPIV and CFD Velocity Magnitude, $|\bar{V}|$, φ=0.49: a) SPIV, x/H=6, b) SPIV, x/H=12, c) SPIV, x/H=82, d) CFD, x/H=6, e) CFD, x/H=12, f) CFD, x/H=82.

The measurement plane locations of x/H=6, 12, and 82 increase from left to right. The velocity field at x/H=6 shows the high-speed fuel jet which is captured by both the measurement and computation. The CFD predicts a slightly higher peak fuel jet velocity

of ~1200 m/s whereas the SPIV measures peak velocity magnitude of ~1100 m/s. The size and location of the fuel jet matches very well. At the downstream locations x/H=12 and x/H=82 there is significantly better agreement between SPIV and CFD. This same trend holds consistent as for the φ=0.18 case. Again the CFD performs proficiently at predicting the velocity magnitudes, location of flow structures, and velocity gradients.

Fig. 7.6 shows quantitative line profiles in a vertical direction through z=0 mm and in a horizontal direction through y=-10 mm. Overall, there exists better agreement between SPIV and CFD for the φ=0.49 case than for the φ=0.18 case. The SPIV measures higher velocities across much of the plume for the φ=0.18 case at x/H=6.

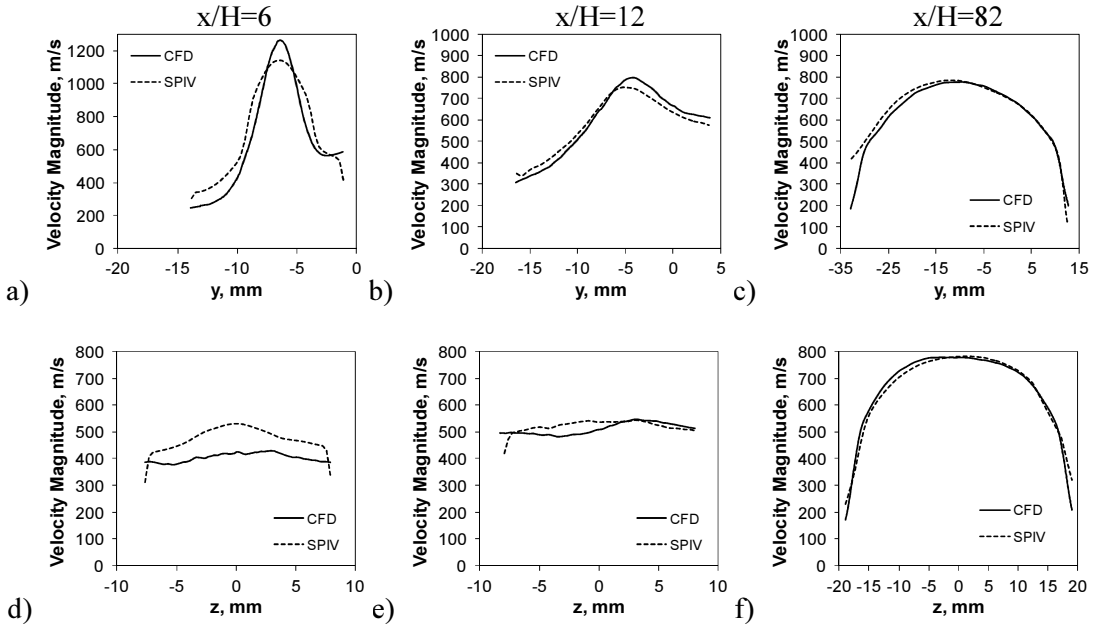

Figure 7.6: SPIV and CFD line comparisons, mean velocity magnitude, $|\bar{V}|$, φ=0.49, Vertical line through z=0 mm, horizontal line through y=-11 mm: a) Vertical line, x/H=6, b) Vertical line, x/H=12, c) Vertical line, x/H=82, d) horizontal line, x/H=6, e) horizontal line, x/H=12, f) horizontal line, x/H=82.

At x/H=6 there is a maximum difference of approximately 100 m/s. At x/H=12 and x/H=82 the maximum difference is approximately 50 m/s and 30 m/s, excluding the large difference towards the edge of the plume. This discrepancy is significant when considering the experimental uncertainly of 24 m/s in velocity magnitude.

For the φ=0.49 fuel equivalence ratio case (Fig. 7.7/7.8), there was no available turbulent statistics at x/H=82 for the CFD and thus no comparison can be made. The researchers (Edwards and Fulton) do not save all quantities for each CFD run and unfortunately were conducted before the SPIV measurements. At x/H=6 the CFD again over-predict the turbulent fluctuations of a factor of approximately 2. At x/H=12, the turbulence intensity has decreased significantly and there exists much better agreement; the CFD over-predicted the turbulent kinetic energy at this measurement plane by a factor of approximately 1.3. Despite the difference in magnitude of the velocity fluctuations, the location of peak turbulence is well matched. The shape of the RMS velocity magnitude is circular and is located in the shear layer between the fuel jet and combustor wall.

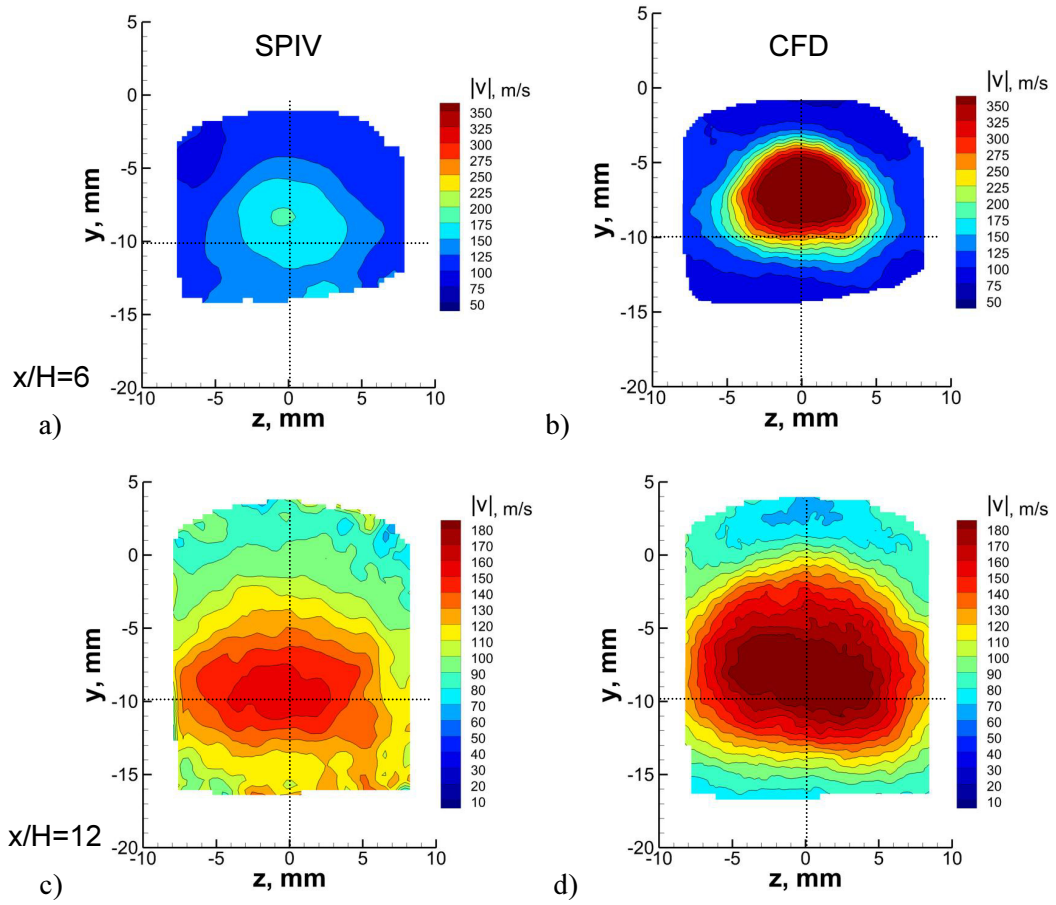

Figure 7.7: Comparison of SPIV and CFD RMS Velocity Magnitude, $|v|$, φ=0.49: a) SPIV, x/H=6, b) SPIV, x/H=12, c) CFD, x/H=6, d) CFD, x/H=12.

The same vertical line profiles at z=0 mm and horizontal line profile at y=-10 mm are presented in Fig. 7.8. Similar shapes and trends are observed as were seen for the φ=0.18 case. Compared to the φ=0.18, case there is significantly less agreement between the SPIV and CFD for turbulent velocity fluctuations. The turbulence is not captured well at x/H=6 and moderate agreement is seen at x/H=12. For the φ=0.18, case the maximum difference between SPIV and CFD was approximately 25 m^2/s^2 whereas for the φ=0.49 case the maximum difference is approximately 50 m^2/s^2 at x/H=12. This could be in part due to the influence of the turbulent fuel jet which penetrates further for the φ=0.49 case.

This is likely due to the higher fuel pressure and thus more influence of the nearfield velocity fluctuations predicted by CFD.

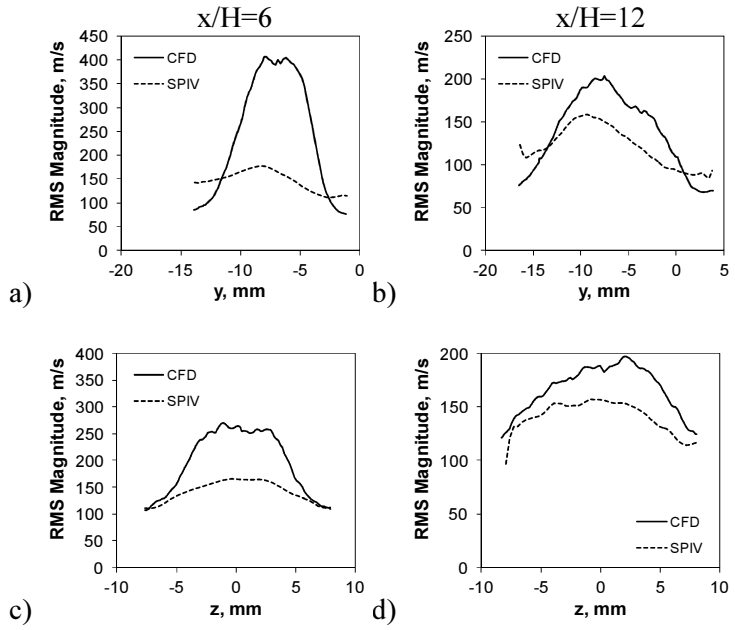

Figure 7.8: SPIV and CFD line comparisons, RMS velocity magnitude, $|v|$, φ=0.49 Vertical line through z=0 mm, horizontal line through y=-11 mm: a) vertical line, x/H=6, b) vertical line, x/H=12, c) horizontal line, x/H=6, d) horizontal line, x/H=12.

In order to quantify the level of agreement or disagreement, the percent difference between SPIV and CFD was calculated over the entire measurement region. It was first necessary to interpolate the CFD results to the same grid as the SPIV in order to allow for subtraction of the fields. The percent difference of any velocity derived variable, β, between SPIV and CFD is defined as:

$$\delta = 100 \times \frac{\sum_{k=1}^{N} |\beta_{k,SPIV} - \beta_{k,CFD}|}{\sum_{k=1}^{N} \beta_{k,SPIV}} \tag{7.3}$$

This calculation was performed for the mean velocity magnitude distribution, $|\bar{V}|$, and the results are presented in Fig. 7.9 with experimental error bars.

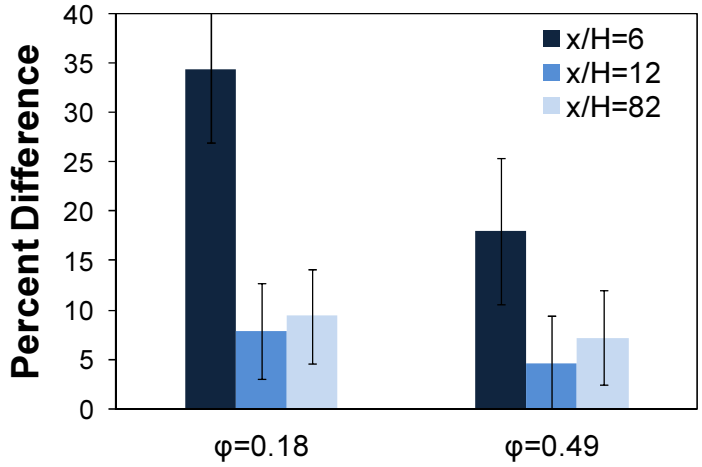

Figure 7.9: SPIV vs. CFD percent difference bar chart.

Overall, the agreement between SPIV and CFD is the worst at x/H=6. The percent difference is slightly lower at x/H=12 compared to x/H=82, but there is excellent agreement (below 10%) for both planes. At the x/H=6 measurement plane location, the high phi case, φ=0.49, has better overall agreement than the low phi case, φ=0.18. Alternatively, at x/H=12 and downstream in the farfield, the CFD has the same predictive capability of modeling both the ramjet and scramjet mode of operation. There should be some efforts to address the shortcomings in both mean velocity and turbulence intensity in the nearfield. Despite the moderate agreement at x/H=6, the CFD model developed by Fulton and Edwards has proved to be a very capable model for predicting several measured flow quantities within the NCHCCP. Going forward, the computational model will be very useful for predicting trends in flow properties as inputs are varied such as fuel equivalence ratio.

7.2 SPIV Comparison to TDLAS at x/H=6 and x/H=12 (φ=0.18)

As part of the collaboration within the NCHCCP, researchers at Stanford University conducted tunable diode laser absorption spectroscopy (TDLAS) measurements of axial velocity within the UVaSCF for Config. C [85]. The measurements were conducted at x/H=6 and x/H=12 for the scramjet mode of operation at φ=0.18. The measurements are path integrated due to the line-of-sight (LOS) nature of the measurement. Two laser beams, at different angles (θ=40°), were directed through the flowpath in the z-direction in order to measure the Doppler shift between the two beams and resolve the integrated axial velocity component at a particular y-location. The angled orientation of the laser beams transmitted through the flow created a spatial average in the axial (x) direction. To assess the spatial averaging a line of sight oriented at 40° was compared to a line of sight perpendicular to the flow (0°) and no significant difference was found. The transmitted beam and collection optics were mounted to a translation stage which allowed the system to traverse in the y-direction, enabling measurement of velocity at several discrete locations. Since the molecule being absorbed by the diode laser in this experiment was water, the measurements are water weighted and cannot be resolved in areas where combustion is not taking place to produce sufficient water. A parallel can be drawn in this sense with the SPIV measurements which were only conducted in the combusting plume region of the flowpath and thus the results have that commonality. In order to compare the measurements, the SPIV results were water-weighted by CARS results and path integrated along the z-direction at the same y-locations as the TDLAS measurements. For a third point of comparison, the CFD data was probed in the same way the TDLAS

measurements were conducted by taking the water number density-weighted average velocity along the LOS.

The comparison of SPIV, TDLAS, and CFD mean axial velocity are presented in Fig. 7.10. TDLAS velocity measurements were not conducted for the ramjet mode (φ=0.49) of operation.

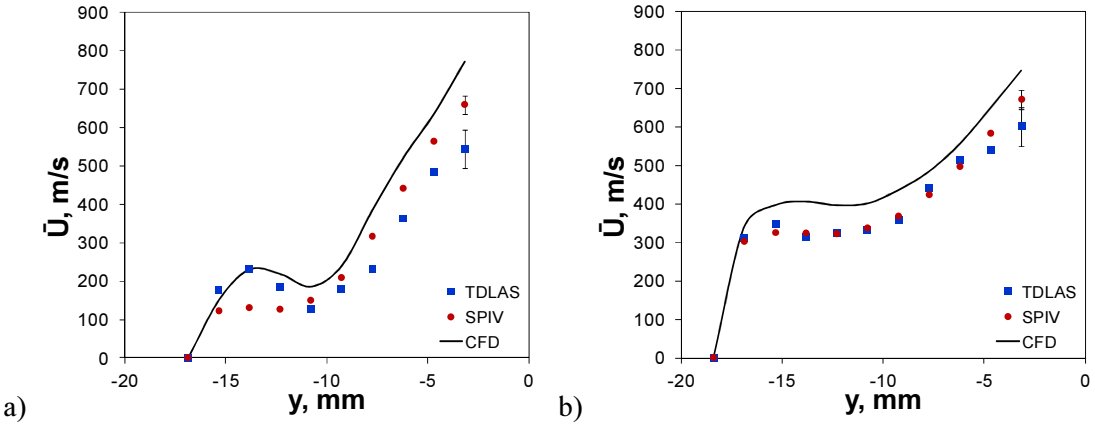

Figure 7.10: Comparison of SPIV, TDLAS, and CFD mean axial velocity at φ=0.18: a) x/H=6, b) x/H=12.

The SPIV measurements are designated by red circles, the TDLAS by blue squares, and the CFD with a black line. Error bars for the SPIV and TDLAS measurements are shown on the last data point in both plots. In Fig. 7.10, the fuel injector wall is located at y=-16.5 mm at x/H=6, and y=-18.4 mm at x/H=12. The results are not presented across the entire duct because there was not sufficient water at these locations to obtain TDLAS measurements. At x/H=6, the same trend in velocity is observed for all three methods. The TDLAS measured the same localized increase and then decrease in velocity as the CFD predicts. The SPIV measured a flat velocity profile in this region. At y=-11 mm the velocity begins to increase steeply and a similar slope is observed for all three methods. There is much greater agreement between CFD and SPIV above y=-11 mm, where the high velocity gradient exists. The TDLAS measurements begin to trail off as the

measurement location moves outward away from the fuel injection wall. A possible explanation for this could be a decreased water vapor concentration towards the freestream. Compared to measurement by both techniques, the CFD over-predicts the mean axial velocity. The SPIV data points tend to lie between the CFD calculations and TDLAS measurements.

At x/H=12, there is excellent agreement between the SPIV and TDLAS velocity to within the uncertainty of the TDLAS measurement. The same trend in axial velocity is observed for all three methods. There is a constant velocity profile between the fuel injection wall and y=-11 mm. As with x/H=6, the velocity begins to increase linearly at y=-11 mm but at a more shallow slope observed at the x/H=12 plane. Again, the CFD tends to over-predict the velocities measured by both SPIV and TDLAS. Comparison of the SPIV measurements and TDLAS measurements, which are an independent velocity measurement, are useful to validate one another and are both shown to support the same trends.

7.3 Conclusions

In summary, there is fair agreement between SPIV and CFD in mean velocity magnitude at x/H=6 for both the φ=0.18 and φ=0.49 case. There is poor agreement in RMS velocity magnitude at x/H=6 for both the φ=0.18 and φ=0.49 case and possible shortcomings in both the CFD and SPIV were examined. The most likely problem with the CFD was the integral length scale filter implemented by the LES simulations that led to over-prediction of turbulence intensity. Despite inaccurate turbulent fluctuations, the CFD performs extremely well at predicting mean quantities. At x/H=12 and 82 for both

fuel equivalence ratios there is excellent agreement for mean velocity magnitude and a significant improvement in RMS velocity magnitude which matches to a high degree. The percent difference between the CFD and SPIV, averaged over the entire measurement area, has been calculated and the results indicate that there is less than 10% difference for x/H=12 and 82 and that overall the φ=0.49 case shows the best agreement. Independent TDLAS axial velocity measurements confirm many of the findings presented by the SPIV at x/H=6 and 12 for the φ=0.18 case.

Chapter 8

Summary and Recommendations

The experimental technique, SPIV, has been applied to a Dual-Mode Scramjet model and measurements were conducted at four planes to meet the objectives of the current research. The first objective, to design DMSJ hardware with extensive optical access for multiple measurement techniques has been accomplished. The hardware design enabled the measurement techniques PIV, PLIF, CARS, TDLAS/T, for measurements of velocity, temperature, and species concentrations. The data set created for the prototypical DMSJ model Configuration C is the largest and most comprehensive experimental data set available to the hypersonic community. State-of-the-art laser based optical measurement techniques enabled the measurement of quantities that have not been reported for DMSJ operation.

The contribution of the current work was the first measurement of 3-component instantaneous velocity at three planes throughout the DMSJ flowpath during the ramjet mode and scramjet mode of operation. The measurements identified the key differences and similarities of the mean vector quantities and turbulent scalars for both modes of combustion. In addition the SPIV measurements can be utilized to calculated combustion efficiency which is described in detail in Ref. [86]. Extensive qualitative and quantitative comparisons of the SPIV measurements have been performed against CFD simulations and TDLAS measurements. Excellent agreement between all three methods was observed for the majority of the measurement locations and fuel conditions. In addition, the current work was the first to measure and quantify the effect of velocity bias associated with

seeding the single-stream ramp fuel injector. The results apply to previous, current, and future measurements and validate the method of seeding.

The modular DMSJ hardware has enabled other relevant studies to be conducted such as a hydrocarbon fueled cavity scramjet flowpath. The same suite of laser-based optical diagnostics have been applied to this new flowpath with varied success. Hydrocarbon flameholders will be relevant to scramjet technology of the future with the goal of burning JP-7 fuels. Looking to the future, the DMSJ hardware has the capability for multiple row fuel injection in both the combustor section and in the isolator section for pre-mixed combustion experiments. This capability broadens the versatility of the UVaSCF and facilitates both fundamental and applied research.

As technology advances, PIV will continue to grow with respect to camera resolution, camera frame rates, and laser repetition rates. For example, the DMSJ hardware presents the opportunity to apply new measurement techniques such as time resolved kHz PIV and PLIF. Higher repetition rates allow a larger turbulent energy spectrum to be examined and the investigation of the small turbulent time scales and large turbulent frequencies. For example time-resolved measurements can capture transient events such as ignition or blow-out. It could also be possible to conduct time-resolved measurements of the transition from ramjet to scramjet mode of combustion. In addition, a volumetric PIV measurement is possible with the use of additional cameras or plenoptics. Particle seeding remains one of the largest challenges for PIV applications. It is the recommendation of the author to investigate new seeding methods and new particle types. These studies are currently under investigation at UVa and may lead to new seeding methods. Several improvements could be made to the current seeder such as a

vortex separator that rejects large particle agglomerations or some other mechanism to break up particles and produce more consistent particle density. There also exist several commercial fluidized bed particle seeders that may be worth the investment. The problem of window fouling remains universal to PIV measurements performed at the UVaSCF. This problem could be mitigated through the use of the newly purchased LaVision kHz rate SPIV system. The possibility of acquiring 1000 images in 1 second may enable seeding of both the fuel stream and freestream where the particles have not been given time to accumulate significantly. This could enable velocity measurements in new sections of the flowpath which have never been examined. This includes the isolator section and the combustor inflow plane which would serve to more accurately define the inflow plane for CFD simulations.

LDV and molecular tagging Velocimetry (MTV) may enable velocity measurements in the freestream that SPIV was unable to attain. This would be beneficial because measurements have never been conducted at the combustor inflow plane. Velocity distributions at the inflow plane could offer critical information for future CFD modeling efforts and aid in defining boundary conditions. For example, if local seeding were possible, LDV would have the capability to measure mean and turbulent velocity. The primary drawback of LDV is that local seeding is only possible in the middle of the duct and therefore measurements could not be taken at all points in the flow. In addition, Femtosecond Laser Electronic Excitation Tagging (FLEET) is capable of imaging flow structures in unseeded air. The FLEET technique works by exciting and dissociating nitrogen molecules with a high-powered focused laser beam. The FLEET technique is capable of measuring multiple components of velocity at a single point in the flow. Since

FLEET does not rely on seeded air, measurements could be conducted at more points in the flow than LDV.

References:

[1] Heiser, W.H, and Pratt, D.T., *Hypersonic Airbreathing Propulsion*, American Institute of Aeronautics, Inc. Washington, D.C., 1994.

[2] Billig. F.S., "Research on Supersonic Combustion." *Journal of Propulsion and Power*, Vol. 6, No. 4, 1993, pp. 499-514.

[3] McDaniel, J.C., Chelliah, H., Goyne, C.P., Edwards, J.R., Givi, P., and Cutler, A.D., "US National Center for Hypersonic Combined Cycle Propulsion: An Overview," AIAA Paper 2009-7280, AIAA/DLR/DGLR International Space Planes and Hypersonic Systems and Technologies Conference, Bremen, Germany, Oct 2009.

[4] Woolf, A.F., "Conventional Prompt Global Strike and Long-Range Ballistic Missiles: Background and Issues," Congressional Research Service Report for Congress, May 5, 2014.

[5] Cockrell, C.E., Auslender, A.H., Guy, R.W., McClinton, C.R., and Welch, S.S., "Technology Roadmad for Dual-Mode Scramjet Propulsion to Support Space-Access Vision Vehicle Development," AIAA Paper 2002-5188.

[6] "X-51 WaveRider Unmanned Scramjet Aircraft, United Stated of America," *Airforce-technology.com*. Retrieved April 9, 2014, from http://www.airforce-technology.com/projects/x51-wave-rider/.

[7] Wall, M. (2013, May), "Air Force's X-51A Hypersonic Scramjet Makes Record-Breaking Final Flight," *Space.com*. Retrieved April 9, 2014, from http://www.space.com/20967-air-force-x-51a-hypersonic-scramjet.html

[8] Covault, C., (2010, May), "Hypersonic X-51 Scramjet to Launch Test Flight in May". *Space.com*, Retrieved April 9, 2014, from http://www.space.com/8428-hypersonic-51-scramjet-launch-test-flight.html

[9] Malik, T., (2012, August), "US Military's Hypersonic X-51A Aircraft Fails Seconds After Launch," *Space.com*, Retrieved April 9, 2014, from http://www.space.com/17132-x-51a-military-hypersonic-plane-test-fails.html.

[10] Cummins., H. Z., Knable, M., and Yeh. Y., "Observation of diffusion broadening of Rayleigh Scattered light." *Physical Review Letters*, Vol. 12. Pp. 150-153, 1964

[11] Adrian, R.J., "Laser Velocimetry", *Fluid Mechanic Measurements*, ed. R. Goldstrein, pp. 155-244, Washington DC: Hemisphere, 1983.

[12] Komine, H., and Brosnan, S., "Instantaneous, Three-component, Dopper Global Velocimetry," *Laser Anemomy*, Vol. 1, pp. 273-277, 1991.

[13] Thurow, B. "MHz Rate Planar Doppler Velocimetry in Supersonic Jets," 42nd AIAA Aerospace Sciences Meeting and Exhibit, Reno, NV, January 2004.

[14] McIntyre, T.J., Houwing, A.F. P., Palma, P.C., Rabbath, P.A.B., and Fox, J.S., "Optical and Pressure Measurements in Shock Tunnel Testing of a Model Scramjet Combustor," *Journal of Propulsion and Power*, Vol. 13, No. 3, 1997, pp. 388-394.

[15] Parker, T. E., Allen, M.G., Reinecke, W. G., Legner, H. H., Foutter, R. R., and Rawlins, W. T., "High-Temperature Supersonic Combustion Testing with Optical Diagnostics," *Journal of Propulsion and Power*, Vol. 9, No. 3, 1993, pp. 486-492.

[16] Donbar, J.M., Gruber, M.R., Jackson, T.A., and Carter, C.D., "OH Planar Laser-Induced Fluorescence Imaging in a Hydrocarbon-Fueled Scramjet Combustor," *Proceedings of the Combustion Institute*, Vol. 28, 2000, pp. 679-687.

[17] Gauba, G., Klavuhn, K.G., McDaniel, J.C., Victor, K.G., Krauss, R.H., and Whitehurst, R.B, "OH Planar Laser-Induced Fluorescence Velocity Measurements in a Supersonic Combustor," *AIAA Journal*, Vol. 35, No. 4, 1997, pp. 678-686.

[18] Molezzi, M.J., and Dutton, J.C., "Application of Particle Image Velocimetry in High-Speed Separated Flows." *AIAA Journal*, Vol. 31, No. 3, 1993.

[19] Weisgerber, H., Marinuzzi, R., Brummund, U., and Magre, Ph., "PIV Measurements in a Mach 2 Hydrogen-air Supersonic Combustion," AIAA Paper 2001-1757, 10th International Space Planes Conference, Kyoto, Japan, April, 2001.

[20] Lang, H. at al. "Stereoscopic Particle Image Velocimetry in a Transonic Turbine Stage." *Experiments in Fluids*, Vol. 32, 2002, pp. 700-709.

[21] Ikeda, Y., Kuratani, N., and Nakajima, T., "M2.5 Supersonic PIV Measurement in Step-back Flow with the Normal Injection," AIAA Paper 2002-0232, 40th Aerospace Sciences Meeting, Reno, NV, January, 2002.

[22] Scarano, F., and van Oudheusden B.W., "Planar Velocity Measurements of a Two-dimensional Compressible Wake," *Experiments in Fluids*, Vol. 34, 2003, pp 430-441.

[23] Alkislar, M.B., Krothapalli, A., and Lourenco, L.M., "Structure of a Screeching Rectangular Jet: A Stereoscopic Particle Image Velocimetry Study," *Journal of Fluid Mechanics*, Vol. 489, 2003, pp. 121-154.

[24] Scheel, F., "PIV Measurement of a 3-dimensional Reacting Flow in a Scramjet Combustion Chamber," AIAA Paper 2004-1038, 42nd AIAA Aerospace Sciences Meeting, 5-8 January, 2004.

[25] Gupta, A.K., Lourenco, L., Linck, M., and Archer, S., "New Particle-Image-Velocimetry Method to Measure Flowfields in Luminous Spray Flames," *Journal of Propulsion and Power*, Vol. 20, No.2, March-April 2004, pp. 369-372.

[26] Tanahashi, M., Shinichirou, M., Choi, G-M., Fukuchi, Y., and Miyauchi, T., "Simultaneous CH-OH PLIF and Stereoscopic PIV Measurements of Turbulent Premixed Flames," *Proceedings of the Combustion Institute*, Vol. 30, 2005, pp.1665-1672.

[27] Arai, T., Sakaue, S., Morisaki, T., Kondo, A., Hiejima, T., and Nishioka, M., "Supersonic Streamwise Vortices Breakdown in Scramjet Combustor," AIAA Paper 2006-8025, 14th Space Planes and Hypersonic Systems and Technologies Conference.

[28] Goyne, C.P., Rodriguez, C.G., Krauss, R.H., McDaniel, J.C., and McClinton, C.R., "Experimental and Numerical Study of a Dual-Mode Scramjet Combustor," *Journal of Propulsion and Power*, Vol. 22, No. 3, 2006. pp. 481-489.

[29] Filatyev, S.A, "Application of Simultaneous Stereo PIV and Double Pulsed Acetone PLIF to Study Turbulent Premixed Flames," AIAA Paper 2006-8025, 45th AIAA Aerosapce Sciences Meeting and Exhibit, January 2007.

[30] Beresh, S. J., Henfling, J. F., Erven, R. J., and Spillers, R. W., "Vortex Structure Produced by a Laterally Inclined Supersonic Jet in Transonic Crossflow," *Journal of Propulsion and Power*, Vol. 23, No.2, March-April 2007, pp. 353-363.

[31] Smith, C.T. and Goyne, C.P. "Three-component Velocimetry in a Scramjet Combustor." AIAA Paper 2008-5073, 44th AIAA/ASME/SAE/ASEE Joint Propulsion Conference and Exhibit. 21-23 July, 2008.

[32] Wagner, J.L., et al. "Velocimetry Measurements of Unstart in an Inlet-Isolator Model in Mach 5 Flow." *AIAA Journal*. Vol. 48, No. 9, September, 2010.

[33] Tuttle, S.G and Carter, C.D, "Particle Image Velocimetry in an Isothermal and Exothermic High-Speed Cavity." AIAA Paper 2012-0330, 50th AIAA Aerospace Sciences Meeting, 09-12 January 2012, Nashville, TN.

[34] Smith, C.T., and Goyne, C.P., "Application of Stereoscopic Particle Image Velocimetry to a Dual-Mode Scramjet." *Journal of Propulsion and Power*, Vol. 27, No. 6, 20011, pp 1178-1885.

[35] Krauss, R.H., and McDaniel, J.C., "A Clean Air Continuous Flow Propulsion Facility," AIAA Paper 92-3912, AIAA 17th Aerospace Ground Testing Conference, Nashville, TN, July 6-8, 1992.

[36] Krauss, R.H., McDaniel, J.C., Scott, J.E., Whitehusrt, R.B., Segal, C., Mahoney, G.T., and Childers, J.M., "Unique, Clean-air, Continuous-flow, High-stagnation-temperature Facility for Supersonic Combustion Research," AIAA Paper 88-3059, July, 1988.

[37] Fulton, J.A., Edwards, J.R., Hassan, H.A., McDaniel, J.C., Goyne, C.P., Rockwell, R.D., Cutler, A.D., Gallo, E., and Cantu, L., "Continued Hybrid LES/RANS Simulation of a Hypersonic Dual-Mode Scramjet Combustor," AIAA Paper 2013-0117, 51st Aerospace Sciences Meeting, Grapevine, TX, 7-10 Jan, 2013.

[38] McRae, C.D., Johansen, C.T., Danehy, P.M., Gallo, E., Cantu, L., Magnotti, G., Cutler, A.D., Rockwell, R.D., Goyne, C.P., and McDaniel, J.C., "OH PLIF Visualization of the UVa Supersonic Combustion Experiment: Configuration "C"," AIAA Paper 2013-0034, 51st Aerospace Sciences Meeting, Grapevine, TX, 7-10 Jan, 2013.

[39] Cutler, A.D., Magnotti, G., Cantu, L., Gallo, E., Danehy, P.M., Rockwell, R.D., Goyne, C.P., and McDaniel, J.C., "Dual-Pump CARS Measurements in the University of Virginia's Dual-Mode Scramjet: Configuration C," AIAA Paper 2013-0355, 51st AIAA Aerospace Sciences Meeting, Grapevine, TX, 7-10 Jan, 2013.

[40] Shultz, I.A., Goldenstein, C.S., Jeffries, J.B., Hanson, R.K., and Goyne, C.P., "Spatially-resolved TDLAS Measurements of Temperature, H2O Column Density, and Velocity in a Direct-Connect Scramjet Combustor," AIAA Paper 2014-1241, 52nd Aerospace Sciences Meeting, 2014, National Harbor, MD.

[41] Rockwell, R.D., Goyne, C.P., Rice, B.E., Kouchi, T, McDaneil, J.C., and Edwards, J.R., "Collaborative Experimental and Computational Study of a Dual-Mode Scramjet Combustor," *Journal of Propulsion and Power*, Vol. 30, No. 3, May-June 2014.

[42] Westerweel, J., "Digital Particle Image Velocimetry: Theory and Application," Delft University Press, 1993.

[43] Raffel, M., Willert, C., Kompenhans, J., *Particle Image Velocimetry – A Practical Guide*, Springer-Verlag, Berlin, 1998.

[44] Willert, C.E., Gharib, M., "Digital Particle Image Velocimetry," *Experiments in Fluids*, Vol. 10, 1991, pp. 181-193.

[45] Keane, R.D., and Adrian, R.J., "Optimization of Particle Image Velocimeters, Part I: Double Pulsed Systems," *Measurement, Science, and Technology*, Vol. 1 No. 11, 1990, pp 1202-1215.

[46] "FlowMaster DaVis 7.2," LaVision, 2007.

[47] Keane, R.D., and Adrian, R.J., "Theory of cross-correlation analysis of PIV Images", *Applied Science Research*, Vol. 49, 1992, pp.191-215.

[48] Fincham, A.M., and Spedding, G.R., "Low Cost, High Resolution DPIV for Measurements of Turbulent Fluid Flow", *Experiments in Fluids*, Vol. 23, 1997, pp. 449-462.

[49] Prasad, A. K., "Stereoscopic Particle Image Velocimetry," *Experiments in Fluids*, Vol. 29, 2000, pp. 103 - 116.

[50] Noqueira, J, Lecuona, A., and Rodriguez, P.A., "Data Validation, False Vectors Correction and Derived Magnitudes Calculation on PIV Data," *Measurement Science and Technology*, Vol. 8 No. 12, pp. 1493-1501.

[51] "532nm Hard Coated Bandpass Interference Filter," Edmund Optics Inc., www.edmundoptics.com.

[52] "Product Datasheet for AngstromSphere Silica Spheres," Fiber Optic Center Inc., New Bedford, MA, www.FOCENTER.com.

[53] Melling, A., "Tracer Particles and Seeding for Particle Image Velocimetry," *Measurement, Science and Technology*, Vol.8 No.12, Dec. 1997, pp 1406 – 1416.

[54] Erbland, P.J., "Development and Application of Carbon Dioxide Enhanced Rayleigh Scattering for High Speed Low Density Flows," Ph.D. Thesis, Princeton University, Princeton, NJ, 2000.

[55] Samimy, M., and Lele, S.K., "Motion of Particles with Inertia in a Compressible Free Shear Layer," *Physics of Fluids*, Vol. 3, Issue 8, Aug. 1991, pp 1915-1923.

[56] Clemens, N.T., Mungal, M.G: "Two- and Three-Dimensional Effects in the Supersonic Mixing Layer," *AIAA Journal*, Vol. 30, No. 4.

[57] Urban, W.D, and Mungal, M.G., "Planar Velocity Measurements in Compressible Mixing Layers," *Journal of Fluid Mechanics*, Vol. 431, 2001, pp 189-222.

[58] Howison, J.C. and Goyne C.P. "Assessment of Seeder Performance for Particle Velcoimetry in a Scramjet Combustor," *Journal of Propulsion and Power*, Vol. 26, No. 3, May, 2010.

[59] Rice, B.E., Goyne, C.P., McDaniel, J.C., and Rockwell, R.D., "Characterization of a Dual-Mode Scramjet via Stereoscopic Particle Image Velocimetry," AIAA Paper 2014-0986, 52nd Aerospace Sciences Meeting, Jan. 2014, National Harbor, MD.

[60] Lutro, H.F., "The Effect of Thermophoresis on the Particle Deposition on a Cylinder," M.S. Thesis, Norwegian University of Science and Technology, 2012.

[61] Loth, E. "Compressibility and Rarefaction Effects on Drag of a Spherical Particle," *AIAA Journal*, Vol. 46, No. 9, 2008.

[62] Samimy, M., and Wernet, M.P., "Review of Planar Multiple-Component Velocimetry in High-Speed Flows," *AIAA Journal*, Vol. 38, No. 4, 2000, pp. 553-574.

[63] McLaughlin, D.K., and Tiederman, W.G., "Biasing Correction for Individual Realization of Laser Anemometer Measurements in Turbulent Flow." *The Physics of Fluids*, Vol. 16, No. 12, pp. 2082-2088.

[64] Meyers, J.F., Kjelgaard, S.O., and Hepner, T.E., "Investigation of Particle Sampling Bias in the Shear Flow Field of a Backward Facing Step," 5th Int. Symp. on Applications of Laser Techniques to Fluid Mechanics, Lisbon, Portugal, July 9-12, 1990.

[65] Petrie, H.L., Samimy, M., and Addy, A.L., "Laser Doppler Velocity Bias in Separated Turbulent Flows," *Experiments in Fluids*, Vol. 6, 1988, pp. 80-88.

[66] Stevenson, W.H., Thompson, H.D., and Roesler, T.C., "Direct Measurement of Laser Velocimeter Bias Errors in a Turbulent Flow," *AIAA Journal*, Vol. 20, 1982, pp. 1720-1723.

[67] Bulusu, K.V., Meyers, J.F., an dPlesniak, M.W., "Estimation of Particle Sample Bias in Shear Layers using Velocity-Data Rate Correlation Coefficient," 16th Int. Symp. on Applications of Laser Techniques to Fluid Mechanics, Lisbon, Portugal, 09-12 July, 2012.

[68] Smith, M.W., "Application of a Planar Doper Velocimetry System to a High Reynolds Number Compressible Jet," AIAA Paper 98-0428, AIAA Aerospace Sciences Meeting, Reno, Nevada, Jan. 12-15, 1998.

[69] Li, D. X., et al., "Bias Errors Induced by Concentration Gradient in Sediment-laden Flow Measurement with PTV," *Journal of Hydrodynamics*, Vol. 24, No. 5, 2012, pp. 668-674.

[70] Li, D. X., Muste, M., and Wang, X. K., "Quantification of Bias Error Induced by Velocity Gradients," *Measurement Sciences and Technology*, Vol. 19, No. 015402, 2008, pp. 1178-1885.

[71] Kirik, J.W., Goyne, C.P., Peltier, S.J., Carter, C.D., and Hagenmaier, M.A., "Velocity Measurements of a Scramjet Cavity Flameholder with Inlet Distortion," *Journal of Propulsion and Power*, 2014, accessed June 10, 2014.

[72] Sciacchitano, A., Wieneke, B., and Scarano, F., "PIV Uncertainty Quantification by Image Matching," *Measurement Science and Technology*, Vol. 24, 2013.

[73] Scarano, F., David, L., Bsibsi, M., and Calluaud, D., "S-PIV Comparative Assessment: Image Dewarping Misalignment Correction and Pinhole Geometric Back Projection," *Experiments in Fluids*, Vol. 39, 2005, pp. 257-266.

[74] Wieneke, B., "Stereo-PIV Using Self-Calibration on Particle Images," *Experiments in Fluids*, Vol. 39, 2005, pp. 267-280.

[75] Beresh, S.J., "Evaluation of PIC Uncertainties using Multiple Configurations and Processing Techniques," AIAA Paper 2008-239, 46th AIAA Aerospace Sciences Meeting, 7-10 January 2009, Reno, NV.

[76] Rice, B.E., Goyne, C.P., and McDaniel, J.C., "Seeding Bias in Particle Image Velocimetry Applied to a Dual-Mode Scramjet," *Journal of Propulsion and Power*, In Review.

[77] Pope, S.B., *Turbulent Flow*s, Cambridge University Press, Cambridge, UK, 2000.

[78] Fleury, V., Bailly, C., Jondeau, E., Michard, M., and Juve, D., "Space-Time Correlations in Two Subsonic Jets Using Dual Particle Image Velocimetry Measurements," *AIAA Journal*, Vol. 46, No. 10, Oct 2008.

[79] Ukeiley, L., Tinney, C.E., Mann, R., and Glauser, M., "Spatial Correlations in a Transonic Jet," *AIAA Journal*, Vol. 45, No. 6, June 2007.

[80] Wernet, M.P, "Time-Resolved PIV for Space-Time Correlations in Hot Jets," Institute of Electrical and Electronics Engineers.

[81] Kerherve, F., Fitzpatrick, J., and Kennedy, J., "Determination of two-dimensional space-time correlations in jet flows using simultaneous PIV and LDC measurements," *Experimental Thermal and Fluid Science*, Vol. 34, 2010, pp. 788-797.

[82] Fulton, J.A., Edwards, J.R., Hassan, H.A., Cutler, A.D., Johansen, C.T., and Danehy, P.M., "Large Eddy/Reynolds-Averaged Navier-Stokes Simulations of Reactive Flow in Dual Mode Scramjet Combustor," *Journal of Propulsion and Power*, Vol. 30, No. 3, May-June 2014.

[83] Burke, M.P., Chaos, M., Ju, Y., Dryer, F.L., and Klipppenstrein, S.J., "Comprehensive H2/O2 Kinetic Model for High-pressure Combustion," *International Journal of Chemical Kinetics*, Vol. 44, No. 7, pp. 444-474, 012.

[84] Smith, C.T., "Stereoscopic Particle Image Velocimetry Measurements in Scramjet Combustors," Ph.D. Thesis, University of Virginia, Charlottesville, VA, 2012.

[85] Schultz, I.A., Goldenstein, C.S., Jeffries, J.B., Hanson, R.K., Rockwell, R.D., Goyne, C.P., "Spatially-Resolved Water Measurements in a Scramjet Combustor Using Diode Laser Absorption," *Journal of Propulsion and Power*.

[86] Busa, K.M., Bryner, E., McDaniel, J.C., Goyne, C.P., Diskin, G.S., Smith, C.T., "Demonstration of Capability of Water Flux Measurement in a Scramjet Combustor Using Tunable Diode Laser Absorption Tomography and Stereoscopic PIV" AIAA Paper 2011-1294, Jan 2011.

[87] Thurow, B.S., Jiang, N., Kim, J., Lempert, W., Samimy, M., "Issues with Measurements of the Convective Velocity of Large-Scale Structures in the Compressible Shear Layer of a Free Jet," *Physics of Fluids*, Vol. 20, 2008.

[88] Lazar, E., DeBlauw, B., Glumac, N., Dutton, C., Elliott, G., "A Practical Approach to PIV Uncertainty Analysis," AIAA Paper 2010-4355, 27th AIAA Aerodynamic Measurement Technology Conference, Chicago, IL, July, 2010.

Appendix A

LaVision ImagerProX2M CCD Camera Technical Data

In the following Appendix A, information regarding the CCD camera used in the current research is available. In addition, technical information regarding the optics and lenses are presented.

List of Figures

Camera Properties

Lens Properties

Table A1: LaVision ImagerProX2M technical data

Category	Unit	Setpoint	ProX2M
resolution (h x v)	pixel	normal	1600 x 1200
pixel size (h x v)	μm^2		7.4 x 7.4
sensor format	mm^2	extended	12.2 x 9
sensor diagonal	mm	extended	15.2
peak quantum efficiency	%	500 nm	55
full well capacity	e^-	normal	40000
linearity range of CCD	e^-	40 MHz	40000
image sensor			KAI-2001
maximum dynamic range	dB		70
dynamic range A/D	bit		14
readout noise	e^- rms	40 MHz	21
frame rate	fps	full frame	30
pixel scan rate	MHz		2 x 40
A/D conversion factor	e^-/count	normal	2.1
spectral range	nm	normal	320-1000
exposure time			500 ns-1000 s
anti-blooming factor		typical	>300
smear	%		0.01
h-binning	pixel		1, 2
v-binning	pixel		1, 2, 4, 8
region of interest	pixel	h x v	1, 2, 3, 4…n
non-linearity	%	full temp. range	<2
uniformity darkness	e^- rms	90% center zone	<20
uniformity brightness	%	typical	2
trigger, aux signals		internal external	software TTL level
power consumption	W	typical maximum	24 40
power supply	VAC		90-260
camera dimensions (w x h x l)	mm^3		84 x 66 x 175
controller dimensions (w x h x l)	mm^3		135 x 51 x 195
weight	kg		1.8
operating temp. range	° C		5-40
operating humidity range	%		10-90
storage temp. range	° C		-20-70
optical input			c-mount/f-mount
data interface			camera link IEEE1394
cooled CCD	° C		+10
cooling method			Peltier cooler
interframing time	ns	full image	110

Table A.2: Nikon 60 mm focal distance, reproduction ratio, and depth of field

Focus Dist. (m)	Depth of Field (m)								Reproduction Ratio
	f/2.8	f/4	f/5.6	f/8	f/11	f/16	f/22	f/32	
0.219	0.219-0.219	0.218-0.219	0.218-0.219	0.218-0.219	0.218-0.219	0.218-0.219	0.218-0.219	0.218-0.219	1
0.22	0.220-0.220	0.219-0.220	0.219-0.220	0.219-0.220	0.219-0.220	0.219-0.220	0.219-0.220	0.219-0.220	1/1.1
0.225	0.225-0.225	0.225-0.225	0.225-0.225	0.225-0.225	0.225-0.225	0.225-0.225	0.224-0.225	0.224-0.225	1/1.3
0.23	0.23-0.23	0.23-0.23	0.23-0.23	0.229-0.23	0.229-0.23	0.229-0.23	0.229-0.23	0.229-0.23	1/1.4
0.235	0.235-0.235	0.234-0.235	0.234-0.235	0.234-0.235	0.234-0.235	0.234-0.235	0.234-0.235	0.234-0.235	1/1.5
0.24	0.239-0.24	0.239-0.24	0.239-0.24	0.239-0.24	0.239-0.24	0.239-0.24	0.239-0.24	0.239-0.24	1/1.7
0.25	0.249-0.25	0.249-0.25	0.249-0.25	0.249-0.25	0.249-0.25	0.249-0.25	0.248-0.251	0.248-0.251	1/1.9
0.27	0.269-0.27	0.269-0.27	0.269-0.27	0.269-0.27	0.269-0.271	0.268-0.271	0.267-0.272	0.267-0.273	1/2.3
0.3	0.299-0.3	0.299-0.3	0.299-0.301	0.298-0.301	0.298-0.302	0.297-0.302	0.296-0.304	0.294-0.305	1/2.8
0.35	0.349-0.351	0.348-0.351	0.348-0.352	0.347-0.352	0.346-0.354	0.344-0.355	0.342-0.358	0.339-0.361	1/3.7
0.4	0.398-0.401	0.397-0.402	0.396-0.403	0.395-0.404	0.393-0.406	0.391-0.409	0.387-0.413	0.382-0.419	1/4.6
0.5	0.496-0.503	0.495-0.504	0.493-0.506	0.491-0.509	0.487-0.513	0.482-0.519	0.475-0.528	0.466-0.541	1/6.3
0.7	0.692-0.708	0.688-0.711	0.684-0.716	0.677-0.724	0.669-0.734	0.657-0.75	0.641-0.773	0.62-0.809	1/9.7
1	0.981-1.020	0.973-1.029	0.963-1.041	0.948-1.059	0.929-1.085	0.903-1.126	0.868-1.189	0.825-1.296	1/14.7
2	1.914-2.096	1.88-2.138	1.835-2.202	1.774-2.298	1.696-2.451	1.597-2.709	1.477-3.189	1.336-4.281	1/31.4
?	38.3-?	27.1-?	19.2-?	13.6-?	9.6-?	6.8-?	4.9-?	3.5-?	1/?

Table A.3: Nikon 105 mm focal distance, reproduction ratio, and depth of field

Focus Dist. (m)	Depth of Field (m)								Reproduction Ratio
	f/2.8	f/4	f/5.6	f/8	f/11	f/16	f/22	f/32	
0.314	0.314-0.313	0.314-0.313	0.314-0.313	0.314-0.313	0.314-0.313	0.314-0.313	0.315-0.312	0.315-0.312	1
0.32	0.320-0.319	0.320-0.319	0.320-0.319	0.320-0.319	0.320-0.319	0.321-0.318	0.321-0.318	0.322-0.317	1/1.1
0.33	0.330-0.329	0.330-0.329	0.330-0.329	0.330-0.329	0.331-0.329	0.331-0.328	0.332-0.328	0.332-0.327	1/1.3
0.34	0.340-0.339	0.340-0.339	0.340-0.339	0.340-0.339	0.341-0.338	0.341-0.338	0.342-0.337	0.33-0.336	1/1.4
0.35	0.350-0.349	0.350-0.349	0.350-0.349	0.351-0.349	0.351-0.348	0.351-0.348	0.352-0.347	0.354-0.346	1/1.6
0.37	0.370-0.369	0.370-0.369	0.370-0.369	0.371-0.368	0.371-0.368	0.372-0.367	0.373-0.366	0.375-0.365	1/1.8
0.4	0.400-0.399	0.400-0.399	0.401-0.398	0.401-0.398	0.402-0.397	0.403-0.396	0.404-0.395	0.406-0.393	1/2.1
0.45	0.450-0.449	0.451-0.448	0.451-0.448	0.452-0.447	0.453-0.446	0.455-0.445	0.457-0.443	0.460-0.440	1/2.7
0.5	0.501-0.498	0.501-0.498	0.502-0.497	0.503-0.496	0.504-0.495	0.506-0.493	0.509-0.490	0.514-0.487	1/3.2
0.6	0.602-0.598	0.602-0.597	0.604-0.596	0.605-0.594	0.608-0.592	0.611-0.589	0.616-0.585	0.623-0.579	1/4.2
0.8	0.804-0.796	0.805-0.794	0.808-0.792	0.811-0.789	0.816-0.784	0.823-0.778	0.834-0.769	0.849-0.758	1/6.2
1	1.007-.993	1.009-.990	1.013-.986	1.019-.981	1.028-.973	1.04-.963	1.058-.949	1.084-.930	1/8.1
1.5	1.517-1.484	1.524-1.477	1.535-1.468	1.549-1.455	1.571-1.437	1.602-1.413	1.649-1.38	1.721-1.336	1/12.9
3	3.075-2.931	3.107-2.903	3.154-2.864	3.222-2.811	3.324-2.739	3.48-2.654	3.73-2.522	4.156-2.369	1/27.2
?	115.61-?	81.81-?	57.91-?	41-?	29.05-?	20.6?	14.63-?	10.4-?	1/?

Appendix B

Supplemental SPIV Figures: Strain Rate, Reynolds Stress, and Turbulence Intensity at x/H=6, 12, and 82 (φ=0.18 and φ=0.49)

For the purpose of brevity in the main document, additional mean scalars and turbulence statistics that are derived from the SPIV experimental data are presented in Appendix B. The quantities of strain rate, Reynolds (shear) stress, and turbulence intensity are presented in the following section.

List of Figures

Strain Rate

First, the normal strain in the y-direction, E_{yy}, is examined in Fig. B.1. A trend of decreased strain rate as the axial location increases is observed.

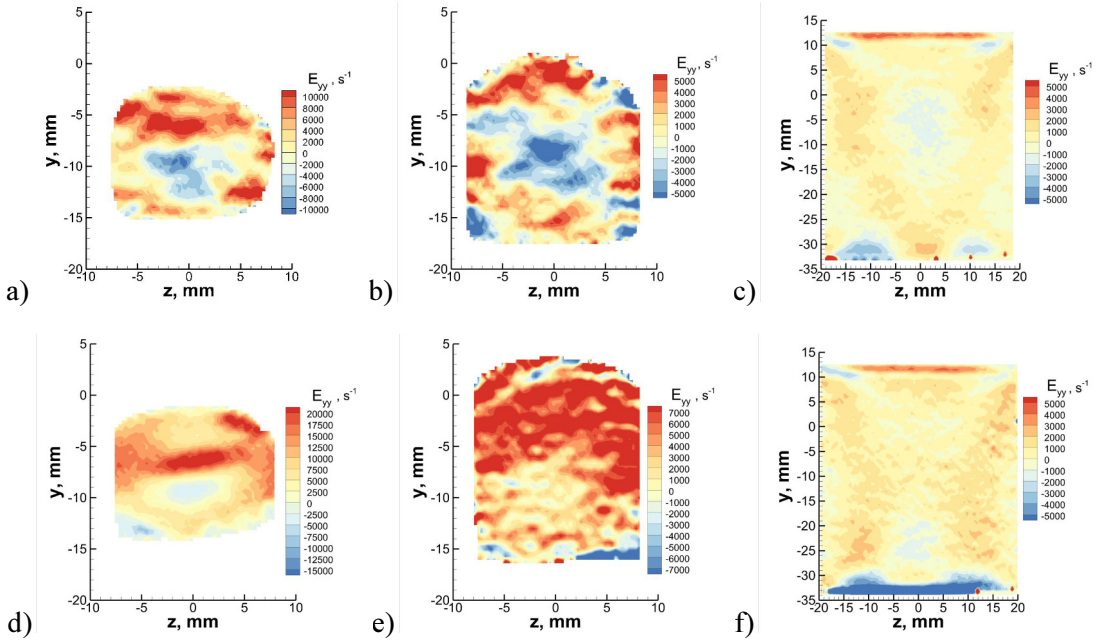

Figure B.1: Strain E_{yy}: a) x/H=6, φ=0.18, b) x/H=12, φ=0.18, c) x/H=82, φ=0.18, d) x/H=6, φ=0.49, e) x/H=12, φ=0.49, f) x/H=82, φ=0.49.

This is consistent with a trend of decreasing vorticity and mixing with increasing axial location shown in Chapter 6. At x/H=6 and x/H=12 for the φ=0.18 fuel condition, positive normal strain values occur towards the edge of the combusting plume whereas negative normal strain occurs in the center of the plume. Positive strain values indicate expansion whereas negative strain values indicate compression. This is due to an increasing magnitude of the V-component of velocity in the negative y-direction. It has been shown that for the φ=0.18 case the V-component of velocity tends to act in the negative y-direction, which serves to transport the high-speed freestream air into the combusting plume. Alternatively, for the φ=0.49 case, the V-component of velocity tends to act in the positive y-direction, meaning the combusting plume is being transported into

the freestream region. The positive strain in the region of the shear layer indicates an increasing V-velocity component in the positive y-direction. At the exit measurement plane location, for both fuel equivalence ratios, the strain rate is minimal and predominantly constant across the duct area.

Contour plots of the normal strain in the z-direction are presented in Fig. B.2.

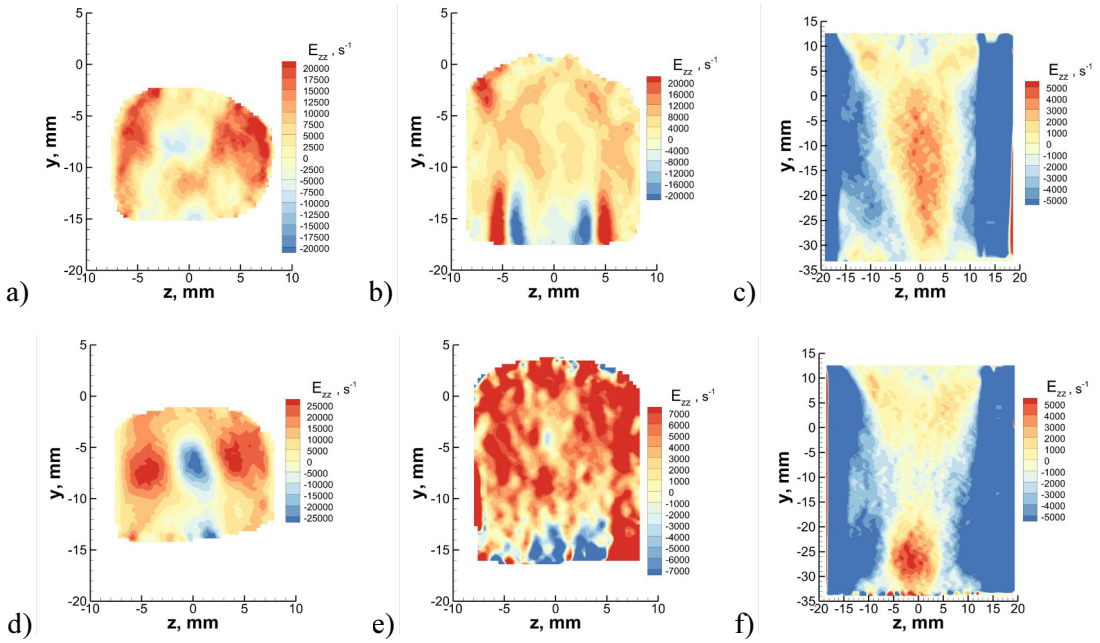

Figure B.2: Strain E_{zz}: a) x/H=6, φ=0.18, b) x/H=12, φ=0.18, c) x/H=82, φ=0.18, d) x/H=6, φ=0.49, e) x/H=12, φ=0.49, f) x/H=82, φ=0.49.

At x/H=6 for both fuel conditions, a similar distribution of normal strain in the z-direction is observed. Positive strain values are symmetrically distributed around low negative values in the center of the plume. This indicates increasing W-components of velocity in the positive z-direction representative of expansion in this direction. At x/H=12 and φ=0.18, sharp regions of positive strain adjacent to regions of negative strain indicate an increase in the W-velocity component followed by an abrupt decrease in the positive z-direction. For the x/H=12 location at φ=0.49, the strain is predominantly positive with isolated negative values near the ramp induced vortices. At the exit plane

for both fuel conditions, maximum values of negative strain are seen at the edges of the duct as a result of the strong W-velocity component due to entrained air, as was shown in Chapter 6. Again, the same trend of decreased strain as the axial dimension increases is observed.

Contour plots of shear strain, E_{yz}, for all measurement planes and fuel equivalence ratios are presented in Fig. B.3

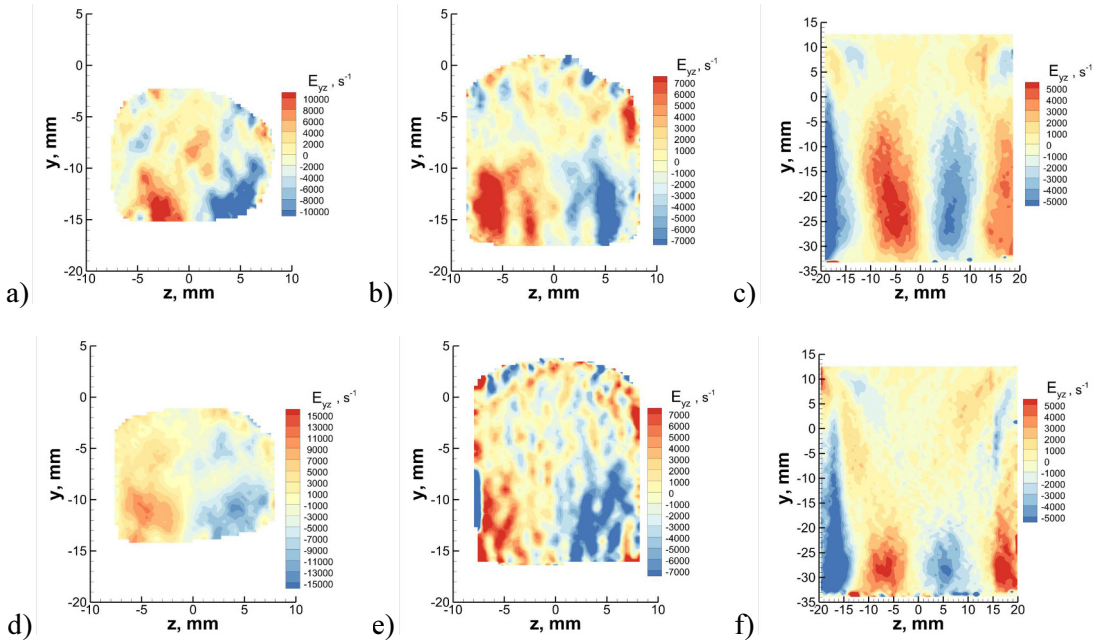

Figure B.3: Strain E_{yz}: a) x/H=6, φ=0.18, b) x/H=12, φ=0.18, c) x/H=82, φ=0.18, d) x/H=6, φ=0.49, e) x/H=12, φ=0.49, f) x/H=82, φ=0.49.

As expected, maximum shear strain occurs in the regions corresponding to the ramp induced vortices shown in Chapter 6. It is observed that positive shear strain is centered on the left vortex and negative shear strain is centered on the right vortex for all axial locations and both modes of combustion. This is due to the counterclockwise motion of the left vortex and clockwise motion of the right vortex. Shear strain is a dominant force responsible for the mixing of the fuel and air and indicates the location of strong velocity gradients. Positive shear strain on the left side indicates an increase in the V-velocity

component in the z-direction and negative shear strain indicates a decrease in V-velocity in the z-direction. Likewise, the shear strain, E_{yz}, decreases as the axial location increases. It can be seen that the velocity gradients in the V-component of velocity are most concentrated at x/H=6 and have spread out by the exit plane, particularly for the φ=0.18 case.

Contour plots of the shear strain, E_{zy}, are presented in Fig. B.4. The shear strain, E_{zy}, represents the derivative of the W-component of velocity with respect to the y-direction.

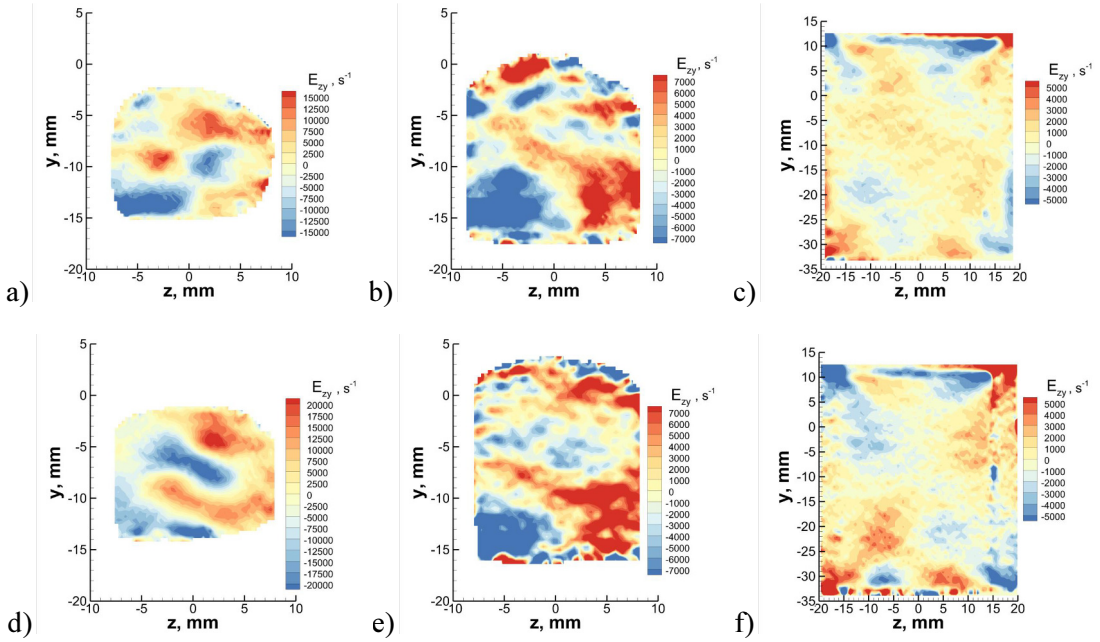

Figure B.4: Strain E_{zy}: a) x/H=6, φ=0.18, b) x/H=12, φ=0.18, c) x/H=82, φ=0.18, d) x/H=6, φ=0.49, e) x/H=12, φ=0.49, f) x/H=82, φ=0.49.

Again, it is expected that peak regions of shear strain correspond to the location of the ramp induced vortices which is verified by Fig. B.4. The magnitude of shear strains, E_{zy} and E_{yz} are comparable at the x/H=6 and x/H=12 planes, meaning the velocity gradients in both directions are similar. In contrast, at x/H=82, the shear strain E_{yz} is significantly higher than E_{zy} in the regions of the ramp induced vortices, meaning the velocity gradient

of the V-component of velocity in the z-direction is dominant. This is supported by the elliptical nature of the vortices at x/H=82 and φ=0.18 with a major axis in the y-direction.

Reynolds Stresses (turbulent shear stress terms)

Figures B.5-7 present the Reynolds stress terms ($\overline{u'v'}$, $\overline{u'w'}$, and $\overline{v'w'}$). First the Reynolds stress ($\overline{u'v'}$) is presented in Fig. B.5 which is the ensemble average of the product of the fluctuating u'- and v'-components of velocity.

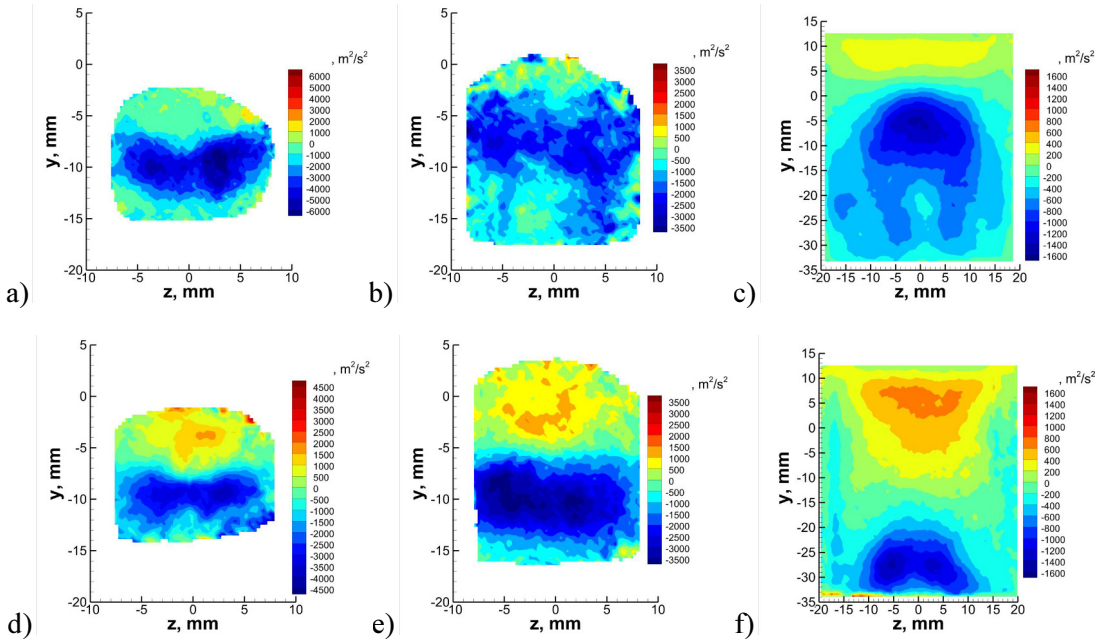

Figure B.5: Reynolds Stress $\overline{u'v'}$: a) x/H=6, φ=0.18, b) x/H=12, φ=0.18, c) x/H=82, φ=0.18, d) x/H=6, φ=0.49, e) x/H=12, φ=0.49, f) x/H=82, φ=0.49.

It is clear that the fluctuating velocity component in the axial x-direction (u') is dominant and the distributions of the covariance between u' and v' resemble the distributions of Fig. 6.8 of turbulent kinetic energy. Negative regions of covariance indicate the tendency of the fluctuating velocity components to act in opposite directions whereas positive regions of covariance indicate the tendency of the fluctuating velocity components to act in the same direction. Therefore, in the dark blue region of the shear layer in Fig. B.6a, a

positive velocity fluctuation in U will result in a negative fluctuation in V and vice versa. It is interesting to note that at x/H=6 and x/H=12 (φ=0.18) the Reynolds stress ($\overline{u'v'}$) is predominantly negative with little-to-no positive correlation. An explanation for this finding could be that positive fluctuations in V velocity result in a deceleration of the U velocity and therefore a negative U fluctuation. At x/H=82 and φ=0.18, peak negative values of covariance occur in the shear layer between the combusting plume and freestream with a concentrated region of positive covariance at the top of the duct where limited combustion takes place. This indicates that the combustion and heat release are primarily responsible for negative fluctuations in the axial velocity component U. In contrast, for the φ=0.49 case, both positive and negative values of covariance exist. Positive values of covariance exist above the fuel jet core towards the freestream and negative values of covariance exist below the fuel jet core near the fuel injector wall. As is evident from Fig. 6.6, the expanding plume, and therefore positive values of the V-velocity component above the fuel jet, could be responsible for this. The same trend is seen at x/H=6 and x/H=12 for the φ=0.49 case except for increased shear layer grown at x/H=12. At x/H=82 and φ=0.49, positive values of covariance are concentrated in the regions of vorticity with positive values in the freestream. These larger regions of negative covariance at x/H=82 for the φ=0.18 case compared to the φ=0.49 case are most likely due to the increased penetration and influence of the ramp induced vortices. A trend of decreasing Reynolds stress along the axial x-direction is observed, which is a result of decreasing turbulent kinetic energy and decreasing vortex strength.

The Reynolds stress ($\overline{u'w'}$) is presented in Fig. B.6 which is the ensemble average of the product of the fluctuating u'- and w'-components of velocity. Significantly different distributions of covariance are observed for $\overline{u'v'}$ compared to $\overline{u'w'}$. A clear asymmetry exists about the z=0 axis with positive values of covariance near the left side vortex and negative values of covariance near the right side vortex. This is due to the symmetric nature of the W-component of velocity

which in a mean sense is typically negative on the left side of the z=0 axes and typically positive on the right side of the z=0 axes. Therefore, the ramp induced vortices have a greater influence on the $\overline{u'w'}$ than the $\overline{u'v'}$ covariance. The distributions indicate that positive fluctuations in W due to the left vortex tend to correspond with positive fluctuations in U and vice versa. Alternatively, positive fluctuations in W due the right vortex are negatively correlated with fluctuations in U. This is consistent because if there is a fluctuation in vortex strength (and therefore W-velocity) the difference between the instantaneous value and the mean value of the W-velocity component have opposite signs depending on the z=0 line of symmetry.

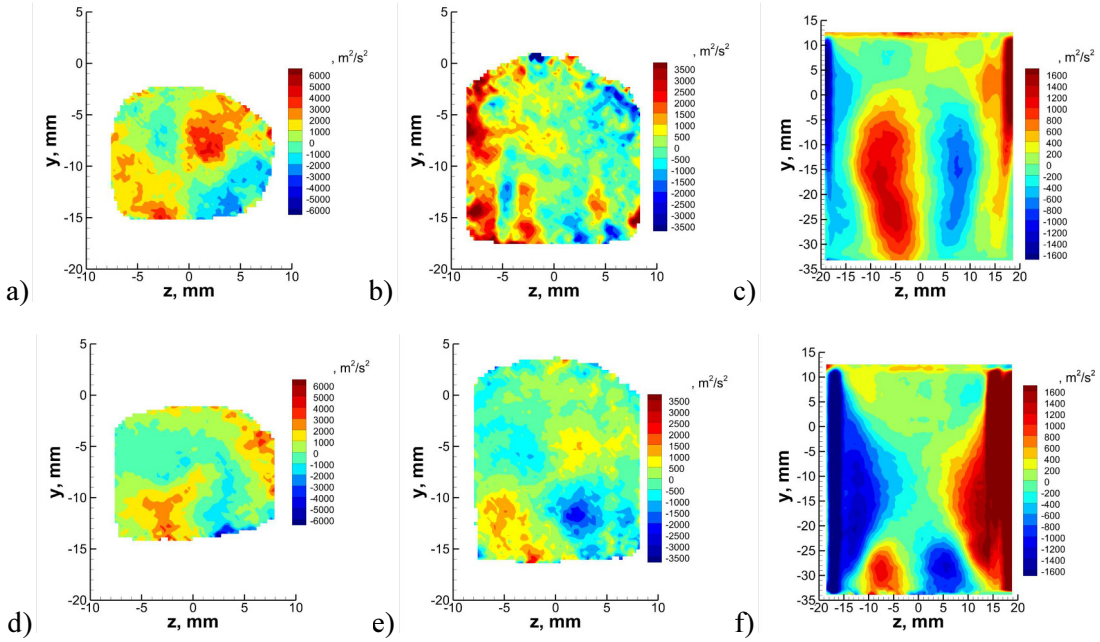

Figure B.6: Reynolds Stress $\overline{u'w'}$: a) x/H=6, φ=0.18, b) x/H=12, φ=0.18, c) x/H=82, φ=0.18, d) x/H=6, φ=0.49, e) x/H=12, φ=0.49, f) x/H=82, φ=0.49.

At x/H=6 for both fuel conditions, fluctuations occur in two small regions near the fuel injection wall with secondary regions of opposite sign above. This feature was observed in Fig. 6.7 where there existed primary and secondary regions of vorticity which cause velocity fluctuations. At x/H=12 for both fuel conditions, the turbulent shear stresses are more distributed but still focused on the ramp induced vortices which have spread further downstream in the flowpath. At x/H=82 for both fuel conditions peak fluctuations occur in the regions of highest vorticty (Fig. 6.7). The

results of Fig. B.5 indicate that the primary flow feature causing turbulent shear stresses between U and W are the ramp induced vortices. In addition, at x/H=82, the effect of the large W-velocity components due to entrained air causes significant velocity fluctuations.

The Reynolds stress ($\overline{v'w'}$) is presented in Fig. B.7 which is the ensemble average of the product of the fluctuating v'- and w'-components of velocity. This corresponds to the covariance of the in-plane velocity vectors. Again, it is expected that turbulent shear stress due to the fluctuations of the in-place velocity vectors will be dominated by the ramp induced vortices.

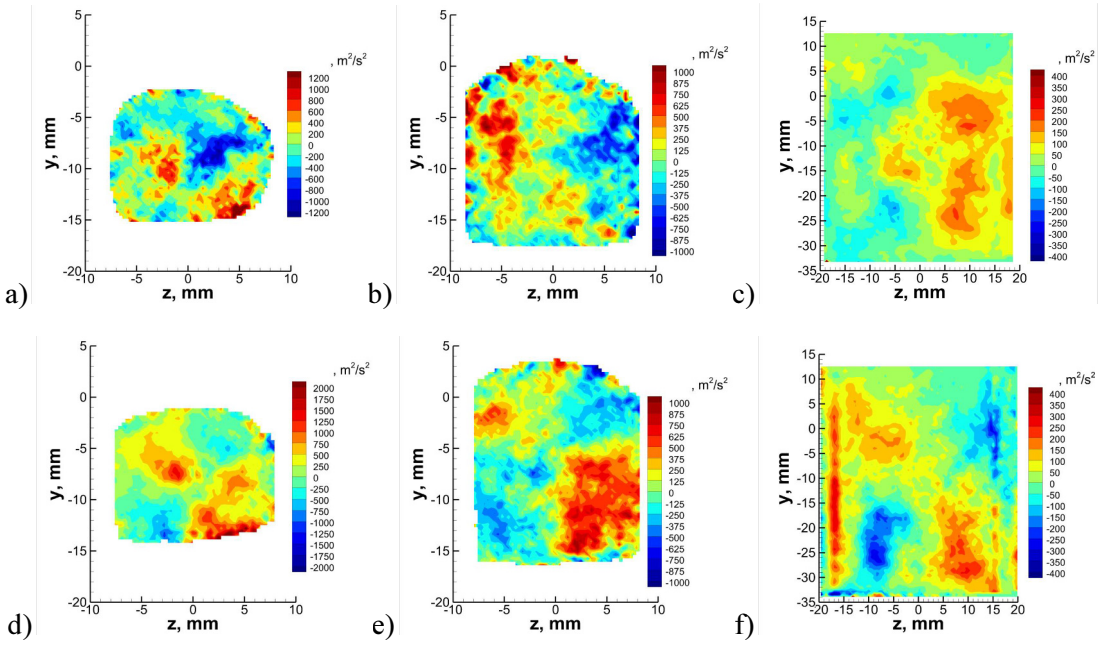

Figure B.7: Reynolds Stress $\overline{v'w'}$: a) x/H=6, φ=0.18, b) x/H=12, φ=0.18, c) x/H=82, φ=0.18, d) x/H=6, φ=0.49, e) x/H=12, φ=0.49, f) x/H=82, φ=0.49.

There is a sign symmetry about the z=0 axes due to the opposite sign of the W-component of velocity similar to that seen in Fig. B.6. Again, there exists two regions of peak turbulent shear stress (with opposite signs) at x/H=6 for both fuel conditions like was observed in Fig. B.6. At x/H=12, the covariance is more chaotic for the φ=0.18 case and more concentrated for the φ=0.49 case. At the exit plane, there exists less influence of the entrained air meaning there is less correlation between the fluctuating V and W-components than for the fluctuating U and W-components. The main trend observed for all three covariance's ($\overline{u'v'}$, $\overline{u'w'}$, and $\overline{v'w'}$) is a

decrease in turbulent shear stress as the axial location moves downstream. Overall, significantly higher turbulent shear stress occurred for $\overline{\boldsymbol{u'v'}}$ and $\overline{\boldsymbol{u'w'}}$ when compared to $\overline{\boldsymbol{v'w'}}$ due to the highly turbulent nature of the axial velocity component.

Turbulence Intensity

The turbulence intensity is defined as the ratio of the 3C RMS velocity and the 3C mean velocity magnitude given in Eqns. B.1-B.3.

$$TI = 100\,{|v|}\Big/{|\bar{V}|} \tag{B.1}$$

$$|\bar{V}| = \sqrt{\bar{U}^2 + \bar{V}^2 + \bar{W}^2} \tag{B.2}$$

$$|v| = \sqrt{\overline{u'}^2 + \overline{v'}^2 + \overline{w'}^2} \tag{B.3}$$

Normalizing by the mean velocity magnitude indicates the degree of turbulent fluctuations. Fig. B.8 presents contour plots of turbulence intensity at x/H=6, x/H=12, and x/H=82 for both fuel conditions (φ=0.18 and φ=49). The measurement planes appear from left to right and the fuel conditions from top to bottom.

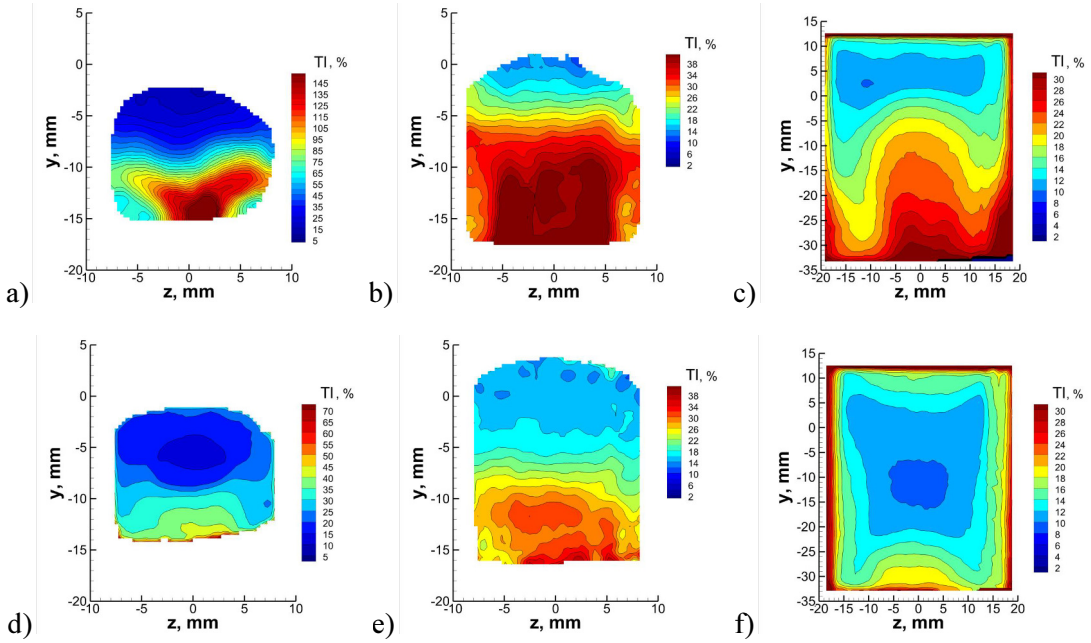

Figure B.8: Turbulence Intensity: a) x/H=6, φ=0.18, b) x/H=12, φ=0.18, c) x/H=82, φ=0.18, d) x/H=6, φ=0.49, e) x/H=12, φ=0.49, f) x/H=82, φ=0.49.

It is clear from Fig. B.8 that the scramjet mode of operation has significantly higher turbulence intensity than the ramjet mode at all measurement plane locations. This is due to the occurrence of relatively high RMS velocity in regions of the low-speed separated region for the scramjet case. Alternatively, high RMS velocity occurs in the regions of the high-speed fuel jet for the ramjet case. The highest turbulence intensity occurs at the x/H=6 measurement plane for both modes of operation and is shown to decrease with an increase in the axial dimension downstream of fuel injection. It is interesting to note that peak levels of turbulence intensity occur near the fuel injection wall for all measurement planes and fuel conditions. This indicates that the primary source of turbulent fluctuations occur due to the combustion process with relatively low turbulence intensity at high y-values in the high-speed freestream. When compared to a non-combusting mixing case of Config. A [84] the turbulence intensity at x/H=12 ranged from 7-13%. Therefore, the combustion process results in an increase in turbulence intensity of approximately 30%.

Despite comparable levels of TKE at corresponding measurement plane locations for the two modes of operation, there exists a significant difference in the turbulence intensity. This is due to the significantly different mean velocity fields which normalize the TKE and can be seen in the distributions of the turbulence intensity contours. Therefore, the shape of the distribution of turbulence intensity resembles the distributions of mean velocity magnitude. For example, regions of low velocity magnitude often result in regions of high turbulence intensity which is indicated in Fig. B.8.

Appendix C

Supplemental SPIV and CFD Velocity Component Comparisons

Comparisons of individual mean velocity components, $\overline{U}$, $\overline{V}$, and $\overline{W}$ between the SPIV measurements and CFD simulations are presented in Appendix C. Contour maps are constructed for all measurement planes and fuel equivalence ratios as well as comparison line plots.

List of Figures

Contour Maps

Line Plots

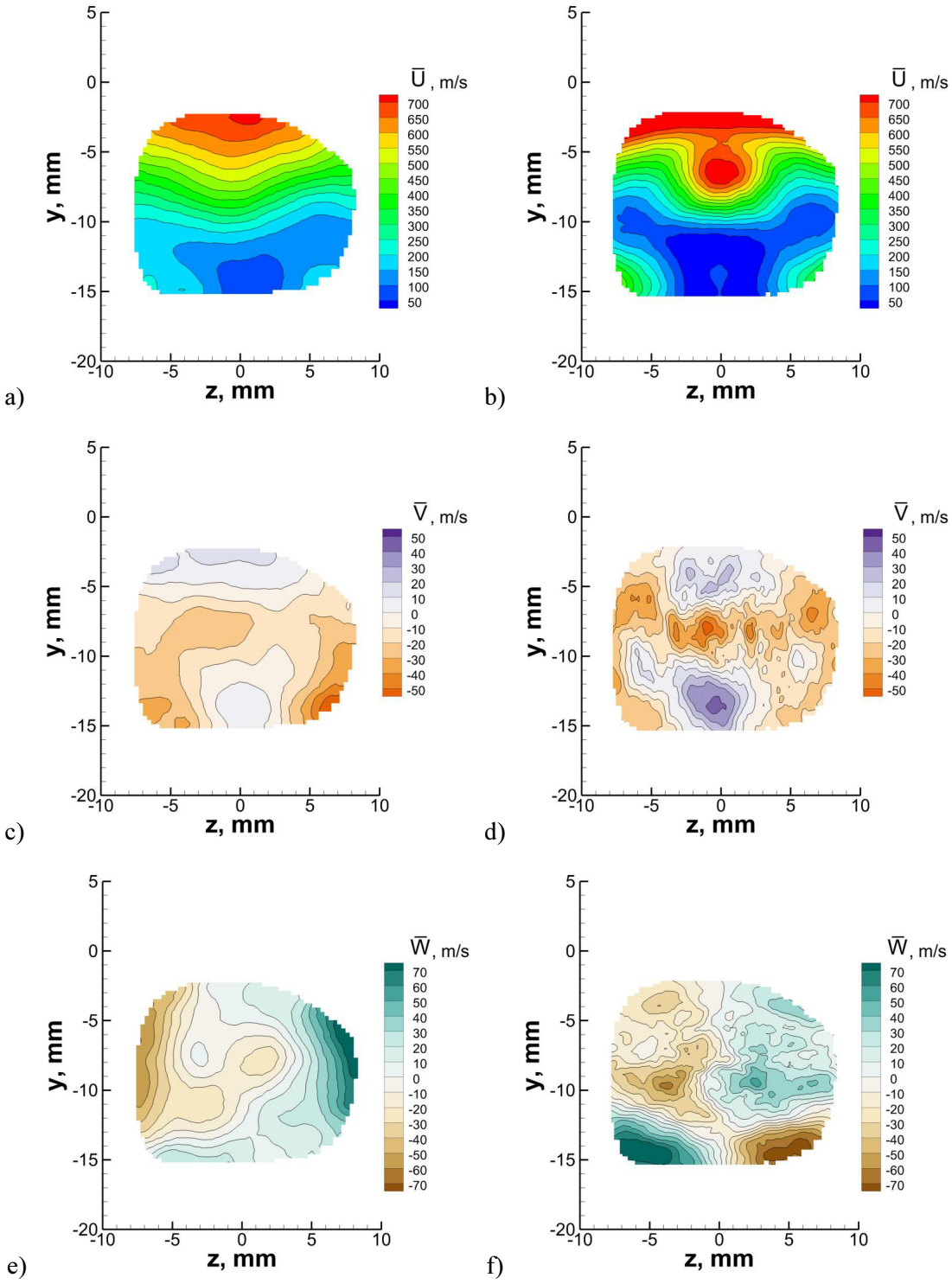

Figure C.1: x/H=6, φ=0.18: a) SPIV, $\bar{U}$, b) CFD, $\bar{U}$, d) SPIV, $\bar{V}$, d) CFD, $\bar{V}$, e) SPIV, $\bar{W}$, f) CFD, $\bar{W}$.

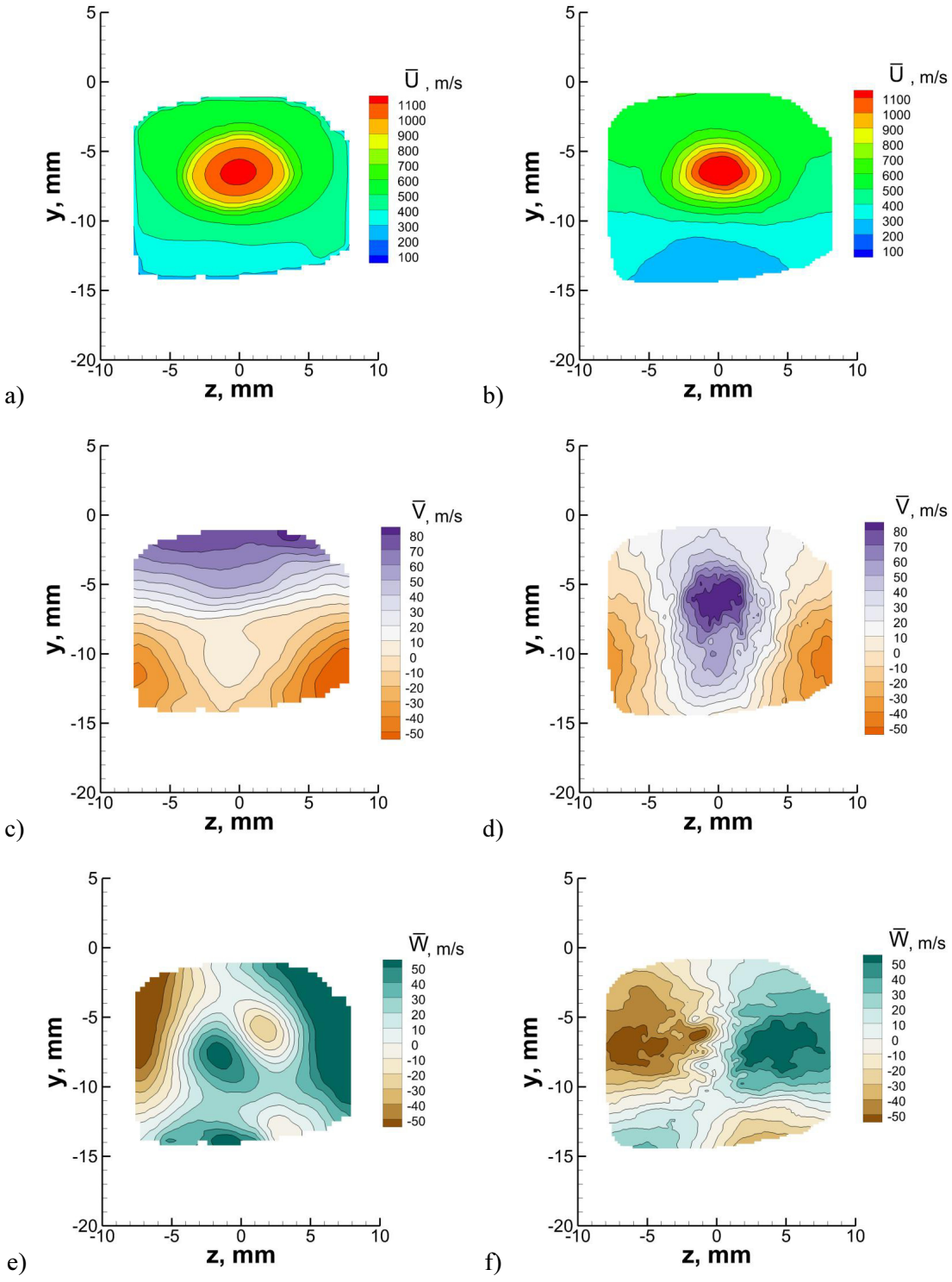

Figure C.2: x/H=6, φ=0.49: a) SPIV, $\bar{U}$, b) CFD, $\bar{U}$, d) SPIV, $\bar{V}$, d) CFD, $\bar{V}$, e) SPIV, $\bar{W}$, f) CFD, $\bar{W}$.

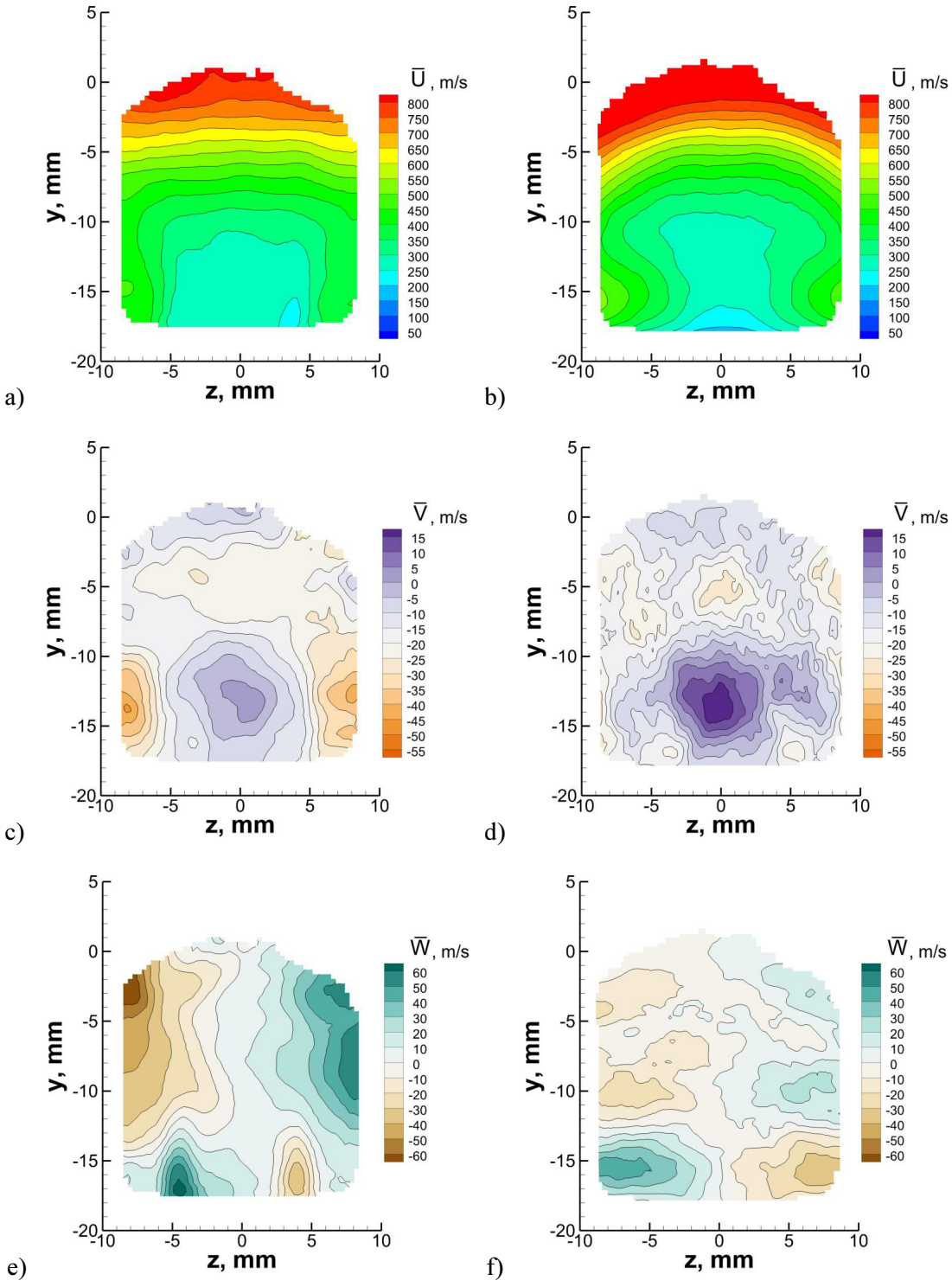

Figure C.3: x/H=12, φ=0.18: a) SPIV, $\bar{U}$, b) CFD, $\bar{U}$, d) SPIV, $\bar{V}$, d) CFD, $\bar{V}$, e) SPIV, $\bar{W}$, f) CFD, $\bar{W}$.

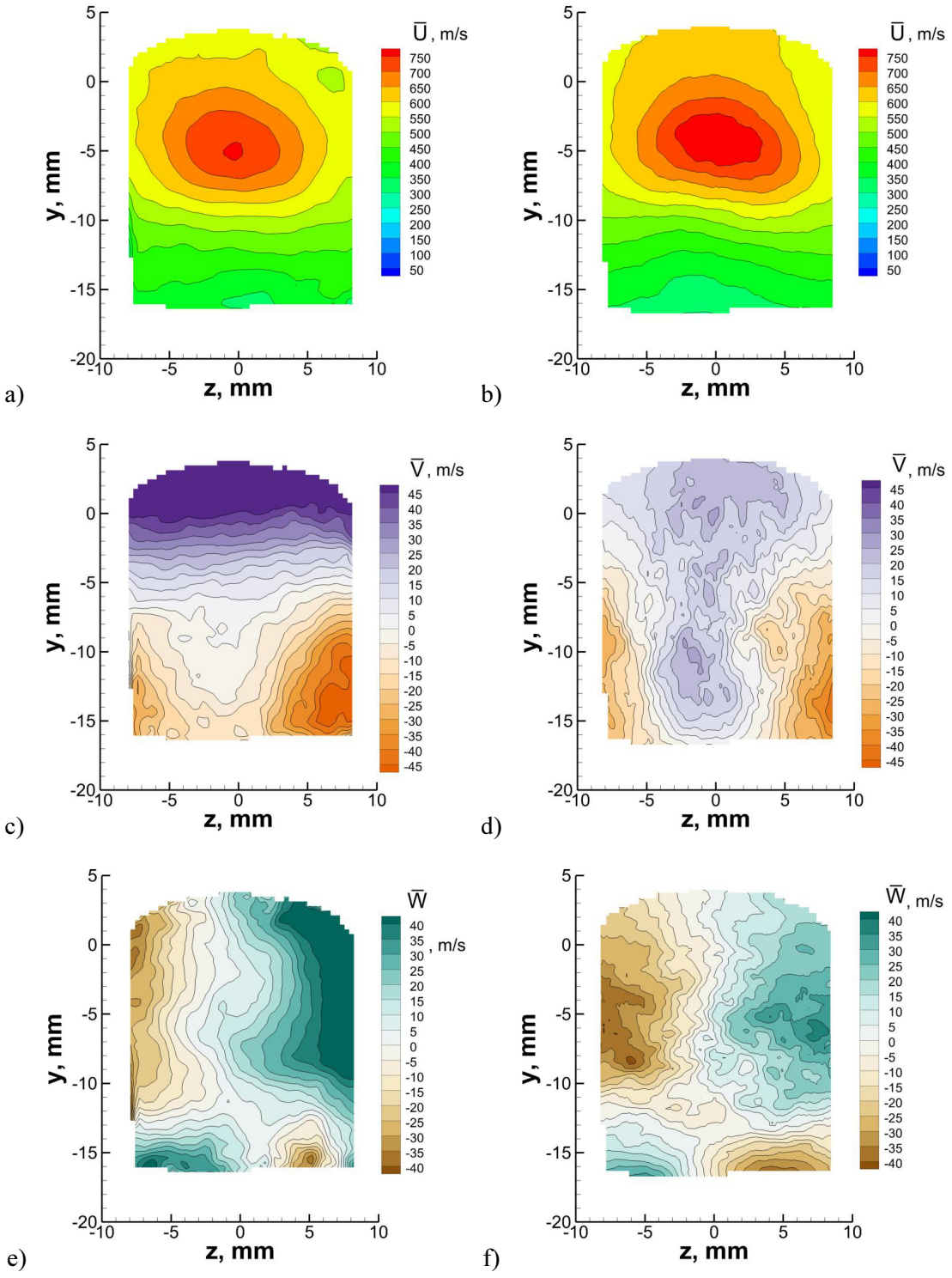

Figure C.4: x/H=12, φ=0.49: a) SPIV, Ū, b) CFD, Ū, d) SPIV, V̄, d) CFD, V̄, e) SPIV, W̄, f) CFD, W̄.

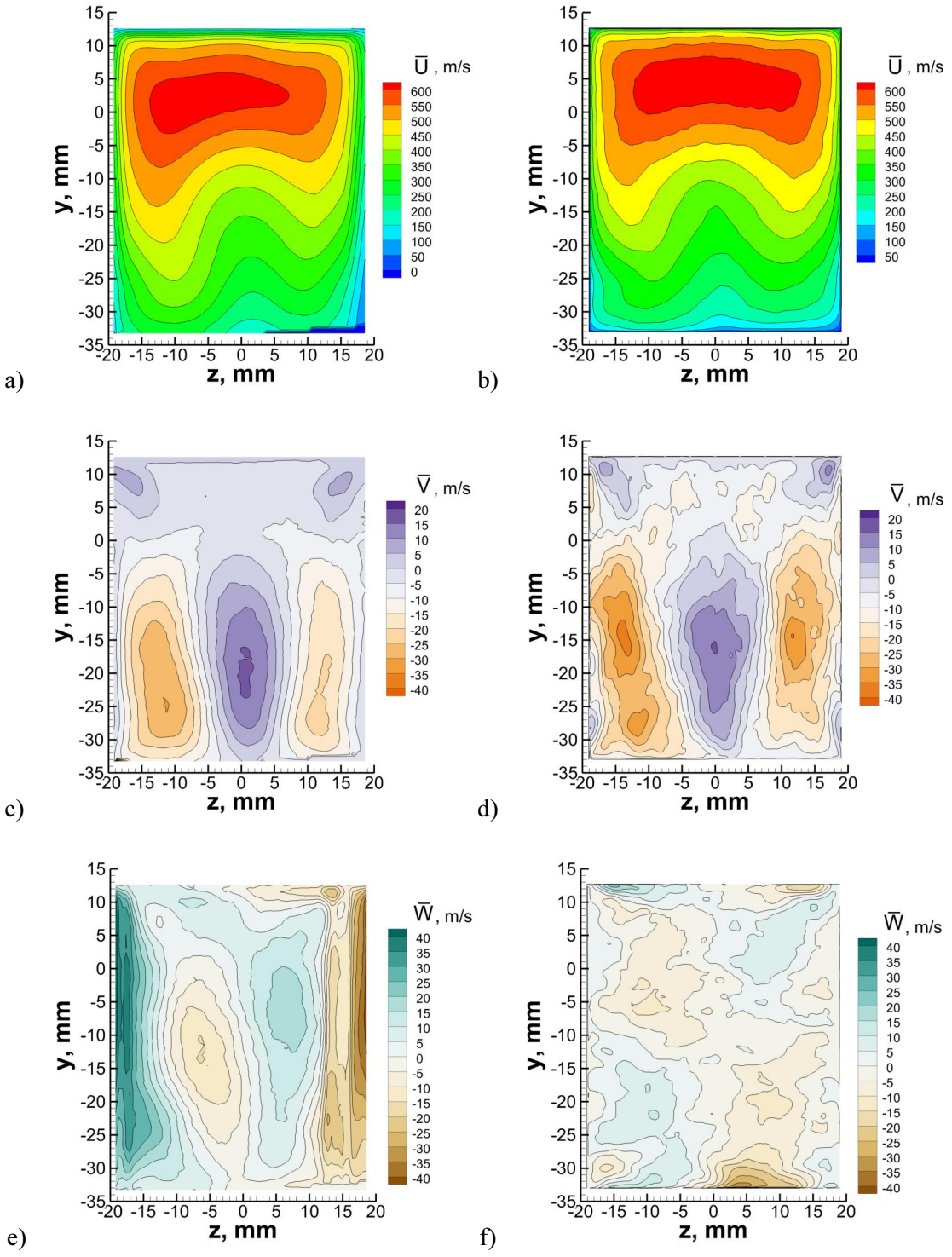

Figure C.5: x/H=82, φ=0.18: a) SPIV, Ū, b) CFD, Ū, d) SPIV, V̄, d) CFD, V̄, e) SPIV, W̄, f) CFD, W̄.

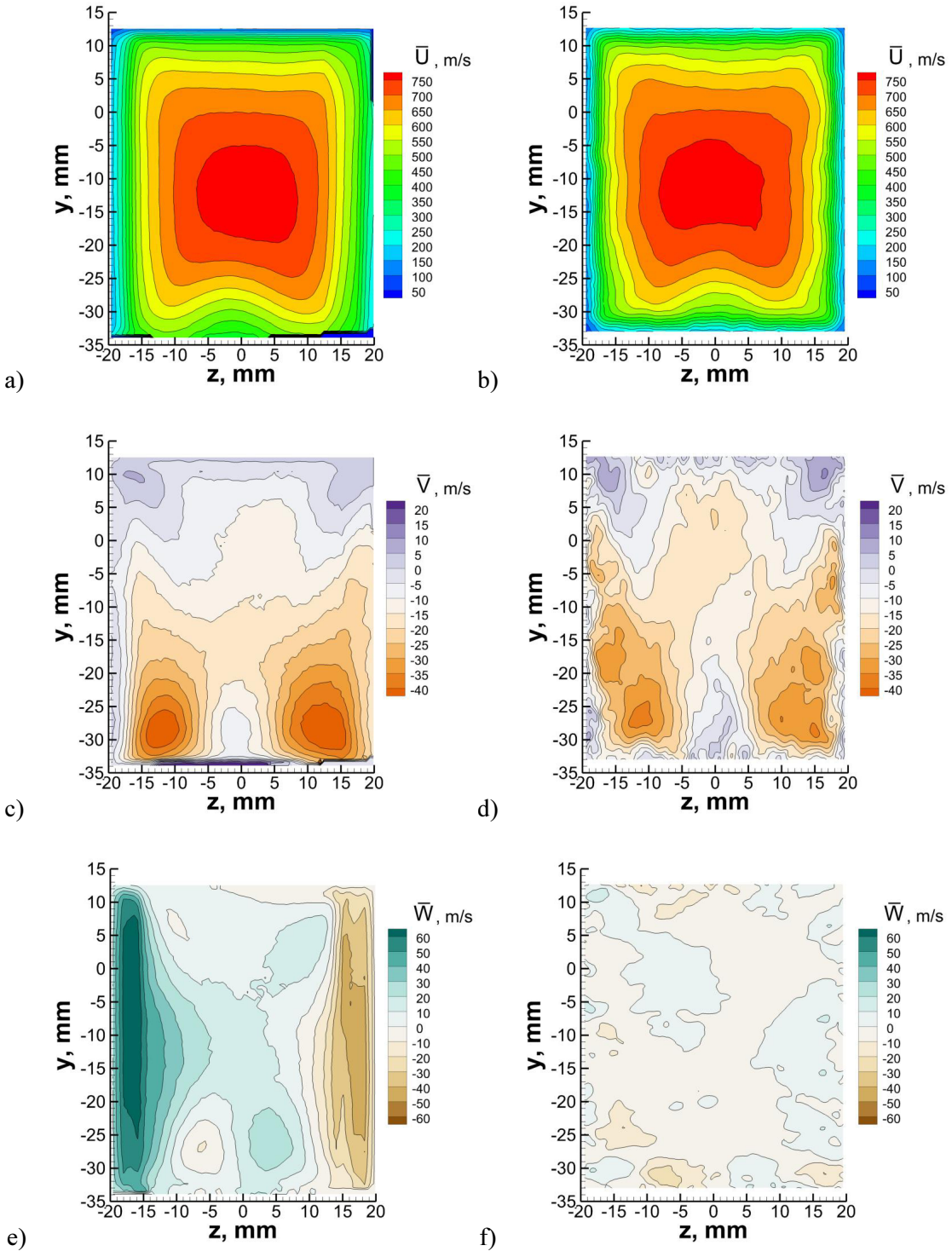

Figure C.6: x/H=82, φ=0.49: a) SPIV, $\bar{U}$, b) CFD, $\bar{U}$, d) SPIV, $\bar{V}$, d) CFD, $\bar{V}$, e) SPIV, $\bar{W}$, f) CFD, $\bar{W}$.

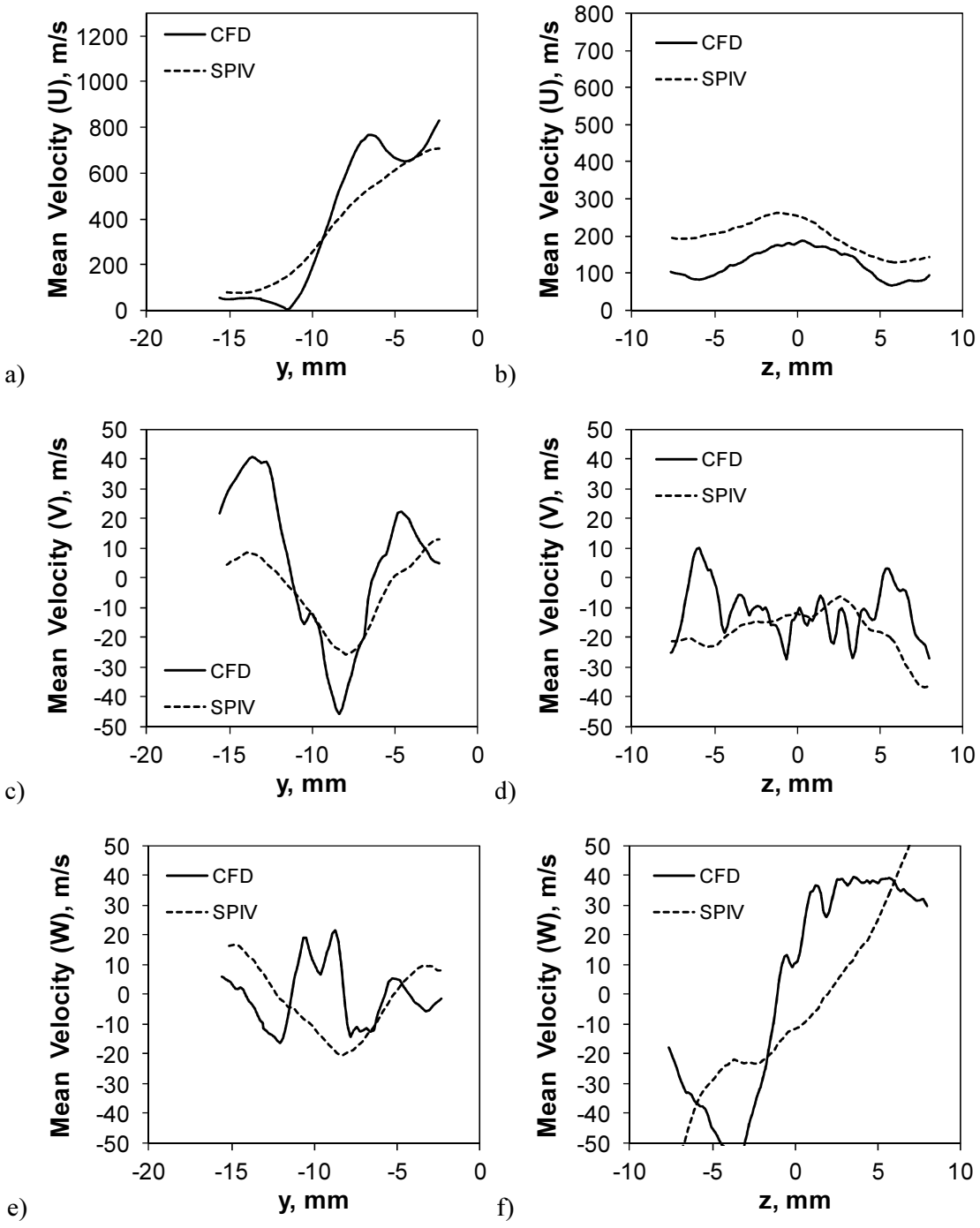

Figure C.7: x/H=6, φ=0.18: a) vertical line, $\overline{U}$, b) horizontal line, $\overline{U}$, d) vertical line, $\overline{V}$, d) horizontal line, $\overline{V}$, e) vertical line, $\overline{W}$, f) horizontal line, $\overline{W}$.

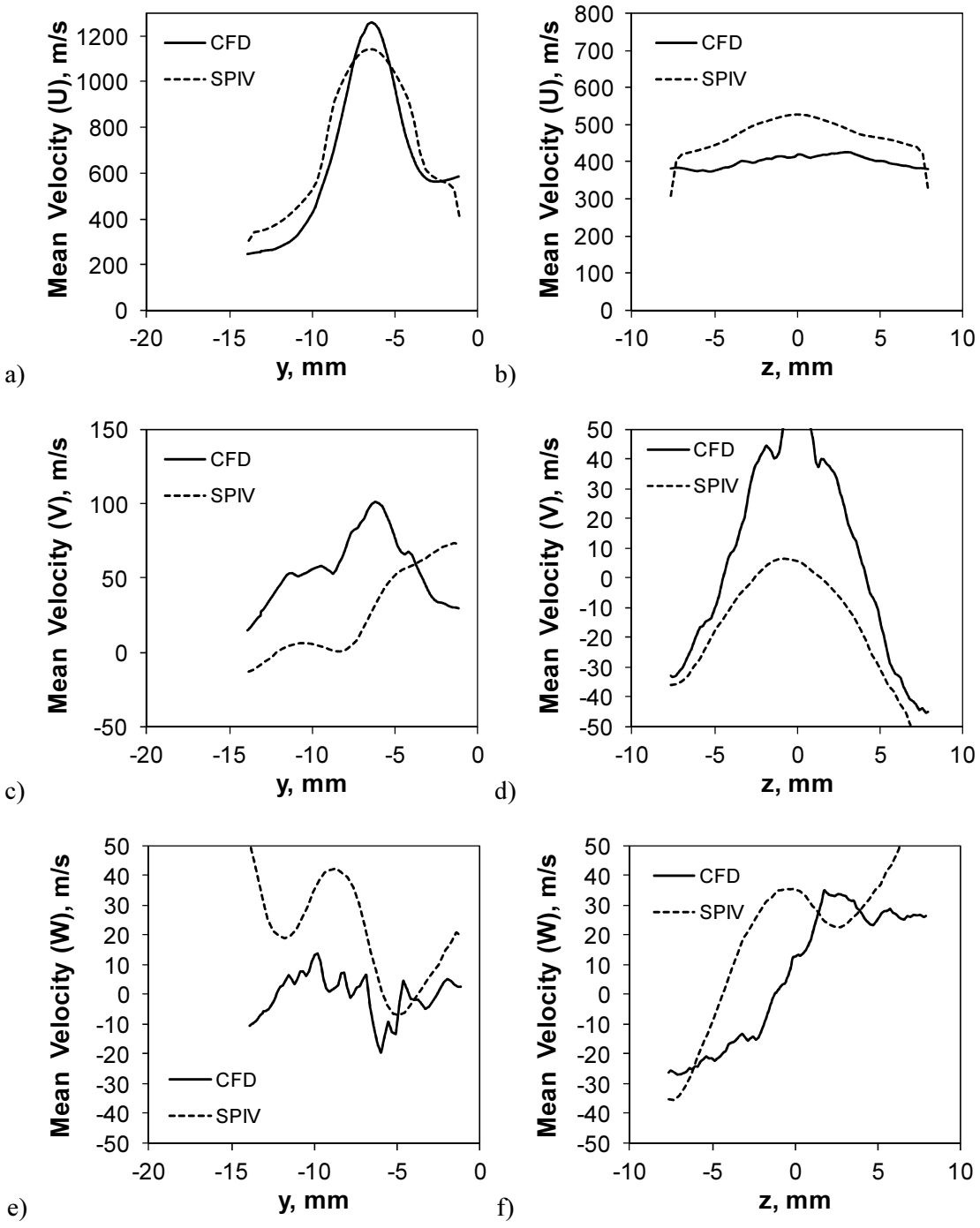

Figure C.8: x/H=6, φ=0.49: a) vertical line, $\bar{U}$, b) horizontal line, $\bar{U}$, d) vertical line, $\bar{V}$, d) horizontal line, $\bar{V}$, e) vertical line, $\bar{W}$, f) horizontal line, $\bar{W}$.

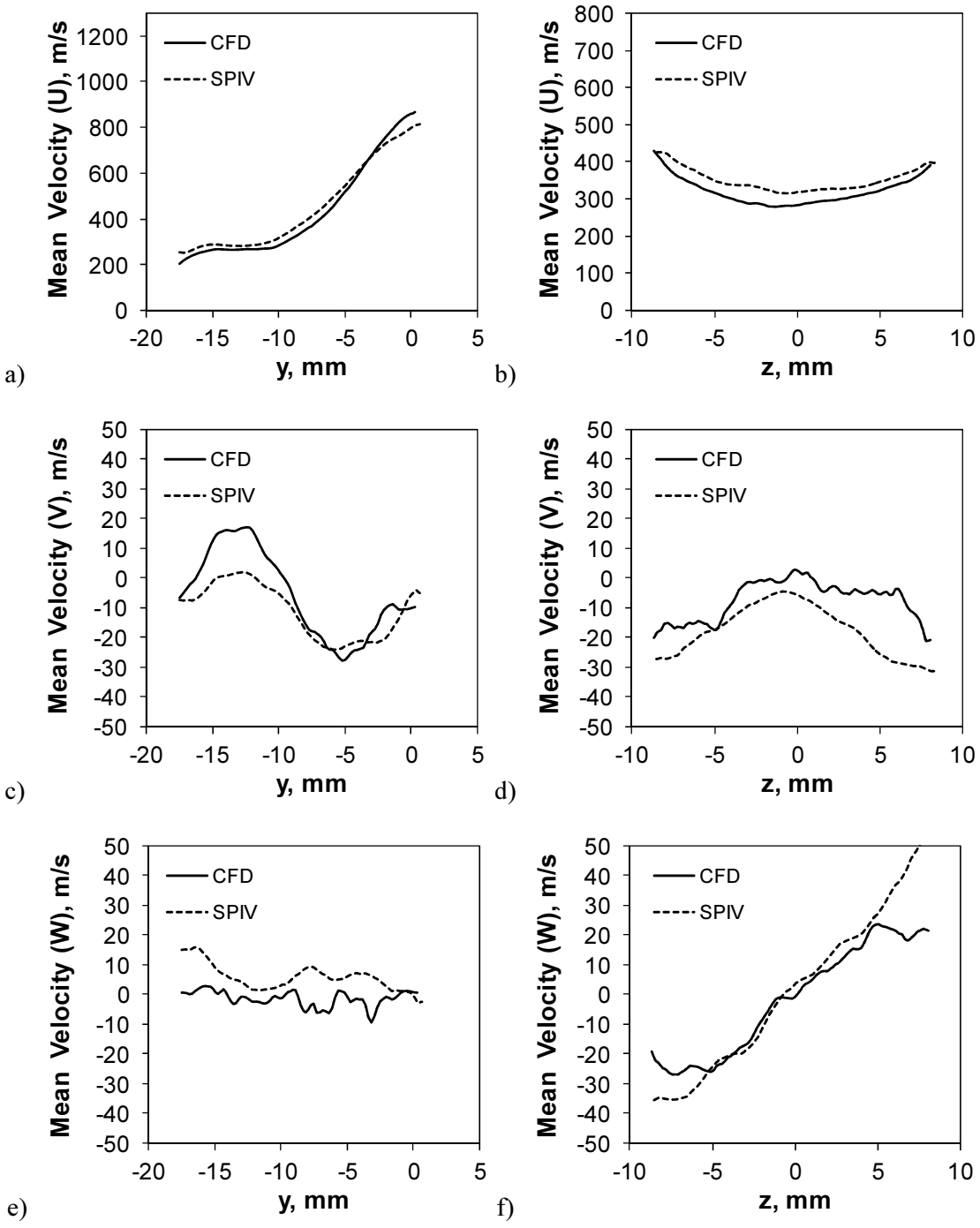

Figure C.9: x/H=12, φ=0.18: a) vertical line, $\overline{U}$, b) horizontal line, $\overline{U}$, d) vertical line, $\overline{V}$, d) horizontal line, $\overline{V}$, e) vertical line, $\overline{W}$, f) horizontal line, $\overline{W}$.

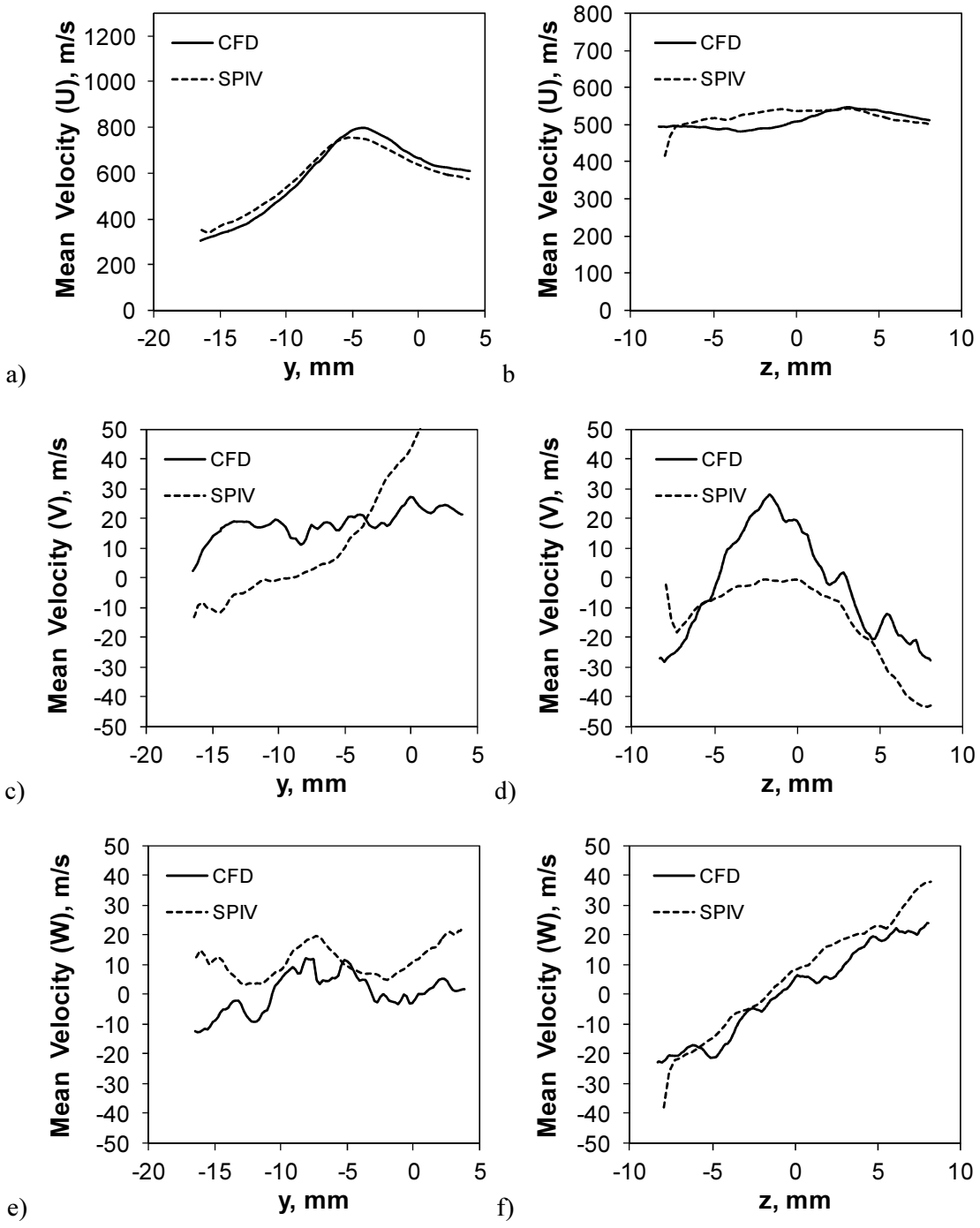

Figure C.10: x/H=12, φ=0.49: a) vertical line, $\overline{U}$, b) horizontal line, $\overline{U}$, d) vertical line, $\overline{V}$, d) horizontal line, $\overline{V}$, e) vertical line, $\overline{W}$, f) horizontal line, $\overline{W}$.

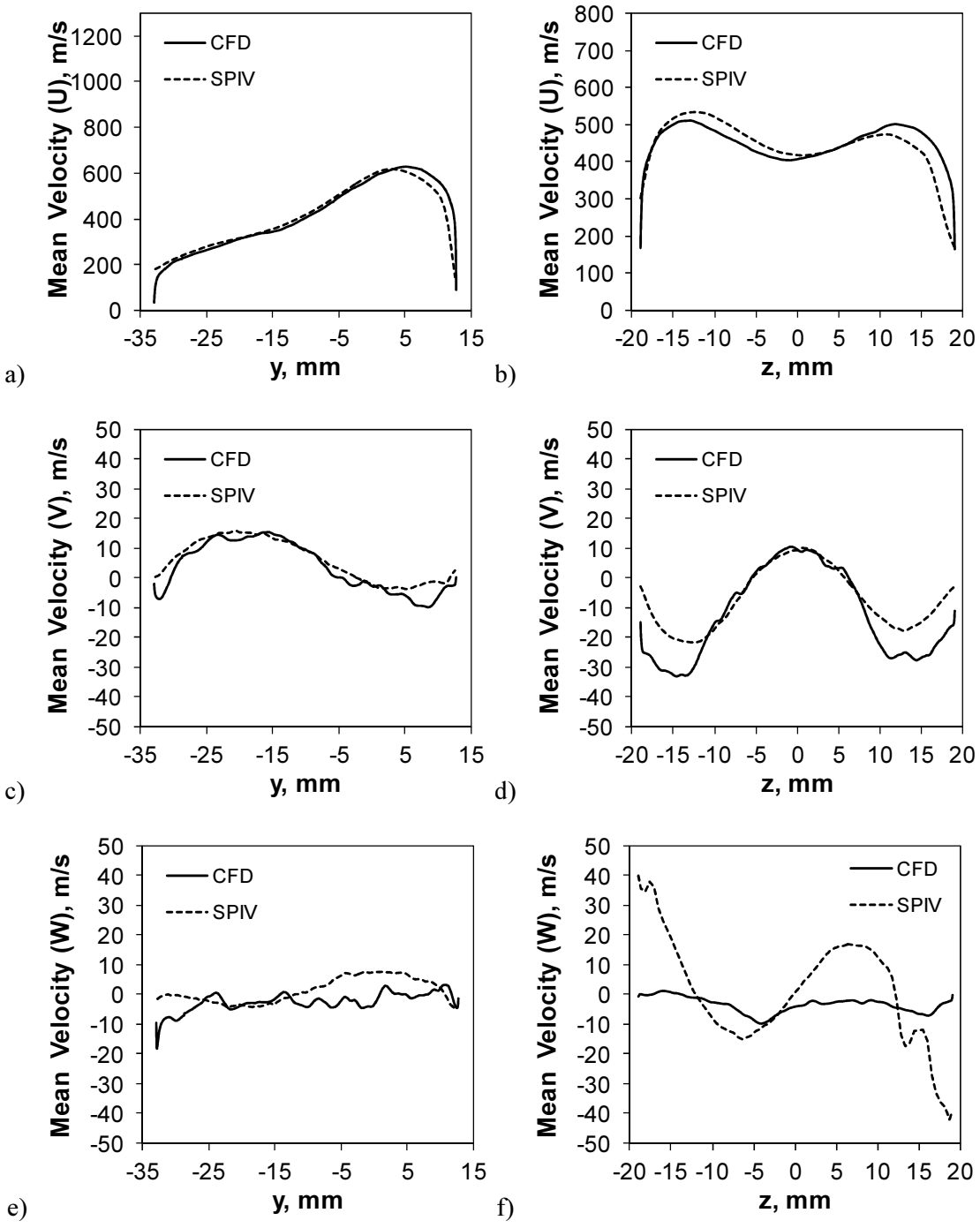

Figure C.11: x/H=82, φ=0.18: a) vertical line, $\overline{U}$, b) horizontal line, $\overline{U}$, d) vertical line, $\overline{V}$, d) horizontal line, $\overline{V}$, e) vertical line, $\overline{W}$, f) horizontal line, $\overline{W}$.

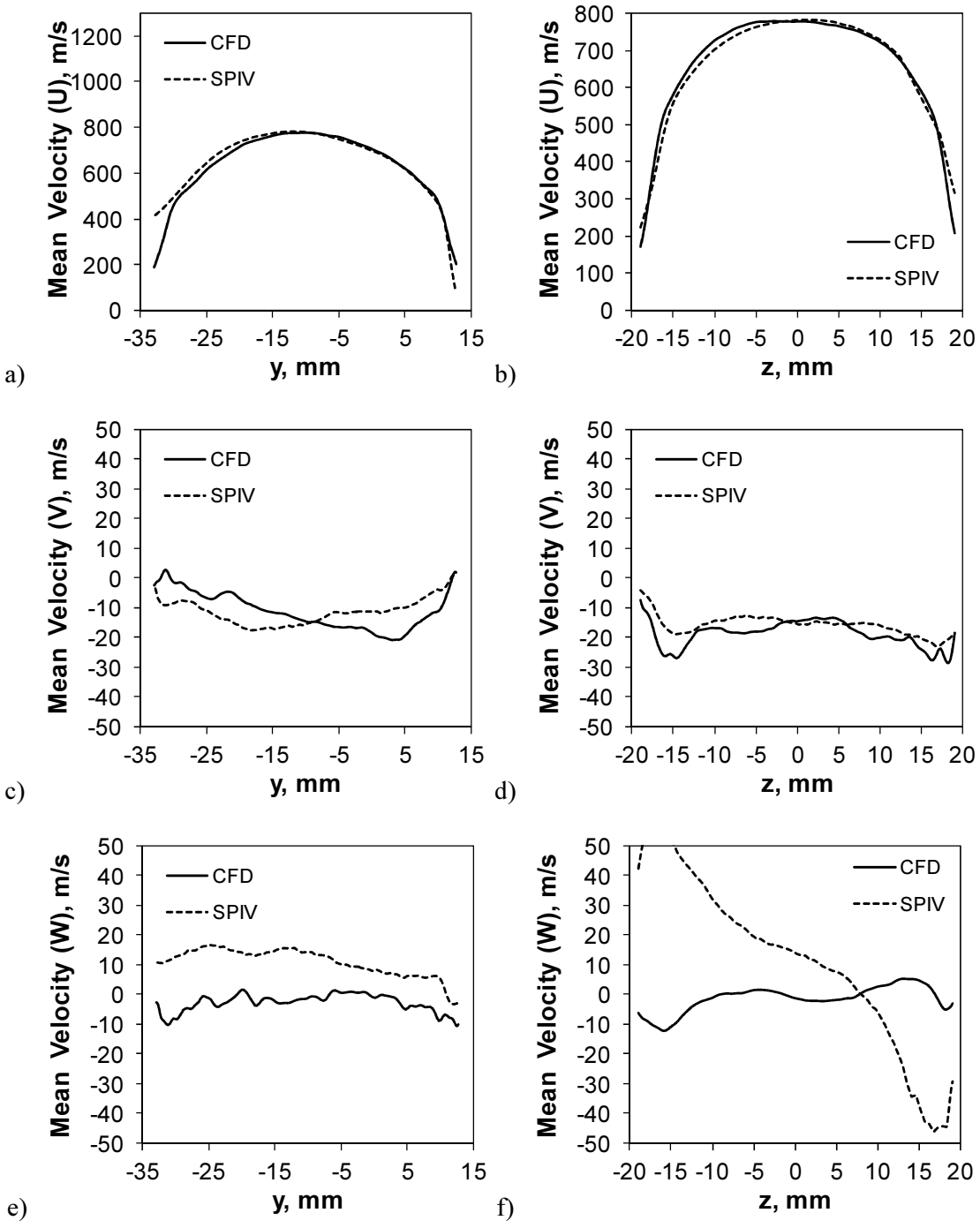

Figure C.12: x/H=82, φ=0.49: a) vertical line, $\overline{U}$, b) horizontal line, $\overline{U}$, d) vertical line, $\overline{V}$, d) horizontal line, $\overline{V}$, e) vertical line, $\overline{W}$, f) horizontal line, $\overline{W}$.